The Dissertation Committee for Seok koo Kim certifies that this is the approved version of the following dissertation:

Platinum catalysts degradation by oxide-mediated platinum dissolution in PEMFCs (Proton Exchange Membrane Fuel Cells)

Committee:

_____
Jeremy P. Meyers, Supervisor

_____
John B. Goodenough

_____
Allen J. Bard

_____
Arumugam Manthiram

_____
Charles B. Mullins

Platinum catalysts degradation by oxide-mediated platinum dissolution in PEMFCs (Proton Exchange Membrane Fuel Cells)

by

Seok koo Kim, B.S.; M.S.

Dissertation

Presented to the Faculty of the Graduate School of

the University of Texas at Austin

in Partial Fulfillment

of the Requirements

for the Degree of

Doctor of Philosophy

The University of Texas at Austin

December, 2011

Dedicated

To my wife, Youngsin Kim

To my son, Byoungwook Kim

Acknowledgements

I would like to give my sincere gratitude to my dissertation advisor Dr. Jeremy P. Meyers, for providing me with the opportunity of being his first student and for enabling me to expand the understanding of the combination of kinetics, thermodynamics and electrochemistry. I also wish to express my thanks to my academic committee members, Dr. John B. Goodenough, Dr. Allen J. Bard, Dr. Arumugam Manthiram, Dr. Charles B. Mullins for their guidance and suggestion.

I am grateful to my colleagues and friends who helped me during the course of this dissertation work: Preethi Mathew for lots of discussion about Pt oxide properties and Pt dissolution, Dr. Babar M. Koraishy for sharing research idea, Isaac Arnquist of Dr. Holcombe group for ICP-MS analysis, Netzahualcoyotl Arroyo Curras of Dr. Bard group for training and discussion of SECM experiment, Jinho Chang of Dr. Bard group for giving me a lot of advice on COMSOL simulation.

Finally, I thank my parents and parents-in-law in South Korea for their precious love all of the years. I thank my wife and son for raising me up with endless love. This dissertation would not have been possible without all of them.

Platinum catalysts degradation by oxide-mediated platinum dissolution in PEMFCs (Proton Exchange Membrane Fuel Cells)

Publication No. _____

Seok koo Kim, Ph.D.
The University of Texas at Austin, 2011

Supervisor: Jeremy P. Meyers

Proton exchange membrane fuel cells (PEMFCs) have attracted great attention due to their high power density, low-temperature operation and high energy conversion efficiency. However, the high cost of Pt catalysts and durability problems hinder their commercialization. So their cost must be lowered drastically and their durability must be extended. In an effort to overcome these problems, there have been intensive efforts to enhance the activity, durability and to lower the price of catalysts by alloying with other less expensive metals. In particular, the sluggish kinetics of ORR caused by Pt oxide at cathode and Pt catalyst degradation by electrochemical surface area (ECSA) loss have been a huge research area where a lot of researchers have paid lots of attention to solve.

In this regard, the objective of this dissertation is to evaluate a series of Pt catalyst electrode surface electrochemical reactions on PEMFC electrode in order to

help searching new catalysts and enhancing system design, assist in the search for new catalysts and improved system design by suggesting the developed mechanism of electrocatalyst activity and stability (durability). We have been focused on understanding the oxide-mediated dissolution of Pt by using electrochemical experiment methods such as RRDE, EQCN, SECM with a combination of ICP-MS and computational simulation with COMSOL Multiphysics.

Firstly, in chapter 3, we showed the oxide-mediated Pt dissolution rate and the influence of hydrogen and cation underpotential deposition on Pt dissolution.

In chapter 4, we revealed oxygen reduction reaction (ORR) plays a significant role in Pt oxide formation and reduction that influences the Pt catalyst dissolution, resulting in accelerated Pt dissolution rate at specific potential range.

Finally, we found out the nature of mobile species generated during PtO_2 reduction process which have been disputed as Pt ion or other mobile species and fulfilled computational simulation for evaluation of SECM experiment in chapter 5.

Based on these experiments and simulation, we were able to explain some mechanism of literature results that already were reported but have not been clearly explained so far. In terms of the purpose of this dissertation, the mechanism of oxide-mediated Pt dissolution, influence of ORR to Pt oxide formation/reduction and Pt dissolution, the nature of mobile species generated during PtO_2 reduction process, are sure to be very helpful in developing new catalysts and enhancing system design and suggested operating conditions.

TABLE OF CONTENTS

LIST OF TABLES

LIST OF FIGURES

CHAPTER 1

Introduction

1.1 Fuel cells

Fuel cells are attractive devices that offer more efficient energy conversion with less pollution in comparison to other conventional power sources during a time in which society faces rapid depletion of fossil fuels and rising environmental concerns (1). A fuel cell can be defined as an electrochemical device that converts chemical energy such as hydrogen or methanol into electric energy (including heat energy, pure water as by product). Comparing to the Carnot cycle devices such as the combustion engine that has efficiency less than 30%, the overall efficiency of the fuel cell system improves significantly up to 90 % when the fuel cell is combined with other system that use waste heat that comes out of fuel cell (2). We realize that the environmental considerations and high efficiency bring about the significant advantage of fuel cells over the traditional power suppliers. Before reviewing the proton exchange membrane fuel cell (PEMFC), a general introduction of fuel cells will be given in the follow section.

Table 1.1 Classification of different types of fuel cells (2).

	AFC	***PEMFC***	***DMFC***	***PAFC***	***MCFC***	***SOFC***
Electrolyte	Liquid solution (KOH)	Polymer membrane (Nafion)		Phosphoric acid (H_3PO_4)	Molten carbonate	Ceramic oxide
Charge Carrier	OH^-	H^+		H^+	CO_3^{2-}	O^{2-}
Operating temperature	50 ~200 °C	50 ~ 100 °C		~ 200 °C	600 ~ 700 °C	600 ~ 1000 °C
Anode reaction	$H_2+2OH^- \rightarrow 2H_2O+2e^-$	$H_2 \rightarrow 2H^++2e^-$	$CH_3OH+H_2O \rightarrow CO_2+6H^++6e^-$	$H_2 \rightarrow 2H^++2e^-$	$H_2+CO_3^{2-} \rightarrow H_2O+CO_2+2e^-$	$H_2+2OH^- \rightarrow 2H_2O+2e^-$
Cathode reaction	$1/2O_2+H_2O+2e^- \rightarrow 2OH^-$	$1/2O_2+2H^++2e^- \rightarrow 2H_2O$	$3/2O_2+6H^++6e^- \rightarrow 6H_2O$	$1/2O_2+2H^++2e^- \rightarrow 2H_2O$	$1/2O_2+CO_2+2e^- \rightarrow CO_3^{2-}$	$1/2O_2+2e^- \rightarrow O^{2-}$
Efficiency	50%	40~50%	40%	40%	>50%	40%
Power Range	5 ~ 150KW	5 ~ 250KW	<1~100KW	50KW~11MW	100KW~2MW	100~250KW
Combined heat and power efficiency	>80%	70~90%		>85%	>80%	<90%
Major Application	Space, Military Portable, Transportation, Stationary power			Combined heat and stationary power	Combined heat and stationary power and transportation	

1.1.1 Classification of fuel cells

All fuel cells operate via the same basic principle, namely, that a fuel is oxidized into electrons and protons, oxygen is reduced into oxide species and these proton or oxide ions are transported through the ion conducting electrolytes. Based on

the type of the ion conducting electrolytes, fuel cells can be classified into alkaline fuel cell (AFC), proton exchange membrane fuel cell (PEMFC) or direct methanol fuel cell (DMFC), phosphoric acid fuel cell (PAFC), molten carbonate fuel cell (MCFC) and solid oxide fuel cell (SOFC)(1-2). The first four fuel cell types are for low temperature usage which operate at below 200 ^{o}C and MCFC, SOFC operate at 600 ~ 1000 ^{o}C. These types of fuel cells are classified in Table 1.1 (2).

1.1.2 Proton Exchange Membrane Fuel Cell (PEMFC)

The proton-exchange membrane fuel cell (PEMFC) as discussed above is the candidate power sources for automotive application due to their low operating temperature, high power density, short start-up time (3). Figure 1.1 shows a schematic of the PEMFC stack structure; gas diffusion layer (GDL) and catalyst layer (CL) of anode and cathode, polymer electrolytes membrane (ionomer membrane).

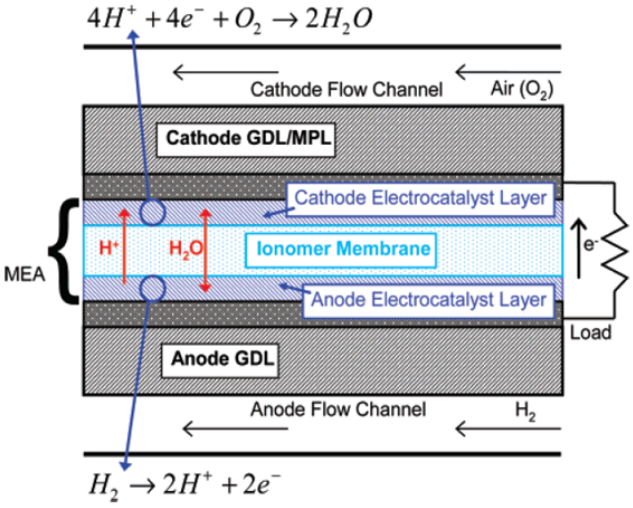

Figure 1.1 Schematic cross section of a typical PEMFC (4).

A membrane-electrode assembly (MEA) or catalyst coated membrane (CCM) consists of a thin film (25 ~ 175 μm) of ion conductive electrolytes covered with a catalyst layer (5~50 μm) on each side. One of the outstanding technology in PEMFC is the development of perfluorosulfonic acid (PFSA) membrane (Nafion®) that has polytetrafluoroethylene (PTFE) backbone providing the chemical corrosion resistance and sulfonated functional branch groups giving high proton ion conductivity(5). And the MEA preparation technique was developed by Los Alamos National Laboratory by casting the mixture of carbon supported platinum catalyst and ionomer and pressing to make so called thin film decal (6-7). This ionomer and catalyst composite networking made platinum loadings reduced from 5 mg/cm^2 to below 0.5 mg/cm^2. Both sides of MEA was covered by 200 ~ 300 μm porous gas diffusion layers (GDL) that works for collecting current, providing uniform gas feeding to both catalyst layers. Hydrogen gas or oxygen (or air) gas flow through the channels of the bipolar plates to the anode or cathode and oxidize or reduce on the each catalyst surface, generating or accepting protons or electrons. This electrochemical reaction is exothermic and the generated heat can be dissipated as waste heat or used outside of the fuel cell. All the electrochemical half-cell reactions at the anode and cathode occur very slowly at the low operating temperature of the PEMFC. Therefore, efficient catalysts, well organized stack cell design and operational technique are required to increase the rate of the reactions at both electrodes (8).

1.1.3 PEMFC thermodynamics and electrochemistry

Since the PEMFC is energy conversion device from chemical energy to electrical energy via heterogeneous electrochemical reaction on the surface of platinum catalysts, a study of thermodynamics is necessary to understand the conversion of energy. Thermodynamics is the theoretical boundary of what is possible with a fuel cell; i.e. any real fuel cell performs at or below its thermodynamic limit. The reversible (Nernst) potential, E_{rev}, is defined as the cell potential at the equilibrium or reversible state. In a PEMFC, the electro-oxidation reactions and its reversible potential at the anode and electro-reduction reaction of oxygen at the cathode are as follows:

For anode: $H_2 \rightarrow 2H^+ + 2e\text{-}$ $E^o = 0.000\ V_{RHE}$ (1.1)

For cathode: $O_2 + 4H^+ + 4e^- \rightarrow 2H_2O$ $E^o = 1.229\ V_{RHE}$ (1.2)

Overall: $2H_2 + O_2 \rightarrow 2H_2O$ $E^o = 1.229\ V_{RHE}$ (1.3)

However, even under no current status, the potential that is open circuit potential (E_{ocv}) of PEMFC shows lower than E_{rev} due to a mixed potential formation and other parasitic processes. Moreover, the potential under the external electrical load that is cell potential (E_{cell}) drops proportionally to the external current load.

The performance of PEMFC can be evaluated by polarization curve that is simply given by the combined effect of various losses as shown at Figure 1.2. The last graph at Figure 1.2, called a polarization curve, shows the voltage output of the PEMFC for a given current output. An ideal PEMFC would supply any amount of

current (as long as it is supplied with sufficient fuel) while maintaining a constant voltage determined by thermodynamics. However, in practice, the actual voltage output of real PEMFC is less that the ideal thermodynamically predicted voltage. This potential deviation from the equilibrium value is called the overpotential (η) and also referred to as polarization or voltage loss. There are three major types of fuel cell potential losses which give PEMFC polarization curve its characteristic shape.

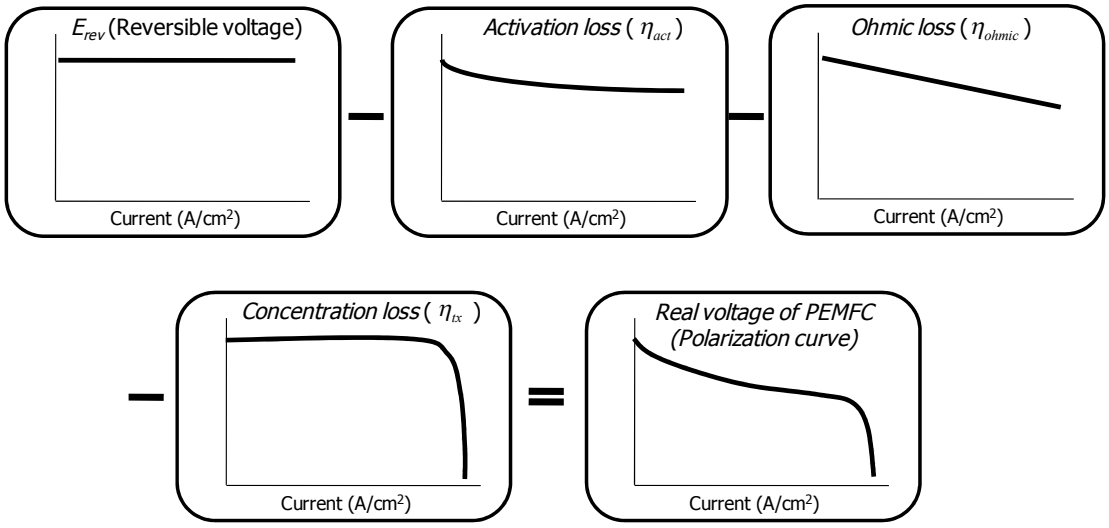

Figure 1.2 Pictorial summary of major factors that contribute to PEMFC performance. The overall PEMFC performance can be determined by starting from the ideal thermodynamic voltage (E_{rev}) and subtracting out the losses due to activation (η_{act}), ionic conduction (η_{ohmic}), and concentration (η_{tx}) (9).

The first one is activation overpotential (η_{act}) that is activation losses due to electrochemical reaction related to kinetics. For a redox reaction at an electrode, the current density *j* is given by the Butler-Volmer Equation,

$$i = i_0 \left(\exp\left(\frac{\alpha_a nF\eta}{RT} \right) - \exp\left(\frac{-\alpha_c nF\eta}{RT} \right) \right) \tag{1.4}$$

where i_0 is the exchange current density, α_A and α_C are the transfer coefficients, respectively, for the anodic and cathodic reaction, and η is the overpotential to drive the reaction. As seen in this Equation, some overpotential is required to drive the electrochemical reaction. This is called activation overpotential and is associated with the sluggish electrode kinetics, especially η_{ORR} by sluggish oxygen reduction reaction (ORR) at the cathode in PEMFC. It is clear from the Equation that the higher the exchange current density, the lower must be the activation overpotential losses for the same current density.

The second term is ohmic overpotential (η_{ohmic}) due to ionic and electronic conduction. Ohmic losses are related to the resistance to the flow of ions in the electrolyte and resistance to the flow of electrons through the electrically conductive components such as porous carbon layer and bipolar plate current collector. These losses are expressed by Ohm's law.

The final expression is concentration overpotential (η_{tx}) due to mass transport. This loss occurs when a reactant is rapidly consumed at the electrode by the electrochemical reaction so that concentration gradients are established.

So, the real voltage output for a PEMFC can thus be written by starting with thermodynamically predicted voltage output of the PEMFC and then subtracting the voltage drops due to the various losses explained above.

$$V = E_{rev} - \eta_{act} - \eta_{ohmic} - \eta_{tx} \tag{1.5}$$

Where V is real output voltage of PEMFC and E_{rev} is thermodynamically predicted PEFMC voltage output.

1.1.4 Challenges of PEMFC technology to automobile application

One of the challenges to commercialization of PEMFC is the cost of the cell stack. A significant contribution to the ultimate cost of PEMFC systems, even after high-volume manufacturing techniques are perfected, is the use of platinum nanoparticle as the catalysts of the hydrogen oxidation (HOR) and oxygen reduction reaction (ORR). In order to decrease the catalyst loading, much research has been performed to improve the specific performance of catalysts by developing platinum alloy catalysts (10), synthesizing none platinum types of catalysts (11) and searching new supporting materials such as graphene (12), metal oxides (13), etc.

The second major technical challenge is durability or long-term performance stability of PEMFC. For example, for commercial usage of PEMFC in automotive

applications, DOE estimates that at least 5,000 hours operation time and 30,000 times start/stop cycles (causing voltages >1.5 V_{RHE}) are required (14). In particular, Reiser *et al*. (15) explained how start/stop cycles influence platinum catalysts by incorporating the reverse current mechanism. They showed huge catalyst and carbon support loss when the anode was partially filled with fuel (hydrogen) especially when a PEMFC was started/stopped. And they also describe a mechanism in which the interfacial potential at the cathode goes up 1.5 V_{RHE}, which results in carbon and platinum oxidation, oxygen evolution on the cathode adjacent to the hydrogen poor portion or stack cell. This potential increase threatens to severely reduce the PEMFC lifetime in automobile application where about 30,000 times start/stop cycles are required (14). Figure 1.3 and 1.4 shows the schematic of the reverse current mechanism within MEA and along two stack cells. Actually the presence of the reverse current decay mechanism is not readily apparent in the current potential behavior monitored by the observer.

The Cell 1 in Figure 1.4 is normal one; the cell 2 is referred to as abnormal one because air (O_2) is present on both electrodes. The overall PEMFC potential is determined by measuring the difference between the current collector potential of the cathode and anode electrodes. The current collector potential of the cathode electrodes is determined by the mixed potential of oxygen reduction reaction (ORR), oxygen evolution reaction (OER), carbon corrosion reaction (CCR). And the current collector potential of the anode electrodes is determined by the oxygen reduction reaction (ORR) and hydrogen oxidation reaction (HOR) that is mixed potential. The

potential difference between anode and cathode defines the drop in solution potential in the hydrogen starved portion of the cell (abnormal cell in Figure 1.4). Because there exists only one potential (i.e. mixed potential) at PEMFC, it results in local anode and cathode currents being equal and opposite. So, at the abnormal cell, the carbon corrosion reaction (CCR) and oxygen evolution reaction (OER) occur on what is normally the cathode while the oxygen reduction reaction (ORR) occurs on the anode. Hence, the current is flowing in reverse of normal operation. Operational condition including abnormal conditions of PEMFC for automobile application are shown at Table 1.2

Table 1.2 Operational condition of PEMFC for automobile application.

Condition	*Anode (Fuel)*		*Cathode (O_2/Air)*		*Cell potential (E_{cell})*	*Accelerated degradation test mode (ADT)*
	Fuel	Potential (V_{RHE})	Gas type	Potential (V_{RHE})		
Normal	H_2	0.01	O_2/Air mixture	0.85	0.8	CV
Idling	H_2	0.0	O_2/Air mixture	0.9	0.9	.
OCV	H_2	0.0	O_2/Air mixture	1.0	1.0	.
Shut down	Air	1.1	O_2/Air mixture	1.1	0	.
Start	H_2/Air mixture	0.0/1.1	O_2/Air mixture	1.0/ **>1.5**	1.0	Potential step, CV
Stop	Air/H_2 mixture	1.1/0/0	O_2/Air mixture	**>1.5**/1.0	1.0	Potential step, CV
Partial H_2 coverage	H_2/inert	0.05/1.1	O_2/Air mixture	0.85/ **>1.5**	0.8	Potential step, CV
H_2 starvation	H_2/inert	**> 1.5**	O_2/Air mixture	0.85	< -0.65	Potential step, CV
O_2/Air starvation	H_2	0.05	(O_2/Air)/H_2 mixture	0.85/ -0.05	-0.1	.

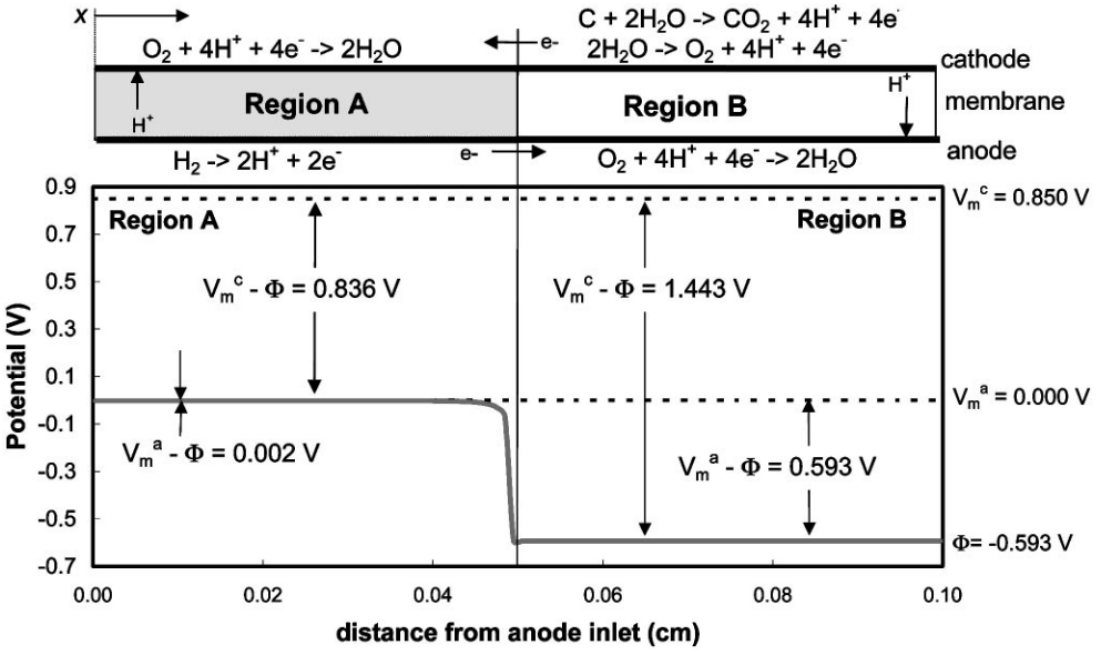

Figure 1.3 Potential distributions along anode flow path during reverse current conditions.

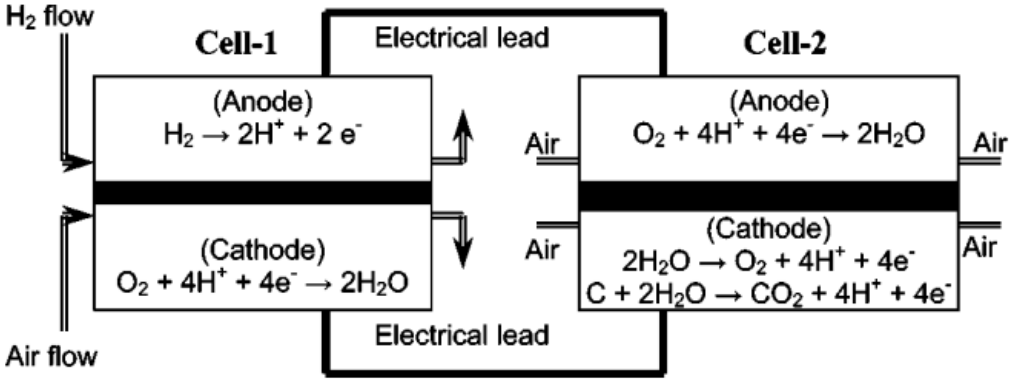

Figure 1.4 Schematic of a dual cell to show the reverse current condition(15).

1.2. PEMFC durability and degradation

Typically, a PEMFC exhibits a gradual power decline with operating time. This gradual performance decline comes from various degradation mechanisms that occur in the fuel cell's different components and the relative contribution of each component's degradation to the degradation of the entire fuel cell. A lot of degradation mechanisms of PEMFC degradation have been proposed. These include polymer electrolyte degradation (16), catalyst layer degradation (17-18), carbon support corrosion (19-20), and gas diffusion layer (GDL) degradation (21).

Especially, catalyst layer degradation is among the most critical issues and enhancing durability and stability is also a major challenge in PEMFC recent research studies (22).

1.2.1 Degradation by electrochemical surface (ECSA) area loss

One of the significant causes of PEMFC degradation is the platinum deterioration on the cathode side. This degradation generally is explained by three mechanisms that are relevant to the ECSA loss (23). The first one is the electrochemical platinum dissolution which results in particle size increase via so called Ostwald ripening and platinum nucleation at electrolytes phase. The second one is platinum detachment by carbon corrosion and the last one is platinum particle's migration and coalescence on carbon surface.

1.2.1.1 Electrochemical platinum dissolution

The first cause of ECSA loss in PEMFC is the electrochemical dissolution of platinum. Pourbaix introduced the method of plotting the thermodynamic equilibrium conditions of all the reactions that occur for a metal in contact with a aqueous solution on a potential vs pH diagram which is known as Pourbaix diagram shown at Figure 1.5 (24). This Pourbaix diagram shows the possibility of platinum oxidation and reduction under various electrochemical potential and pH condition as determined by the Nernst equation, $E = E^O - (RT/nF)\ln[H^+] - (RT/nF)\ln[Pt^{z+}]$, where E^O is the cell potential under standard conditions . Especially around the condition < pH 1 which is similar with the typical pH range of PEMFC electrolyte, is the concern in terms of platinum dissolution. Several studies in the literature (25-27) on the dissolution of Pt under equilibrium conditions in acid solution showed that the solubility of Pt increase with temperature, pH and the upper potential limit (E_H) in potential cycling. We can derive some Equations regarding to platinum oxidation by Pourbaix diagram.

$$Pt \leftrightarrow Pt^{2+} + 2e^- \qquad E^o = 1.188 - 0.0295\log[Pt^{2+}] \qquad (1.6)$$

$$Pt^{2+} + 2H_2O \leftrightarrow PtO_2 + 4H^+ + 2e^- \qquad E^o = 0.837 - 0.1182pH - 0.0295\log[Pt^{2+}] \qquad (1.7)$$

$$Pt + H_2O \leftrightarrow PtO + 2H^+ + 2e^- \qquad E^o = 0.980 - 0.0591pH \qquad (1.8)$$

$$PtO + H_2O \leftrightarrow PtO_2 + 2H^+ + 2e^- \qquad E^o = 1.045 - 0.0591pH \qquad (1.9)$$

$$PtO_2 + H_2O \leftrightarrow PtO_3 + 2H^+ + 2e^- \qquad E^o = 2.000 - 0.0591pH \qquad (1.10)$$

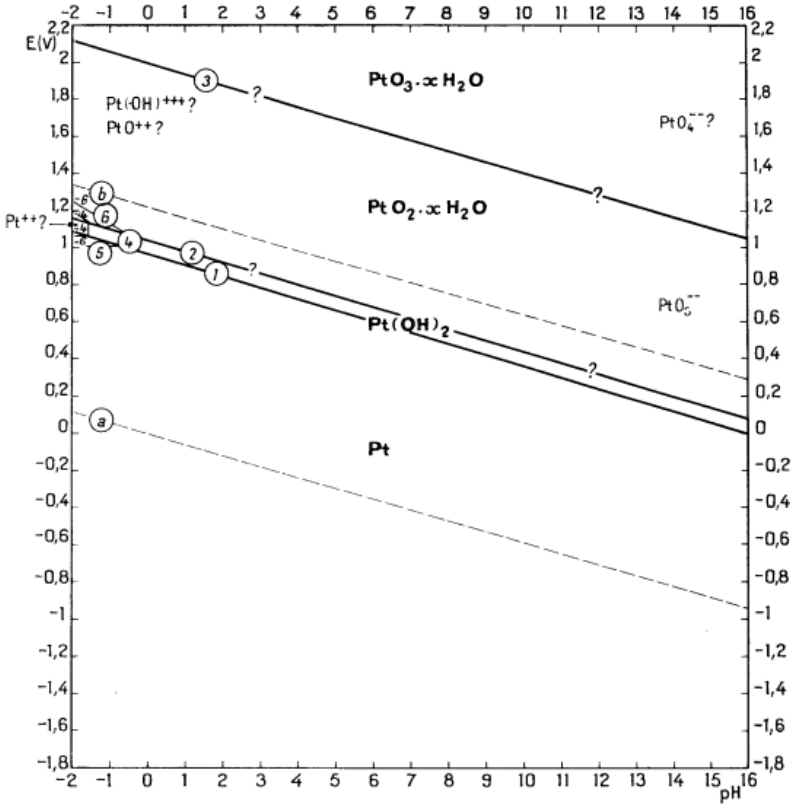

Figure 1.5 Potential-pH equilibrium Pourbaix diagram for platinum-water (24).

While there will be some form of platinum in solution at very low concentrations at low potentials, raising the electrode potential suggests a drastic increase in the mean concentration of platinum ions in solution. The presence of oxide on the surface can, passivate the platinum surface and prevent the higher rates of dissolution that would be expected if bare platinum were exposed to cathode operating potentials.

The evidence for platinum dissolution due to the electrochemical driving force are strong potential dependence of surface loss, potential dependent increase in dissolved platinum, dissolution rates with Nernstian predictions, reduced dissolution

of platinum oxides and Ostwald ripening. Bindra *et al*. (28) quantified dissolution of platinum in phosphoric acid at various potential region by weighing mass change of platinum wire. Wang *et al*. (29) also demonstrated an increase in dissolved platinum from 0.65 V_{RHE} to 1.1 V_{RHE} and decrease for potentials above 1.1 V_{RHE} by employing inductively coupled plasma mass spectrometer (ICP/MS) with carbon supported nanoparticle platinum (Figure 1.6). The decrease of platinum dissolution above 1.1 V_{RHE} is attributed to the formation of protective platinum oxide layer (PtO or PtO_2) formed above 1.1 V_{RHE} by the study of Jerkiwsicz *et al*. (30) by using electrochemical quartz crystal nanobalance (EQCN) and *ex-situ* Auger electro spectroscopy (AES).

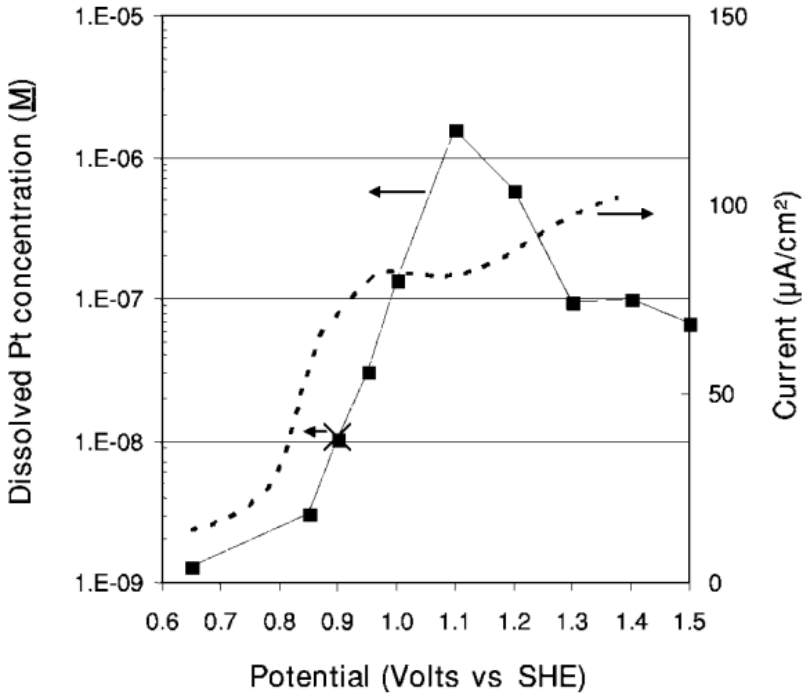

Figure 1.6 Platinum dissolution dependence on potential (29).

However, as shown as at Figure 1.7, a lot of studies showed many deviations of Nernstian dissolution dependency on nanoparticle sized platinum catalyst used in PEMFC. This discrepancy can be attributed in part to the particle size effect. An electrochemical equivalent of the Gibbs-Thomson Equation can provide the effect of interfacial energy on the solubility in terms of particle size.

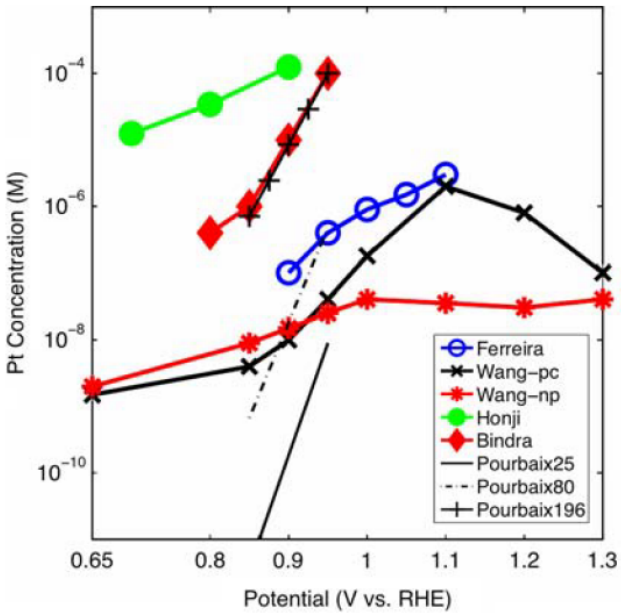

Figure 1.7 Comparison of dissolved Pt concentrations of previous studies (23).

The modified concentration of platinum dissolution can be calculated by plugging the Gibbs-Thomson Equation into the Nernst Equation.

$$C_{pt^{2+}} = \exp\left(\frac{2F(E - E^{o}(T)) + (2\gamma\Omega / d)}{RT}\right) \tag{1.11}$$

Where Ω is the volume per atom, γ is the surface energy and d is the platinum nanoparticle diameter. This thermodynamic analysis indicates that the platinum dissolution ought to increase with decreasing particle size (23).

1.2.1.2 Oxide-mediated platinum dissolution

Platinum is generally considered to be an 'inert' material, a noble metal, in the area of electrochemistry, thus used as a catalyst for hydrogen oxidation, oxygen reduction in the PEMFC. However, it was found that platinum is passivated (31) at PEMFC cathodic operating potentials of about 0.8 V_{RHE} and the oxygen reduction reaction activity (ORR) is significantly lower on the passive oxide film covered platinum surface than on an oxide-free surface. Moreover, continuous platinum oxide formation and reduction by potential cycling was reported to enhance platinum catalyst degradation and dissolution due to the place exchange between platinum atom and oxygen atom (32) and various potential waveforms, scan rates and potential limits have been used to evaluate the relationship between platinum oxide and platinum dissolution (17, 33). Understanding of the nature of oxide formation on both platinum and carbon will enhance an understanding of the electrode-electrolyte interface and further focus the search for new catalysts.

1.2.1.3 Carbon corrosion

Irrespective of the metal catalyst itself undergoing dissolution, the high surface area carbon support is also known to undergo significant degradation. The oxidation of carbon proceeds according to the reaction

$$C+2H_2O \leftrightarrow CO_2+4H^+ +4e^- \qquad E^o = 0.207\ V_{RHE} \qquad (1.12)$$

While the oxidation potential is enough low to be in the operating cell potential window of PEMFC, it is kinetically not favored in terms of isolating the platinum islands electronically from the electrode. This leads to ECSA loss through loss of contact with the surface, or via agglomeration as particles become less highly dispersed.

1.2.1.4 Migration and coalescence (sintering)

Crystallite migration and coalescence in the absence of electrolytes were observed at Pt/C catalyst (34). However this will be insignificant at low temperature such as PEMFC operation condition. Although solid experimental evidence of migration and coalescence of platinum nanoparticles in PEMFC has not been reported, this process is responsible for asymptotic platinum particle size distributions with a tail toward large particle size found in PEMFC cathode after long time operation (35).

1.2.2 Polymer electrolyte degradation by hydrogen peroxide

It is commonly believed that perfluorosulfonic acid (PFSA) based membrane such as Nafion is attacked by highly reactive oxygen radicals (•OH, •OOH) generated by an electrochemical or chemical reaction of hydrogen and oxygen at a platinum catalyst (36). Their unpaired electrons react with weak polymer end-group in the membrane. Pozio *et al*. (37) showed that the free radical attack of the perfluorinated molecular chains from weak bonds is a degradation mechanism and the radicals are derived from H_2O_2 which can form from a two-electron oxygen reduction and from oxygen molecules permeated through the membrane from the cathode to anode. The hydrogen peroxide was observed within a PEM fuel cell membrane when H_2 and air are present as gas inputs by an in situ experimental technique (38).

$$O_2+2H^++2e^- \leftrightarrow H_2O_2 \qquad E^o = 0.695\ V_{RHE} \qquad (1.13)$$

This H_2O_2 can diffuse into the membrane, and chemically breaks down into hydroxyl radicals assisted by metal ions present in the membrane(37). The decomposition mechanism of the membrane by radical attacks to the polymer weak end-group such as $–CF_2COOH$ is introduced by Curtin *et al*. (39). The reaction mechanism is shown below.

$$Rf\text{-}CF_2COOH+\bullet OH \rightarrow Rf\text{-}CF_2\bullet+CO_2+H_2O \qquad (1.14)$$

$$Rf\text{-}CF_2\bullet+\bullet OH \rightarrow Rf\text{-}CF_2OH \rightarrow Rf\text{-}COF+HF \qquad (1.15)$$

$$Rf\text{-}COF+H_2O \rightarrow Rf\text{-}COOH+HF \qquad (1.16)$$

The –COOH group is regenerated in last Equation, and these reactions are cycled continuously. Once the decomposition process begins at one end group, a whole chain unit can be decomposed to HF, CO_2 and low-molecular weight species by the radical depolymerization reactions (so called “unzipping mechanism”) (4). Mittal *et al*. (40) also suggested that sulfonic acid groups could be the key to the radical attack mechanism and membrane degrading species can be directly formed by molecular H_2 and O_2 on the surface of Pt catalyst subject to the surface properties of Pt catalyst.

CHAPTER 2

Experimental methodology

2.1 Electrochemical quartz crystal nanobalance (EQCN)

An electrochemical quartz crystal nanobalance (EQCN) is a variant of acoustic wave nanosensors that are capable of ultrasensitive mass measurements. This method has been used to enable simultaneous and in-situ determination of the mass variation in relation to surface charge density associated with an electro-sorption or electro-deposition process. The development of this sensitive technique has played an important role on the electrochemical surface (interfacial) science showing that EQCN is a useful and quantitative tool for in-situ measuring atomic level processes at working electrode surface. For example, under favorable conditions, a typical QCN can measure a mass change of 0.1~1 ng/cm^2.

However, the greater the sensitivity required for the EQCN technique, more reliable and accurate evaluation of the calibration constant (C_f) are also required. The mass sensitivity of the EQCN originates from the relationship between the oscillation frequency (Δf) and total mass change of the crystal & the ad-layer of materials residing at the crystals electrode, given by the Sauerbrey Equation shown below.

$$\Delta m = -(\frac{\sqrt{\rho_q \mu_q}}{2nf_o^2})\Delta f = -(\frac{N\rho_q}{f_o})\Delta f = -C_f \Delta f \qquad (2.1)$$

In equation (2.1), f_o is the resonant frequency of the quartz-crystal resonator (in this study -7.995 MHz in air), ρ_q the density of quartz (2.684 gcm^{-3}) and μ_q the shear modulus of quartz (2.947 X 10^{11} $gcm^{-2}s^{-1}$), N is a frequency parameter (1670 kHz mm) characteristic of the crystal, and C_f is the sensitivity factor ($ngHz^{-1}cm^{-2}$) of the crystal. Using a crystal with a 7.995 MHz fundamental frequency (as used in this study) as an example, a net change of 1Hz corresponds to about 1.36 ng of material adsorbed or desorbed onto the crystal surface of an area of 0.196 cm^2 (the EQCN working electrode area used in this study). The theoretical C_f is shown in Table 2.1

Table 2.1 Theoretical (calculated) sensitivity factor (C_f) of quartz-crystal with respect to the intrinsic frequency

Intrinsic frequency	$(Hz*cm^2)/ng$	$ng/(Hz*cm^2)$	$ng/(Hz*0.196cm^2)$
5MHz	0.056	17.787	3.486
6MHz	0.081	12.352	2.421
7.995MHz	0.144	6.957	1.364
9MHz	0.182	5.490	1.076

The Sauerbrey Equation is only valid in case of a gas or liquid phase. For example, as the density and viscosity of the fluid increase, the f_o decreases. In electrochemical experiments, the Δf are associated with not only the electrochemical process that takes place at the working electrode surface, but also the viscosity of medium, temperature, pressure that the EQCN working electrode are facing. So, it is

very important to understand the origin of Δf in using EQCN in electrochemical study. The theoretical (calculated) value of Table 1 corresponds to the result in gas phase. If the crystal is put in contact with a 'condensed medium' or some film (layer) was coated on the crystal, it affects the shear mode of crystal that results in a decrease of the fundamental vibrational frequency. In addition, when it comes to a porous catalyst layer coated on EQCN working electrode crystal, the crystal's surface roughness and the electrochemical double layer play a significant role in decreasing f_o, not well understood so far though.

In this study, EQCN sensitivity constant was calibrated from cyclic voltammetry experiments. The electrochemical reaction in the Ag electrodepostion-dissolution is shown below;

$$Ag^{+} + e^{-} \longleftrightarrow Ag \tag{2.2}$$

By using Faraday's law,

$$\Delta q = \frac{\Delta m}{M_{Ag}} F \tag{2.3}$$

Where Δq in Ccm^{-2} is the charge measured; Δm in gcm^{-2} is the mass change of Ag during the deposition and dissolution, and M_{Ag} and F are the atomic weight (108 g/mol) of Ag and the Faraday constant (96487 C/mol). By combining the Sauerbrey Equation with the above Equation, the following Equation can be obtained.

$$C_f = \frac{M_{Ag}}{zF} \frac{\Delta q}{\Delta f} \tag{2.4}$$

Where z is the number of electrons transferred in the electrochemical reaction (here n=1 for Ag electro-deposition and dissolution).

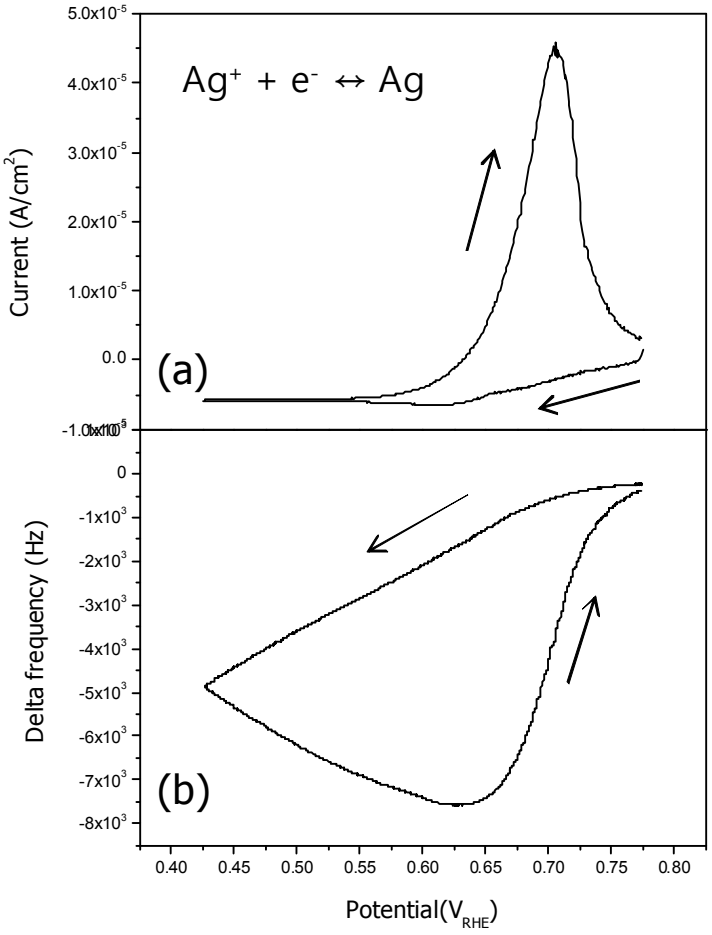

Figure 2.1 CV profile and corresponding quartz-crystal response for Ag deposition and stripping from Pt catalyst layer coated EQCN working electrode in 0.5M H_2SO_4 + 1.5mM Ag_2SO_4 at a scan rate of 1mVs^{-1} at 298K.

Figure 2.1 shows the characteristic CV profile and the frequency response for Ag ion deposition and stripping in 0.5M H_2SO_4 electrolyte. The anodic and cathodic charge density Δq is about 0.437 Ccm^{-2}. As the potential is swept from 0.775 V_{RHE} towards 0.425 V_{RHE}, Ag becomes electrodeposited on Pt catalyst layer and its slope is linear (where Δf slope has negative values with increasing mass). Although the sweep is reversed to anodic direction, the frequency still continues to decrease, indicating a mass increase, until 0.625 V_{RHE} because current flows in the opposite direction and more silver continue to dissolve. Beyond 0.625 V_{RHE}, the current becomes positive (anodic) and the deposited Ag on Pt catalyst layer begins to be stripped and eventually reaches its initial value at the beginning of the cycle. The sensitivity of the EQCN determined by this method was 10.4 ± 0.5 $ngHz^{-1}cm^{-2}$ which is bigger than its theoretical value of 6.957 $ngHz^{-1}cm^{-2}$ because of the thick (about 100 μm) and porous Pt catalyst layer on EQCN working electrode crystal.

Figure 2.2 (a) shows the cyclic voltammogram of Pt catalyst layer on EQCN working electrode taken in 0.5M H_2SO_4 solutions. The background current ($\approx 5.71 \times 10^{-5}$ A) is because of double layer capacitance induced by Pt nanoparticle catalysts with a high surface area. In the region A, a good electrochemical response was confirmed with clear hydrogen adsorption and desorption (H UPD) waves in the region of 0.05 ~ 0.4 V_{RHE}. And the region B (0.4 ~ 0.8 V_{RHE}) is the double layer region of H_2O adsorption/desorption. The region C (> 0.8 V_{RHE}) associate with the formation and reduction of platinum oxide.

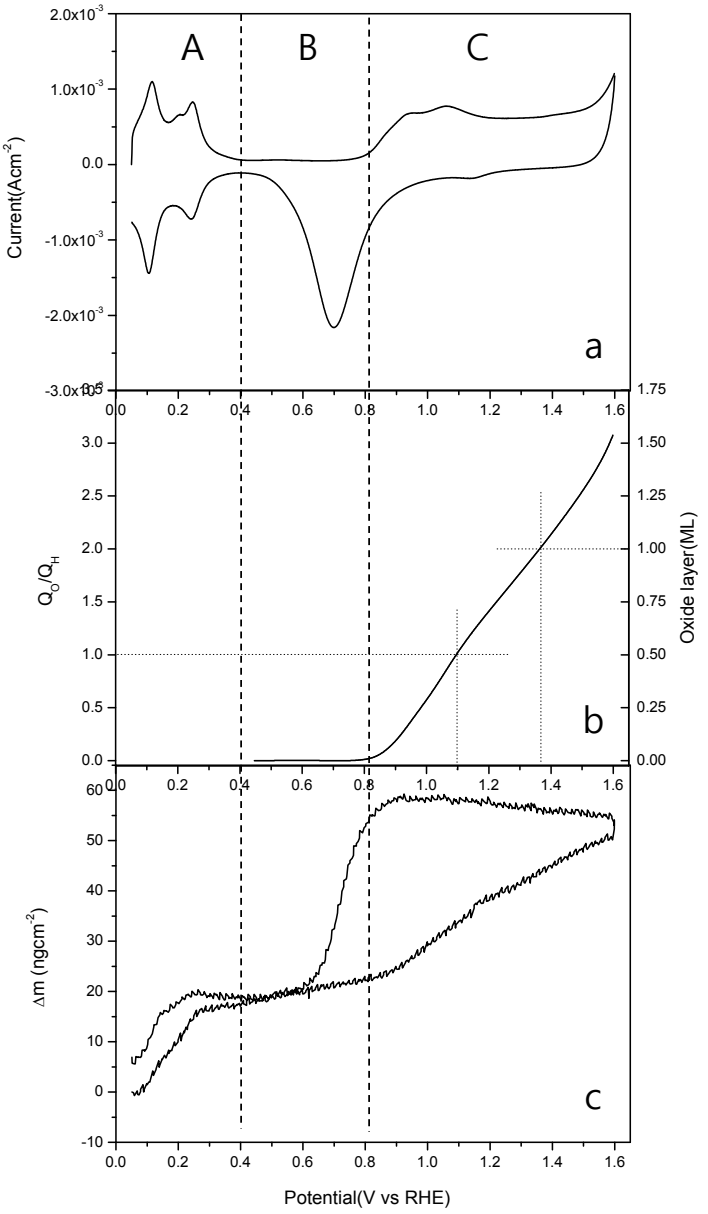

Figure 2.2 Cyclic voltammogram (a), oxide coverage during anodic scan b) and simultaneously recorded mass change (c) of a Pt catalyst layer on EQCN working electrode in the 0.5M H_2SO_4. Scan rate is 100mVs^{-1}

From the Figure 2.2 (b), the degree of oxidation can be quantified by the ratio of oxidation charge (Q_O) and hydrogen adsorption charge (Q_H). The successive oxidation reactions were explained at the introduction part of this paper. The onset potential of Pt-oxide formation is about 0.8 V_{RHE}, and at near 1.1 V_{RHE} the half of Pt surface covered with Pt-O, and at near 1.38 V_{RHE} the surface of Pt is almost fully covered with O species ($Q_O/Q_H = 2$). At the higher potential, higher order oxides such as PtO_2 would be formed ($Q_O/Q_H > 2$).

Figure 2.2 (c) shows the mass changes measured simultaneously during cyclic voltammetry and indicated a continuous mass increase in the anodic scan. As hydrogen desorbs, Δm increases with exchange with water molecules. In the double layer region, the adsorption of SO_4^{-2} or HSO_4^- and additional H_2O molecules adsorption on the active sites previously occupied by hydrogen atoms are responsible for the mass increase of EQCN working electrode (41). And in region C, the increase in Δm is attributed to the formation of platinum oxide.

2.2 Rotating (ring) disk electrode (R(R)DE)

The rotating (ring) disk electrode (R(R)DE) is a widely used method to study electrochemical measurements under well defined mass transport conditions. The rotating disk drags the fluid at its surface and the centrifugal force ‘throws’ the solution outward from the center in a radial direction. This convection force replenishes the electrolyte at the electrode surface by a flow normal to the surface and

brings the reactants dissolved in the electrolyte to the electrode surface. The mass flow to the electrode surface can easily be controlled by the varying the rotation speed. The diffusion coefficients and kinetic parameters of the electrocatalytic reaction can be calculated from the current potential relationship at different rotation speed.

Several different types of experiments are possible at the RRDE; the most common are collection experiments, where the disk generated species is observed at the ring, and shielding experiments, where the flow of bulk electroactive species to the ring is perturbed because of the disk reaction(42). Schematic of the RRDE is shown in Figure 2.3.

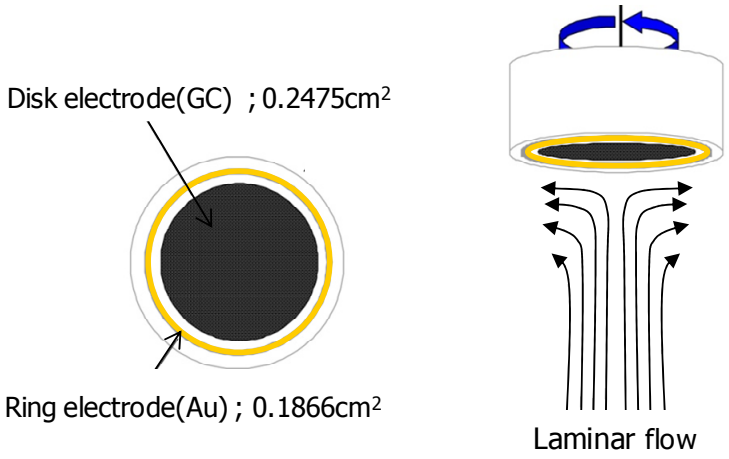

Figure 2.3 Schematic of rotating ring disk electrode with indicated fluid flow

2.3 Scanning electrochemical microscopy (SECM)

The scanning electrochemical microscopy (SECM) was first introduced by Bard and coworkers (43) in 1989 and has received attention due to its excellent ability as an *in situ* technique to investigate interfacial phenomena.

A typical SECM measurement is performed by amperometrical detection of redox species in an ultramicroelectrode (UME) used as a tip electrode positioned at a close distance above a substrate surface. The substrate potential and tip potential are independently controlled by two separate potentiostatic circuits. A nanometer-sized UME tip offer high mass transfer rates under steady state conditions in combination with practically negligible effects of the resistive potentials drop in solution, double layer charging current and low levels of reactant adsorption. The current of redox at the UME tip is governed by the diffusion of redox species. When the tip is far from the substrate, as shown in Figure 2.4 (a), the diffusion limiting steady state UME tip current is given by Equation 2.5 shown below

$$i_{T,ss} = 4nFaD_oC_o^* \tag{2.5}$$

Where n is the number of electrons transferred, F is Faraday's constant, D is the diffusion coefficient, C_o^* is the concentration of redox species and a is the radius of the UME tip.

In the feedback mode of SECM, as the UME tip is approached to the substrate surface, the current from a redox reaction at the UME tip is perturbed by the characteristics of the substrate surface property. For example, when the UME tip

approaches to the electrical insulating substrate such as glass, the diffusion of electroactive mediator (O or R, where only one of the species is present initially in solution) will be partially blocked by the substrate and the resulting UME tip current decreases. This is so called negative feedback, as shown in Figure 2.4 (b). On the contrary, when the UME tip is approaching close to an electrical conductive substrate where the opposite reaction to that on the tip is performed by applying a proper potential, the electroactive mediator that is consumed at tip will regenerated from the substrate. This feedback is called positive feedback (Figure 2.4 (c) that O/R redox couple can be recycled each other between the gap of UME tip and the substrate.

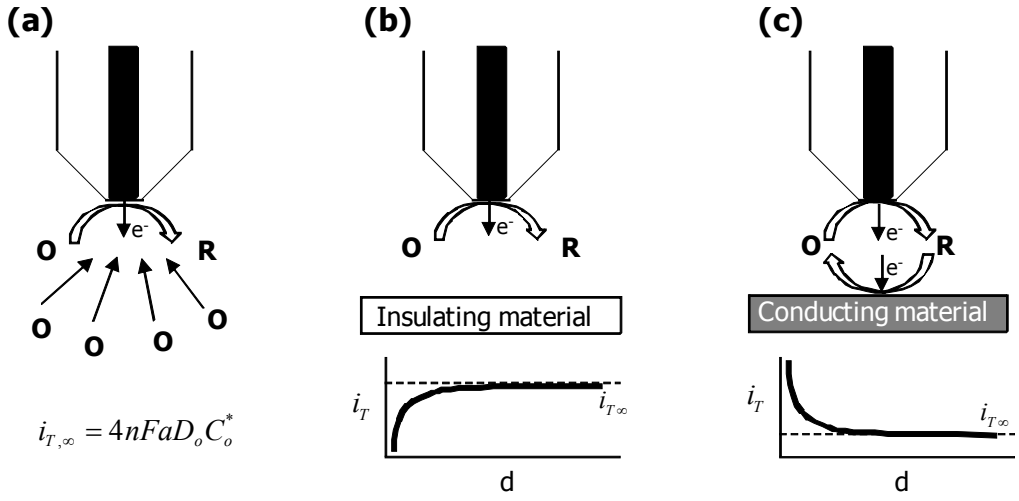

Figure 2.4 Principles of SECM.

(a) With UME far from the substrate

(b) Blocking of diffusion by insulating substrate

(c) Positive feedback at a conductive substrate

In addition to the feedback mode of SECM, tip generation/substrate collection (TG/SC) or tip collection/substrate generation (TC/SG) are also widely used in order to evaluate the mediator property or electrode surface property. For example, in case of TG/SC mode, when species R is stable and UME tip generate an electroactive mediator such as O at a certain potential, this O will diffuse and be electrochemically reduced on the substrate surface if the potential of the substrate is held at reduction potential of species O. By measuring the tip current (i_{tip}) and the substrate current (i_{sub}) as UME tip approaches to the substrate at the same time, we can measure how much electroactive mediator O generated at tip electrode was collected at the substrate by reducing to species R. Generally, in TG/SC mode, the collection efficiency shows very high value about 99% because almost of species O generated at tip can be collected at the substrate which usually has bigger diameter than tip electrode, not escaping from the very narrow gap that has $L(d/a) \approx 0.1$ where d is distance of gap between tip and substrate, a is radius of tip electrode. Contrast this behavior with that at the RRDE, where even with close spacing between disk and ring and with a large ring, the collection efficiency is usually much smaller, because some disk generated product always diffuses away before being collected by the ring.

It is also possible to carry out tip collection/substrate generation (TC/SG). However there are some shortcomings if the substrate is larger than tip electrode. The first, the process at large substrate is always non-steady state, and the second the collection efficiency will be lower than that of TG/SG mode and finally a large

substrate current will cause significant iR-drop. So, the TG/SC mode is favorable for kinetic measurements, while TC/SG is preferred for monitoring enzymatic reactions, corrosion and other heterogeneous processes at the substrate surface.

2.3 Inductively coupled plasma mass spectrometry (ICP-MS)

An inductively coupled plasma mass spectrometer (ICP-MS) invented in the late 1980's is an element analytic instrument capable of determining nearly all elements in the periodic table at limits of detection in the parts per quadrillion and with a linear analytical range over 8-10 orders of magnitude. ICP technology was built upon the same principles used in atomic emission spectrometry. Samples are decomposed to neutral elements in high temperature argon plasma and analyzed based on their mass to charge ratios. An ICP-MS can be thought of as four main processes, including sample introduction and aerosol generation, ionization by an argon plasma source, mass discrimination, and the detection system. The schematic illustrates this sequence of processes in Figure 2.5 (a, b).

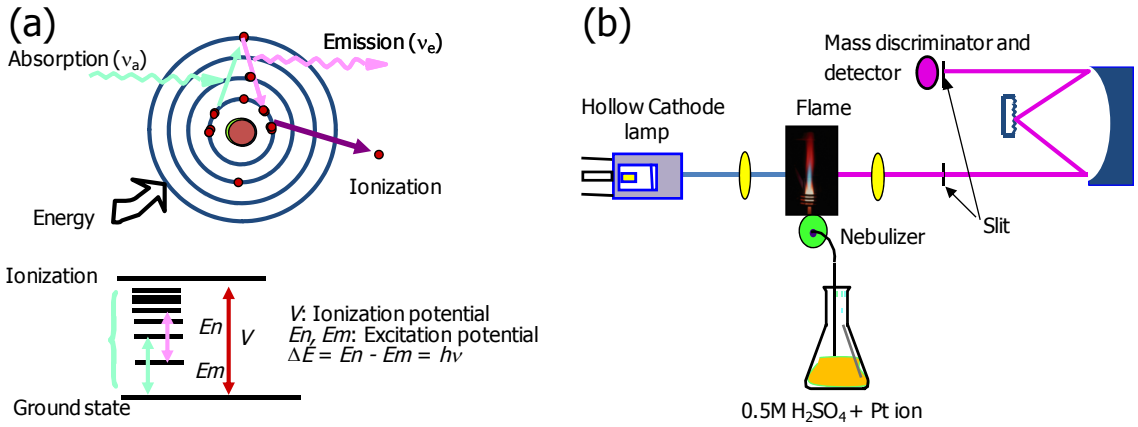

Figure 2.5 (a) Principles of atomic spectroscopy

(b) Schematic of ICP-MS analysis (Optimass 8000, GBC sci. Inc.)

CHAPTER 3

The influence of hydrogen and cation under potential deposition on oxide-mediated Pt dissolution in proton exchange membrane fuel cell

3.1 INTRODUCTION

Proton-exchange-membrane fuel cells (PEMFCs) have attracted attention as energy conversion devices for electric vehicles, small-scale stationary power generation, and portable electronics devices (8). One of the key challenges to PEMFC commercialization is the gradual loss of cell performance over time, which limits the device lifetime over which the fuel cell can operate to the required power and efficiency. In particular, the deterioration of the PEMFC's performance by degradation of the electrocatalysts is a major problem. The catalyst degradation in the cathode has been studied extensively, and is generally agreed to be related to three major mechanisms: i) Ostwald ripening (Pt dissolution and redeposition onto lower surface energy sites) (28-29) ii) coalescence of Pt nanoparticle via Pt migration and surface diffusion on the carbon support (23, 28, 35) iii) carbon corrosion-induced Pt detachment or agglomeration (44).

Although electrode kinetic properties are frequently measured on pristine catalyst surfaces, PEMFC cathode electrocatalysts are commonly covered by oxide films that may have a profound influence on the chemistry, stability and kinetics of the oxygen reduction reaction, under the potential range where the electrodes normally operate. While experimentation and discussion continues, a consensus of

sorts has emerged that suggests strong physisorption of water on the platinum surface in the range of 0.27 - 0.85 V_{RHE}, followed by formation of a PtO layer in the range of 0.85 - 1.15 V_{RHE}, and a formation of a PtO_2 layer at even higher potentials (30, 45-47).

Mitsushima (17, 48) and Guilminot (49) reported the formation of PtO_2 at potentials more positive than 1.5 V_{RHE}, and noted that PtO_2 is formed by further oxidation of an existing thin layer of PtO, resulting in a two-layer film. Sun *et al.* (50) also proposed that a two-layer oxide structure existed with the inner layer (PtO) in the potentials region of 1.0 $V_{RHE} < E_H < 1.35$ V_{RHE} and an outer layer containing (PtO_2) in the potentials at potential greater than $E_H > 1.35$ V_{RHE}.

Furthermore, it has been noted that potential cycling accelerates the rate of surface area loss in PEMFC operation; potential cycling has been standardized as an accelerated testing protocol for membrane-electrode assembly durability by the Department of Energy. There are several experimental studies that show that cycling the potential of platinum electrodes to a range in which oxides are formed and subsequently stripped results in a loss of electrochemically active surface area (ECSA) that is more rapid than holding the potential at either the upper or lowter potential limit (32, 51-53). Researchers have therefore proposed that the presence of oxide can, in effect, passivate the surface, and protect platinum form the dissolution rates that would be expected at more positive potentials (29, 54). If platinum dissolution occurs through an electrochemical mechanism such as electrochemical oxidation of Pt, i.e.,

$$Pt \rightarrow Pt^{z+} + ze^{-} \quad (3.1)$$

One expects higher equilibrium concentrations of the mobile Pt ion in solution at more positive potentials. Wang *et al*. (29) conducted a series of experiments in which platinum is held at fixed potentials until an equilibrium concentration in solution is reached, and observed that the platinum concentration in solution increased with the electrode potential up to about 1.1 V_{RHE}, but observed a marked decrease in solution-phase Pt concentration at more positive potentials; their results suggest a protection of the surface from the direct electrochemical dissolution mechanism at potentials where the surface is fully covered by oxide and a lower equilibrium concentration of the mobile species in the presence of oxide. While the literature suggests that the presence of oxide can help to protect the platinum surface from anodic dissolution at higher potentials, there are still open questions about the nature that the oxide film plays, and the mechanism of Pt dissolution: whether oxide-mediated dissolution occurs primarily on oxidation or reduction of the film, and which mobile platinum species are formed in the dissolution process.

In this study, in order to understand the Pt dissolution rate and to help clarify the likely mechanism(s) of Pt dissolution, a variety of electrochemical techniques are used in combination with ICP-MS to clarify the surface state of Pt during electrochemical experiments, to confirm that both methods give equivalent results under identical potential cycling or potential sweep conditions. We examined specifically the influence of potential limits in cycling in an attempt to corroborate

measurements made by Mitsushima *et al*. (17), and showed what we believe to be very good agreement between EQCN and ICP-MS experiments. This agreement allowed us to assess mass loss over a relatively small number of cycles, and indicates that mass loss of the sample is matched by dissolution of platinum ion from electrode to the solution. When confronted with the rather surprising result that cycling to lower potentials somehow protects the surface in the subsequent cycle, we examined the role of adsorption of various cations at these lower potentials. It has been established that Zn UPD changes the nature of the H UPD region by surface reordering or blocking in this potential region (55-56); we sought to examine whether this surface reordering would have an effect on the result reported by Mitsushima *et al*. that cycling into the H UPD region resulted in lower levels of Pt loss than cases in which the lower potential limit was maintained above the H UPD region. We report these results in an attempt to clarify the deterioration mechanism and the influence of cation UPD on Pt catalysts in acid media. In an attempt to detect more precisely the nature of the mobile species that dissolves and under what potential conditions that mobile species detaches from the platinum surface, we carried out a series of experiments on the formation and stripping of Pt oxide by using RRDE experiment in combination with ICP-MS analysis.

3.2 EXPERIMENTAL

3.2.1 Preparation of thin film Pt catalyst layer for EQCN and RRDE test

The catalyst layer of the EQCN and RRDE working electrode was fabricated by dispersing 32 mg of Pt-black catalyst (E-Tek) and 182.4 mg of 5 wt% Nafion solution (Aldrich) in a mixture of 2 ml of isopropyl alcohol and 4.8 ml of distilled pure water. The mixture was ultrasonicated until a dark homogeneous dispersion was formed (~1hr). Then 8 ul of the dispersed ink solution was dropped onto the glassy carbon (GC) disk electrode for RRDE or AT-cut Au quartz crystal for EQCN to give a catalyst loading of 35,800 ng. The loadings were 188.5ug/cm^2 for EQCN experiments and 144.6 ug/cm^2 for RRDE experiments, owing to the different electrode sizes. The electrodes were subsequently dried in an atmosphere of ultra pure N_2 gas (99.999 %).

3.2.2 EQCN flow cell system and electrochemical measurement

Figure 3.1 shows the EQCN flow cell system composed of a quartz crystal analyzer (Maxtek RQCM, INFICON Inc.), gear pump and a potentiostat (CHI760C, CH Instruments Inc.) controlled by a personal computer through a general purpose interface bus. During all measurements, the mass change resulting from the oxidation and reduction of Pt was measured by EQCN. The EQCN cell consists of a working electrode (7.995 MHz AT-cut Au quartz crystal, 0.196 cm^2 of geometric area, ICM Inc.), Hydrogen reference electrode (HydroFlex, Gaskatel GmbH Inc.) and Pt wire counter electrode. All the potential values were indicated with respect to the RHE.

The electrolyte solution from a reservoir was delivered to the EQCN cell at a volumetric rate of 122.5 mm^3/sec with a gear pump (Cole Palmer) with a retention time of 0.27 sec. The 0.5 M H_2SO_4 electrolyte solution was de-aerated with bubbling high purity N_2 gas for 1hr before the beginning of the electrochemical test, and continuous purging was done during the experiment.

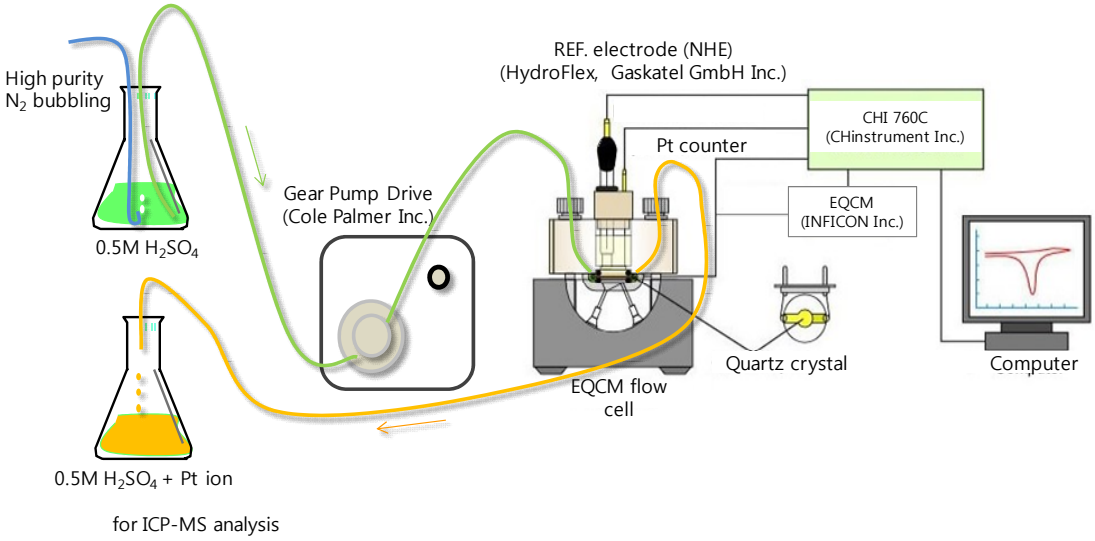

Figure 3.1 Schematics of the EQCN flow cell system

Prior to the measurements, the working electrode was pretreated by a potential cycle between 0.05 ~ 1.0 V_{RHE} at a rate of 100 mVs^{-1} for 20 cycles. The triangle wave voltammetry (TW) and square wave voltammetry (SW) of the EQCN working electrode was performed at a scan rate of 500 mVs^{-1} and 1 Hz of frequency for 500 cycles with respect to the lower (E_L) and upper (E_H) limits on the potential. Before each cycling test, a LSV (linear sweep voltammogram) was conducted at a scan rate

of 100 mVs^{-1} immediately before the TW testing to make a measurement of the electrochemical active area (ECSA). For the experiments examining the effects of other dissolved cations, 0.5 M H_2SO_4 electrolytes containing 5mM of fully dissolved cations were prepared using analytical grade Aldrich reagents; $ZnSO_4$, Li_2SO_4, Na_2SO_4, K_2SO_4, $CdSO_4$.

The sensitivity factor for the EQCN was determined following the method described by Vatankhah *et al.* (57). This method is the silver electrodeposition-electrodissolution processes by cyclic voltammetry. All the electrochemical experiments were conducted in 0.5 M H_2SO_4 solution containing 1.5 mM of analytical grade Ag_2SO_4(Fisher Scientific) at T ≅ 298 K. The cyclic voltammetry profiles for silver deposition and stripping on thin film Pt catalyst layer were recorded in the potential range 0.425 ~ 0.775 V_{RHE} at 1 mVs^{-1} scan rate. The calibration constant of the EQCN determined by this method was 10.40 ±0.53 $ngHz^{-1}cm^{-2}$, which is bigger than its theoretical value of 6.957 $ngHz^{-1}cm^{-2}$ because of the thickness (about 100um) and porosity of the Pt catalyst layer on the EQCN working electrode crystal. The presence of Nafion in the electrode structure might preclude a completely rigid structure as we assume during calibration and could obscure interpretation of the results within a single cycle, good agreement between EQCN and ICP analysis (discussed below) suggests that the loss over multiple cycles can be quantified with this technique.

3.2.3 Rotating Ring-Disk Electrode (RRDE) measurement

The reaction mechanism of Pt dissolution was investigated using a RRDE. A GC disk – Au ring electrode (E7R9, PINE Inc.) was used; the geometric surface areas of the disk and ring electrodes were 0.2475cm^2 and 0.1866 cm^2 respectively with a theoretical collection efficiency of N=0.37 ($N = |i_{Ring}|/|i_{Disk}|$). The RRDE experiment for determining the real collection efficiency was carried out by using 1 mM of ferrocenemethanol (97% FcMeOH, Sigma Aldrich) in 0.1 M sodium nitrate ($NaNO_3$, sigma Aldrich) solution with N_2 bubbling and oxygen reduction reaction (ORR) shielding effect. This method will be discussed at results and discussion section. The rotating speed of the electrode was adjusted to 0, 800, 1600, 2500 and 3000 rpm using a speed controller (Modulated Speed Rotator (MSR), PINE Inc.).

100ml of 0.5 M H_2SO_4 electrolyte solution was de-aerated or aerated with vigorous bubbling of high purity N_2 gas for 1hr before the beginning of the electrochemical test and continuous purging was done during the experiment. Prior to the measurements, the working electrode was pretreated by a potential cycle between 0.05 V ~ 1.0 V_{RHE} at a rate of 100 mVs^{-1} for 20 cycles with the condition of N_2 bubbling. The hydrogen electrode (HydroFlex, Gaskatel GmbH Inc.) and Pt wire electrode were also used as reference and counter electrode.

3.2.4. ICP-MS measurement

At the end of each electrochemical experiment, the solutions were analyzed by using ICP-MS (Optimass 8000, GBC Scientific Inc.) to determine the amount of

dissolved Pt in solution. The detected Pt ion concentration is around 1 ppb – 100 ppb with respect to the potential cycling condition and N_2 or O_2 saturated solution. All glassware was cleaned by dipping in 4 M of nitric acid for at least 12 hr and rinsed with DI water before using. The ICP-MS system had a detection limit of 0.1 ng/L for Pt ions.

3.3 RESULTS AND DISCUSSION

3.3.1 Determination of real collection efficiency of RRDE.

The theoretical collection efficiency of the RRDE used in this study is 0.37. However, because Pt catalyst thin-film coated GC disk electrode in this RRDE test is not even, the real collection efficiency is hardly to be coincidence to the theoretical value. In generally, reversible mediators such as ferrocenemethanol can be used for RRDE electrode collection efficiency measurement.

Figure 3.2 (a) shows example for collection efficiency measurement. The RRDE electrode (bare GC disk_Au ring) was dipped into 1 mM ferrocenemethanol as electroactive mediator in 0.1 M $NaNO_3$ solution and rotated under a rotation rate (i.e. 400, 800, 1600 rpm). Disk potential E_{disk} was scanned 0.3 ~ 0.8 V_{RHE} with 10 mVs^{-1} scan rate, ring potential E_{ring} was fixed at 0.3 V_{RHE} which is the reduction potential of ferrocenemethanol. The ratio of $|i_{Ring}|/|i_{Disk}|$ shows a constant value of 0.38 under various rotating speed (Figure 3.2 (d)). This value is quite near to the theoretical collection efficiency of 37%.

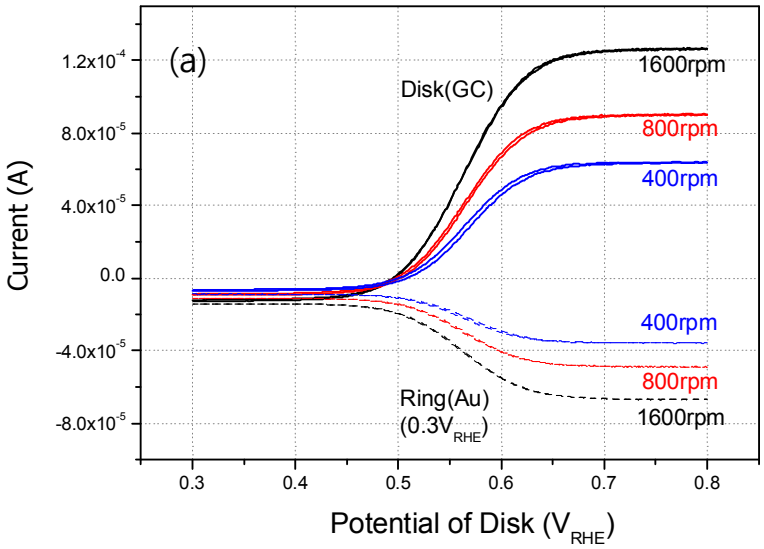

Figure 3.2 (a) i_{Disk} & i_{Ring} vs E_{Disk} , GC disk_Au ring,
10 mVs^{-1} in 1 mM FcMeOH and 0.1 M $NaNO_3$ solution.

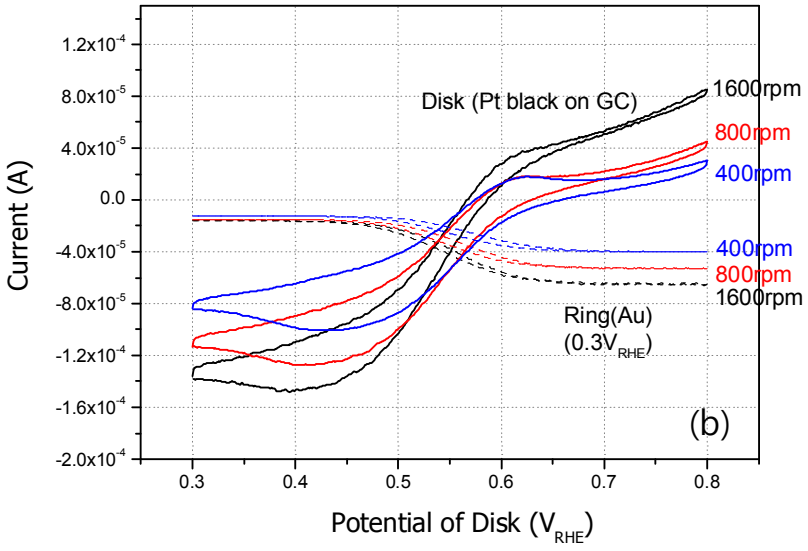

Figure 3.2 (b) i_{Disk} & i_{Ring} vs E_{Disk} , disk : Pt black catalyst film on GC, ring : Au
Scan rate : 10 mVs^{-1} in 1 mM FcMeOH and 0.1 M $NaNO_3$ solution.

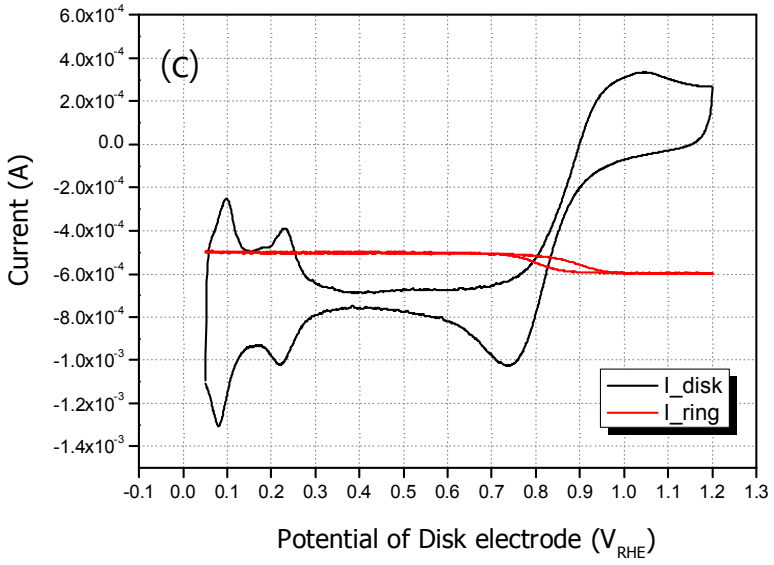

Figure 3.2 (c) i_{Disk} & i_{Ring} vs E_{Disk} , disk : Pt black catalyst film on GC, ring : Au
Scan rate : 50 mVs^{-1} with 1600 rpm in O_2 saturated 0.5 M H_2SO_4.

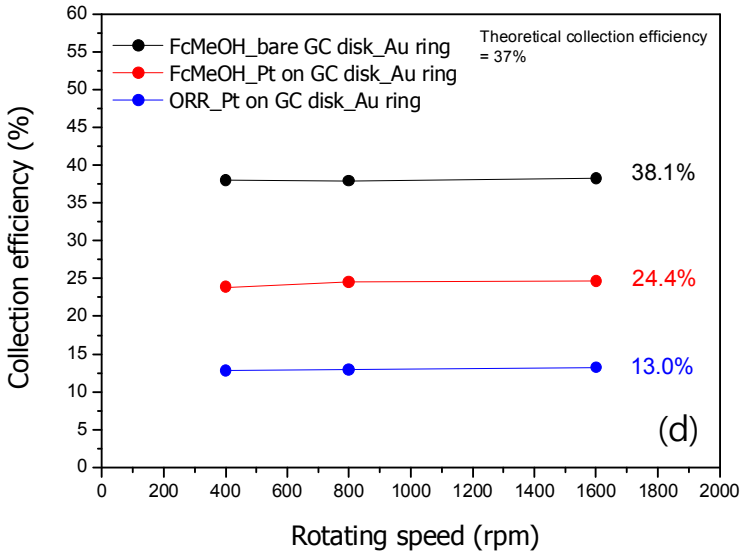

Figure 3.2 (d) Measured collection efficiency with various rotation speeds.

Figure 3.2 (b) shows the same test only except that Pt catalyst thin film was coated on GC disk electrode. Unlike the bare GC disk electrode, the disk current shows huge hysteresis due to the uneven surface morphology and large portion of pore volume inside the catalyst thin film. In spite of observed hysteresis in disk current, the measured collection efficiency reveals a constant value of 0.244 for various rotation speeds, which is lower than the theoretical value of 0.37. However, we must note that this 24.4 % is not attributed to just Pt surface area, but also uncovered bare GC surface.

Hence, we identified oxygen as a mediator which is electroactive only on Pt, not on GC. If there is only the oxygen reduction reaction ($O_2 + 4H^+ + 4e^- \rightarrow 2H_2O$) at ring electrode in the acid solution at 0.4 V_{RHE} of Pt ring electrode, the ring current by ORR would be strongly influenced by oxygen consumption rate at the disk electrode like Equation 3.2 (42)

$$i_{Ring} = nFD_{O_2} 2\pi \int_{r_2}^{r_3} \left(\frac{\partial C_{O_2}}{\partial y}\right)_{surface(y=0)} rdr \tag{3.2}$$

Where r_2 and r_3 are the inner radius and outer radius of ring electrode, respectively (r_2 = 3.13mm, r_3 = 3.96mm in this study). And the decreased ring current due to oxygen flux decrease by shielding effect of ORR at disk electrode can be expressed by Equation 3.2

$$i_{Ring,decreased} = N \times i_{Disk,ORR} \tag{3.3}$$

So, if we know the limiting ring current ($i_{Ring,\lim}^{i_{Disk,ORR}=0}$) when the disk current by ORR is zero ($i_{Disk,ORR}=0$) and the limiting current ($i_{Ring,\lim}^{i_{Disk,ORR}=0}$) when the disk current by ORR is maximum ($i_{Disk,ORR,\lim}$), we can determine the collection efficiency (Equation 3.4) of RRDE by plugging Equation 3.2 to Equation 3.3.

$$i_{Ring} = i_{Ring}^{i_{Disk,ORR}=0} - i_{Ring,decreased} = i_{Ring}^{i_{Disk,ORR}=0} - N \times i_{Disk,ORR} \tag{3.4}$$

$$N = \frac{i_{Ring}^{i_{Disk,ORR}=0} - i_{Ring}^{i_{Disk,ORR},\lim}}{i_{Disk,ORR,\lim}} \tag{3.5}$$

Figure 3.2 (c) shows the current response at the Pt thin film on GC disk electrode (black) and Pt ring electrode (red) during disk potential scan at 50 mVs^{-1} in O_2 saturated 0.5 M H_2SO_4. We could estimate $i_{Disk,ORR,\lim}$ from the center of the narrowest part of the double layer region (around 0.4 V_{RHE} of disk potential) and $i_{Ring,\lim}^{i_{Disk,ORR}=0}$, $i_{Ring}^{i_{Disk,ORR},\lim}$ was determined from the average value of i_{Ring} in the range of 1.1 ~ 1.2 V_{RHE} and from the range between 0.3 ~ 0.4 V_{RHE}, respectively. The calculated collection efficiency by this method is shown at Figure 3.3 (d) to be 13% which is much less than the theoretical value of 37 % and 24.4 % by using 1mM FcMeOH.

3.3.2 Pt dissolution rate under potential cycling in terms of potential limits

We begin our discussion of experimental results with a summary of how cycling conditions affect the rate of platinum mass loss from the electrode. As mentioned in the introduction, Wang *et al*. (29) showed that the concentration of dissolved Pt increases monotonically from 0.65 V_{RHE} to 1.1 V_{RHE}, and then decreases

at potentials higher than 1.1 V_{RHE} due to the stable protective PtO, PtO_2 layers. In their experiments, they allowed the surface to remain at the specified potential for sufficient hold duration to approach a true equilibrium condition. However, under transient conditions as in potential cycling, the dissolution rate has been shown to accelerate with respect to both scan rate and potential limits (17). Indeed, under transient conditions, the platinum might not be in the equilibrium state dictated by local potential conditions. As such, dissolution might proceed to a point well beyond that which is predicted by thermodynamic considerations alone, as the solution is equilibrating with a surface that is not at a thermodynamic equilibrium state as designated by the potential.

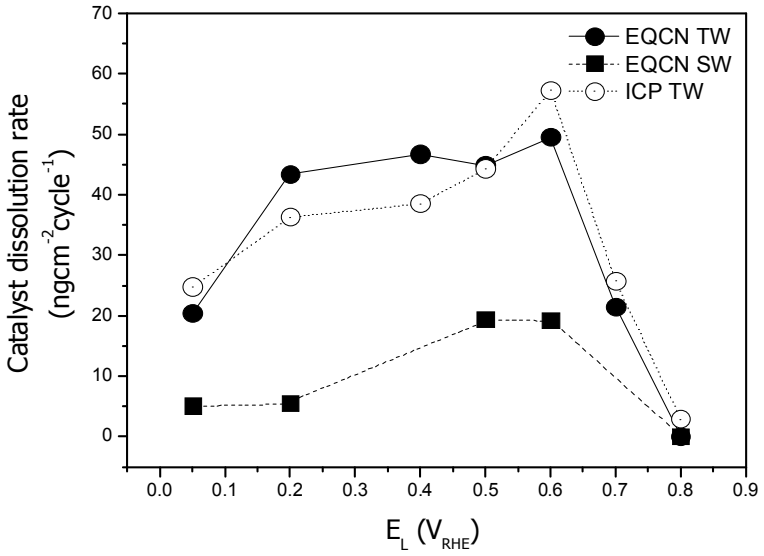

Figure 3.3 Pt dissolution rate as a function of E_L with E_H =1.6 V_{RHE} at 298K in 0.5M H_2SO_4 for 500mVs^{-1} triangular-wave cycling (TW) and 1Hz square-wave cycling (SW) for 500 cycles.

Figure 3.3 shows the Pt dissolution rate as a function of the lower potential limit for cycling, $E_{L,}$ with the upper limit, E_H, fixed at 1.6 V_{RHE} both for cyclic voltammetry with a scan rate of 500 mVs^{-1} and for square wave voltammetry at 1Hz, over the course of 500 cycles. The dissolution rate obtained by both analysis method (EQCN & ICP) is 45-55 $ngHz^{-1}cm^{-2}$; we found the measurements by the two methods to be in good agreement with each other. These values are larger than the results presented in other papers (17, 58) that used a Pt planar working electrode electrodeposited onto EQCN quartz crystal and a stagnant electrochemical cell. The difference can be explained by the high roughness factor of Pt catalyst layer, and from fresh electrolyte feeding from the reservoir; the enhanced surface area and the inability of the solution to become saturated with mobile ionic platinum species ensures a higher rate of dissolution.

The Pt dissolution rate trend reveals that cycling between two potentials that are both sufficiently high so as to maintain oxide on the surface over the course of the entire cycle results in a rather modest effective dissolution rate. Consistent with other data in the literature, if the lower potential limit is low enough for the oxide to be stripped, we regenerate a bare platinum surface, which is much more prone to subsequent dissolution, during intervals when the potential is raised to higher values, but before the protective oxide layer is formed.

Previous analysis suggested that platinum solubility would increase with potential but that the oxide equilibrates with a much lower concentration of dissolved platinum than the platinum metal (54). As such, one would expect the effect of the

lower potential limit on overall dissolution to be quite modest compared to the influence of whether the protective layer is repeatedly removed before exposing the platinum to higher potentials. Yet, cycling with a lower potential limit in the range of H UPD appears to lower the cyclic dissolution rate significantly below that which is revealed when the lower limit is in the oxide- and H UPD-free region. This observation will be discussed in greater detail in chapter 3.3.3.

We found a broad maximum of loss with a lower potential limit in the range of 0.2 ~0.6 V_{RHE} by both *in-situ* EQCN measurement and *ex-situ* ICP-MS analysis. This is a somewhat surprising result, though it does corroborate measurements made by Mitsushima *et al*. (17) As the solubility of platinum is predicted to be quite low at the low values of the potential where H UPD occurs, we would not expect the adsorbed hydrogen to play a major role in protecting the surface as the oxide does, as the potentials at which oxides are present are potentials at which the solubility of platinum in solution is expected to be much higher. We note that the trend is in place for both triangular wave (TW) and square wave cycling (SW), indicating that the total time spent at lower potentials or traversing the oxide-free region is not the controlling factor. Some clues as to the mechanism of Pt dissolution can be gleaned from the plot of dissolution versus E_L in Figure 3.2. First, the region of $0.3 < E_L < 0.7$ V_{RHE} and $E_L > 0.7$ V_{RHE} can be explained by surface oxide properties that are strongly related to Pt-oxide formation. The surface state of Pt is a very important factor that influences its electrocatalytic behaviors such as kinetics, thermodynamics that influence with the activity, dissolution, migration, and agglomeration. The literature suggests that two

types of Pt-oxide film, PtO and PtO_2 were formed during the anodic scan of cycling. The PtO was formed in the potential range of E_H = 1.2~1.4 V_{RHE} and PtO_2 in the higher potential range above 1.5 V_{RHE} by further oxidation of the already existing PtO layers. PtO is regarded as thin monolayer and PtO_2 is a thick, highly hydrated, porous, polymer-like layer (30). PtO oxide films is reduced in the potential range of 0.6~0.8 V_{RHE} and PtO_2 oxide film under a more negative potential range than PtO reduction potential.

Figure 3.4 shows Pt catalyst ECSA loss (a), mass loss (b) after the potential cycling test by changing the upper potential limit E_H and rotating speed with the E_L=0.5 V_{RHE}, for scan rates of 500 mVs^{-1}. We note that an increase in the rotation speed results in an increase in the mass loss rate Pt catalyst mass loss at upper potential limits above 1.2 $V_{RHE,}$ whereas we see negligible difference when the upper potential limit is kept below 1.2 V_{RHE} E. It should be noted that when the upper potential limit is sufficiently high to form PtO_2 on the electrode surface (generally considered to be at potentials more positive than 1.5 V_{RHE}), there is a mechanism by which the oxide can be reduced electrochemically to form a mobile species (24, 52), namely:

$$PtO_2 + 4H^+ + 2e^- \rightarrow Pt^{2+} + 2H_2O \qquad (3.6)$$

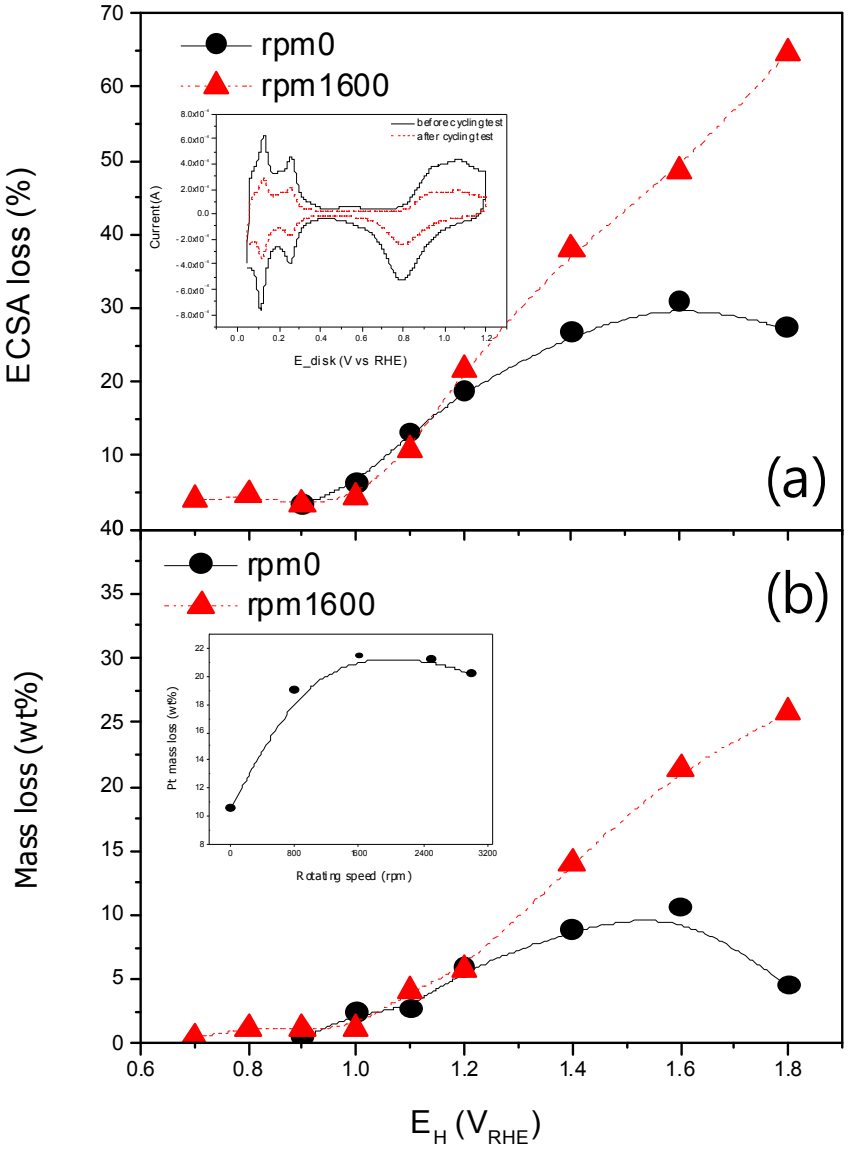

Figure 3.4 Pt ECSA loss (a) and mass loss (b) analyzed by ICP-MS with a changing upper limit potential (E_H), with lower limit potential (E_L) fixed at 0.5 V_{RHE}, for scan rates of 500 mVs^{-1}.

Inset of (a) : CV before and after cycling test, inset of (b) : Pt mass loss (wt%) at various rotating speed measured by ICP-MS

This mechanism certainly might contribute significantly to mass loss for cycling experiment where the upper potential limit is sufficiently high to generate PtO_2, but does not likely play a role at upper potential limits below the formation of PtO_2. While not conclusive, the difference in dissolution rate at more positive upper potential limits suggests the generation of mobile species that might redeposit in the case of a stagnant solution, but which are removed from the point of generation by convection at higher rotation speeds.

From these experiments, we see the effect of potential cycling on the overall dissolution rate, and consistent results among various detection techniques. There is evidence to suggest again the protective nature of the oxide film, though there is also a strong likelihood that potential cycling to sufficiently positive potentials such that PtO_2 is generated will result in the direct dissolution of the oxide film, thereby contributing to Pt loss, though this mechanism is unlikely in the range of $E_H < 1.2$ V_{RHE}.

3.3.3 Pt dissolution during reduction of Pt oxide

We also wanted to investigate whether we might determine the nature of the species that are liberated and contribute to the mass loss. As such, we conducted RRDE experiments to detect the nature of species that are liberated from the platinum electrode upon cycling. Figure 3.5 shows the result from RRDE experiment in 0.5M H_2SO_4 at a scan rate of 50 mVs^{-1}. The Figure 3.5 (a) is I_{disk}-E_{disk} and the Figure 3.5 (b) is I_{ring}-E_{disk} at $E_r = 1.4$ V_{RHE}. We see that the main effects of increasing the upper

potential limit of the disk electrode are an increase in the oxidation charge at ring electrode during the cathodic sweep of E_{disk} and a shift of the oxidation peak potential of the ring electrode toward less positive values, in accordance with the reduction peak potential shift of disk electrode in Figure 3.5 (a).

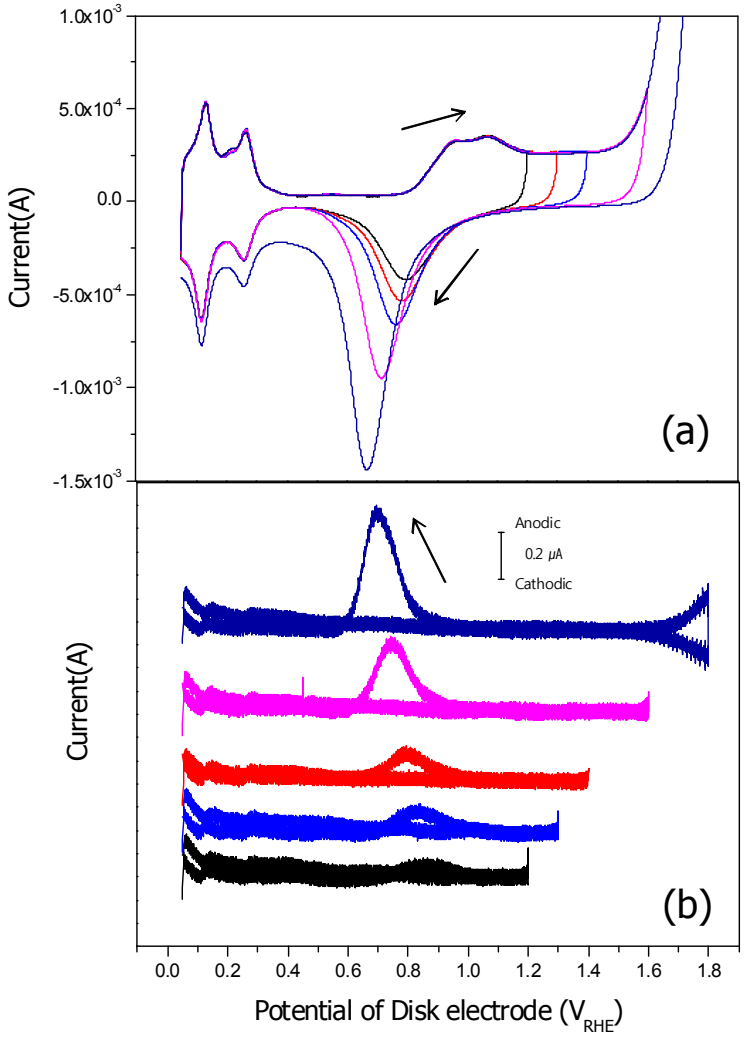

Figure 3.5 RRDE measurement at various E_H under N_2-saturated 0.5M H_2SO_4, scan rate of 50 mVs^{-1}, ω=3000 rpm
(a): I_{disk} - E_{disk}, (b): I_{ring} - E_{disk} (E_{ring} = 1.4 V_{RHE})

These results are similar to the interpretation of experiments by Johnson *et al* .(52) who suggested that the wave in the Figure 3.5 (b) result from the electrochemical oxidation of Pt^{2+} at the ring electrode as this species is generated at the disk electrode by the electrochemical reduction reaction shown by the reaction described in Equation 3.1. Based upon these experiments, oxidizable Pt species in solution appear to be generated at the disk only during the reduction of the oxide peak.

We also note that experiments in which the ring was held at very low potentials did not reveal any significant current signatures as the disk potential was cycled: no reducible forms of Pt were observed under any conditions. The results in Figure 3.5 (b) suggest that the cathodic dissolution of PtO_2 is enhanced by an increase of the upper limit potential at disk electrode up to 1.8 V_{RHE}, likely due to the increase in the amount of PtO_2(50).

Figure 3.6 shows the Pt mass loss based on the calculation of oxidation charge at ring electrode (E_r = 1.4 V_{RHE}) during cathodic scan in N_2 saturated 0.5 M H_2SO_4. The ring oxidation tests were conducted at discrete cycles (cycle numbers 0, 50, 100, 200, 300, 400, 500) during the Pt dissolution test in the same reactor. The potentiostat controlling the ring potential was only active during those particular cycles. The ring should therefore have been electrochemically inert during other cycles. Based upon the efficiency of the RRDE used in the experiment ($N=0.13$) and Faraday's law ($\Delta Q=n*F*\Delta m/M_{pt}$), the amount of soluble Pt species at disk electrode generated during cathodic scan can be calculated. For the purposes of this calculation, we

assumed a mobile Pt^{2+} species, resulting in n=2 for oxidation to Pt^{4+} at the ring electrode. The shaded area below the line in Figure 3.6 represents the total amount of soluble Pt species generated during cathodic scan of potential cycling test and its value is 360.6 ng. There is a possibility that there were some cycles that released a much higher quantity of electroactive Pt species into solution that this test did not reveal, but we found no evidence of anything other than the fairly unremarkable trend in detectable Pt species indicated by Figure 3.5. The total amount of Pt detected at the ring corresponds to just 4.99 % of total Pt mass loss during the potential cycling test of 0.5 -1.6 V_{RHE}, 500cycle, 500mV/s in N_2 saturated 0.5 M H_2SO_4.

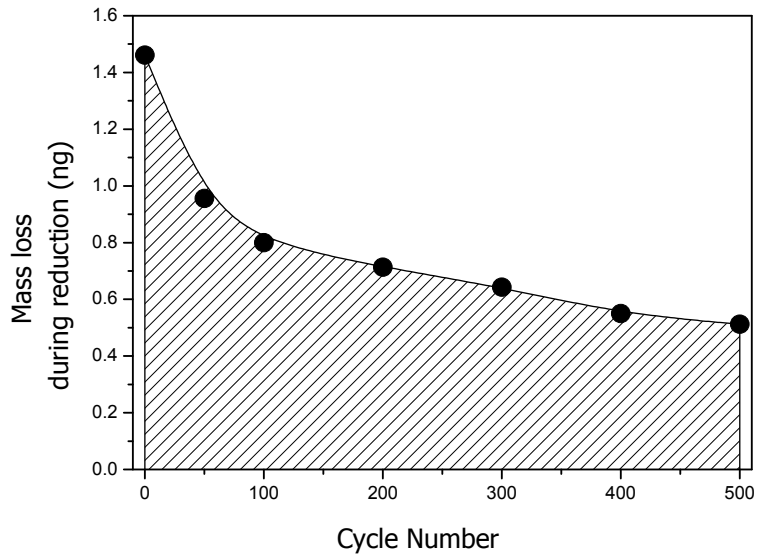

Figure 3.6 Pt mass loss (ng) calculated by the integrated oxidation charge at ring electrode during cathodic scan (50mV/s in N_2 saturated in 0.5M H_2SO_4). The collection efficiency of the RRDE is 0.13, and the assumption of the charge associated with mobile Pt species is *n*=2.

Figure 3.7 attempts to show the relative values of the mass loss from EQCN testing, the total Pt put into solution via ICP-MS (circle) after EQCN flow cell testing, ICP-MS (square) after RRDE testing, and integrated Pt mass loss (triangle_line) from Figure 3.6. The change in mass from EQCN testing corresponds to ~12% mass loss over the course of 500 cycles, and corresponds very well with the independent measurement of ICP-MS testing of the solution after those same 500 cycles.

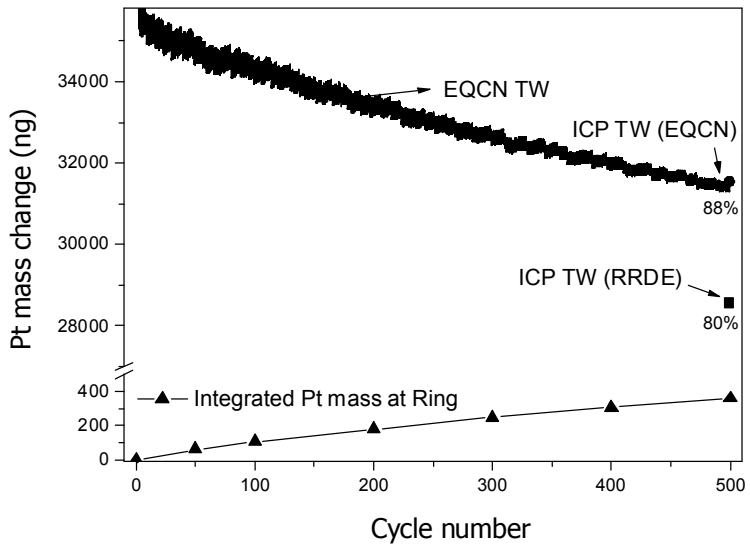

Figure 3.7 Total Pt mass change vs. cycle for in-situ EQCN, ICP-MS (EQCN) after EQCN test, ICP-MS (RRDE) after RRDE test and integrated Pt mass loss (ng) from Figure 3.6. EQCN and ICP-MS experiments reveal original electrode mass remaining; integrated Pt mass loss reveals mass lost to solution.

We note that there is slightly greater mass loss, as measured by ICP-MS in RRDE experiments over the course of 500 cycles: a mass change of roughly 20%,

corresponding to 80% mass remaining. We show for comparison (on a much enlarged scale) the integrated mass detected at the ring electrode for RRDE experiments. Note that for EQCN and ICP-MS results, the data shown is for initial mass of Pt remaining as a function of cycle number or at the end of the experiment; for the mass detected at the ring electrode, it is an estimate of the total mass lost.

We note that even if our assumption that Pt^{2+} and n=2 is incorrect in the prediction of mass loss from the disk is incorrect, we cannot account for the total amount of mass lost from the disk by any reasonable combination of Pt dissolution and subsequent oxidation reactions. We believe that this discrepancy suggests either a highly irreversible electrochemical reaction, or a non-electrochemical/physical degradation of the oxide films that result in a mass loss from the disk without allowing detection at the ring electrode. Additional results via scanning electrochemical microscopy (SECM) will be shown at chapter 5 in order to corroborate this observation and to develop a mechanistic model to describe the mass loss based on these results.

3.3.4 Electrochemical Pt surface shielding by cation (Zn^{2+}) UPD

As mentioned in chapter 3.3.1, cycling with a lower potential limit in the range of the hydrogen underpotential region appears to lower the cyclic dissolution rate significantly below that which results when the lower limit is maintained in the oxide and H UPD free region. In the absence of any information about a specific interaction between platinum and the electrolyte under these conditions, we surmised

that the hydrogen underpotential deposition process somehow influenced the nature of the platinum surface and how it would behave subsequently. We noted in the introduction that Zn UPD changes the nature of the H UPD region by surface reordering or blocking in this potential region (55-56); while we do not anticipate that cations such as Zn^{2+} will likely be present in significant quantities in fuel cell operation, we considered that the opportunity to interfere with hydrogen underpotential deposition (UPD) or to electrochemically shield the Pt surface by competition between Zn underpotential deposition (UPD) and Pt ion redeposition that might be generated during PtO_2 reduction process while still sweeping to the same potentials might help to illuminate the role that this process plays on electrode degradation. In these experiments, we used underpotential deposition (UPD) of Zn^{2+} on Pt catalyst in 0.5 M H_2SO_4 to probe the influence of the hydrogen underpotential region on overall dissolution rate.

Underpotential deposition (UPD) gives a surface ad-layer of less than a monolayer of a metal on a foreign metal surface, and has been studied for electrochemical process such as electroplating, electrocatalysis, electrocrystallization, etc (59-61). The Zn UPD was first reported on Pt by Takamura et al. (62) as an adsorption phenomenon in 1970. The UPD shift potentials, ΔE_{UPD}, were observed as ca. 1.1 V for Pt and Pd, and ca. 0.6 V for Au, being expressed as $e\Delta E_{UPD} \approx \phi_s - \phi_{Zn}$ (63). Where e is the elementary charge, ϕ_s and ϕ_{Zn} is the work functions of substrate and Zn, respectively. The standard reduction potential of

Zn^{2+}/Zn is -0.76 V_{RHE}, the UPD of Zn^{2+} ions on Pt surface is around +0.34 V_{RHE}; this 1.1 V potential shift of Zn UPD from standard reduction potential is the work function difference between Pt and Zn (63-64). For 5mM $ZnSO_4$, these UPD properties are, of course, strongly influenced by the surface structure characterization of electrochemically oriented Pt electrode, and the influence of the reordering Pt surface by electrochemically shielding of Pt ion redeposition is due to the formation of new surface structure which may have adsorption-desorption properties that differ from both Pt and Zn metals (55).

Figure 3.8 shows a cyclic voltammogram and the resulting EQCN mass change of the electrode versus electrode potentials in 0.5 M H_2SO_4, for a scan rate of 100 mVs^{-1} both with and without the addition of 5 mM $ZnSO_4$ to the electrolyte. At potential lower than 0.4 V_{RHE} without Zn ion additives, the mass of the electrode decrease with cycling into the H UPD region, relative to the mass in the capacitive region of the CV. It is worth noting that the addition of Zn ion to the 0.5 M H_2SO_4 acid solution does not appear to affect the processes in double layer region or the oxide formation/reduction on the Pt surface.

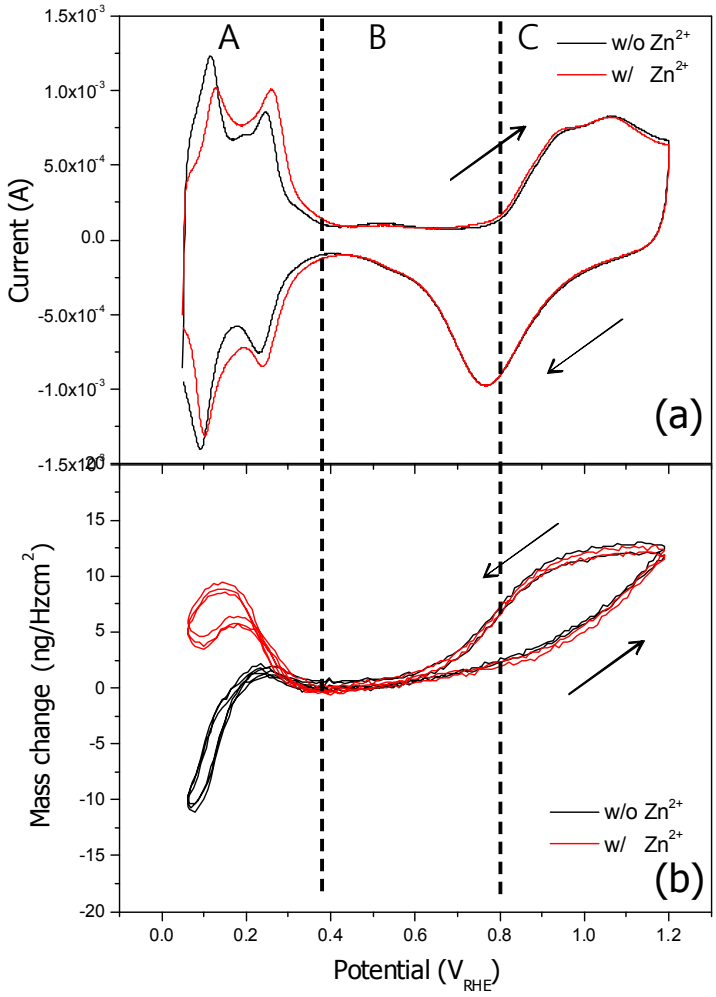

Figure 3.8 (a) Cyclic voltammogram and (b) EQCN mass change measured simultaneously in 0.5 M H_2SO_4 with and without 5 mM $ZnSO_4$. Scan rate is 100 mVs^{-1}.

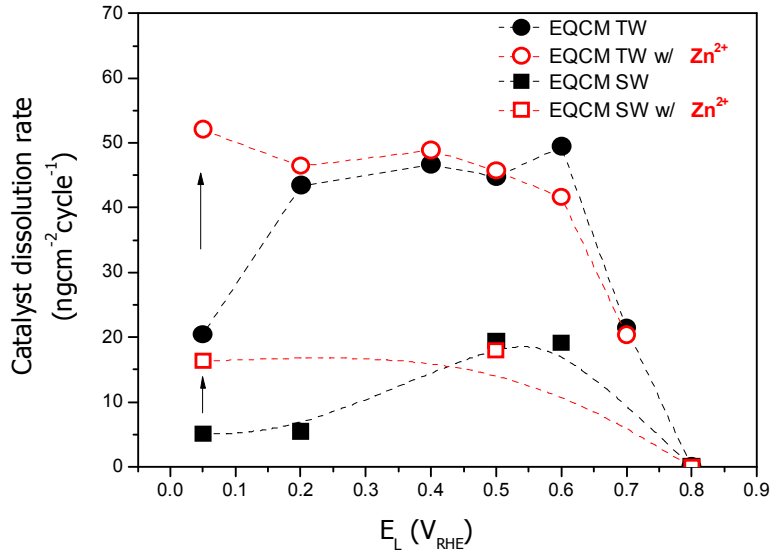

Figure 3.9 Pt dissolution rate as a function of E_L with E_H =1.6 V_{RHE} at 298 K in 0.5 M H_2SO_4 for 500 mVs^{-1} triangular wave (TW) and 1Hz square-wave (SW) over 500 cycles, with and without Zn ion additives.

Figure 3.9 shows the Pt dissolution rate of triangular-wave and square-wave cycling both with and without Zn ion additives. Compared to Figure 3.3, in the presence of Zn^{2+}, the dissolution rate at E_L = 0.05 V_{RHE} increases to a rate roughly the same as the dissolution rate observed when the lower potential limit is maintained above the H UPD range for both triangular-wave and square-wave experiments. EQCN measurements from cycling experiments (E_L = 0.05 V_{RHE} with E_H = 1.6 V_{RHE}) are qualitatively consistent with the results of ICP analysis (28.96 $ngcycle^{-1}cm^{-2}$ without Zn additive, versus 62.43 $ngcycle^{-1}cm^{-2}$ with Zn additive). So, the nature of what happens in the UPD region (region A in Figure 3.8) is presumed to have a

strong influence on Pt dissolution in cycling experiments for various lower potential limits when the upper limit is held fixed at 1.6 V_{RHE}, even though the amount of dissolution observed when the electrode is held without cycling in this potential window has been shown by others to be very low (29).

In addition, we conducted a series of experiments on the Pt dissolution rate by changing the kind of cation in the electrolyte in the acid solution, otherwise conducted at the same conditions as described above. The results are shown in Figure 3.10. The addition of alkaline metal ions such as Li_2SO_4, Na_2SO_4, K_2SO_4 that have more negative UPD potentials than H UPD have no noticeable effects on the Pt dissolution rate or ECSA loss compared to the sample with no additives.

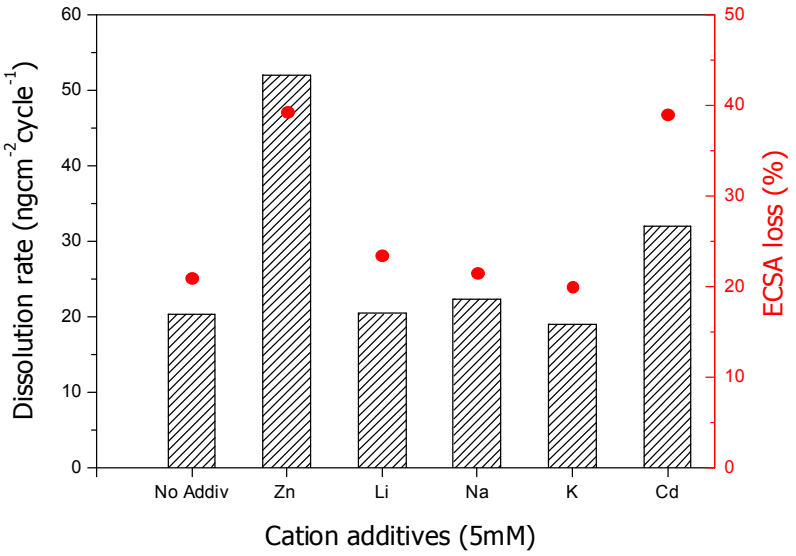

Figure 3.10 Pt dissolution rate (bar) and ECSA loss (dot) at E_L = 0.05 & E_H = 1.6 V_{RHE} with various cation additives. The mass loss is shown as loss per cycle; the ECSA loss is cumulative over the course of 500 cycles.

This means that these ions present in the outer Helmholtz plane do not appear to influence Pt surface adsorption/desorption. On the other hand, the addition of $CdSO_4$ that has UPD at around 0.71 V_{RHE} (65) (within the H_2O adsorption/desorption region) results in an increased Pt dissolution rate and ECSA loss, though not as much as of $ZnSO_4$.

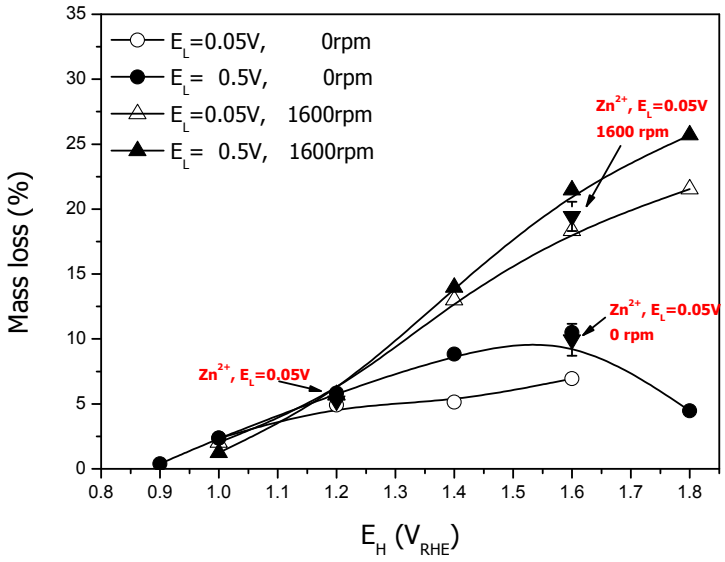

Figure 3.11 ICP-MS results of RRDE test at 298 K in N_2 saturated 0.5 M H_2SO_4 for 500cycle of 500 mVs^{-1}, scan rate in terms of potential limits (E_L, E_H) and rotation speed.

We investigated the influence of Zn additives further in a series of experiments shown in Figure 3.11. This Figure shows Pt catalyst dissolution resulting from potential cycling for several different sets of conditions. For curves indicated by

unfilled markers, the solution is free of Zn additives, and the lower potential limit is maintained at 0.05 V_{RHE}, well within both the H UPD and Zn UPD potential range; for the set of curves with filled triangles oriented upwards, the solution is free of Zn additives and the lower potential limit is maintained at 0.5 V_{RHE}, well above the UPD regions. All experiments were conducted at 500 mVs^{-1}, with two different rotation speeds: stagnant conditions (no rotation= circular markers), and with a rotation speed of 1600 rpm (triangular markers). Data for solutions with Zn added to the acid solution are shown for a handful of cases by points highlighted by arrows on the graph and indicated by filled, downward-pointing triangular markers.

We consider the influence of Zn additives in three distinct conditions: E_H = 1.2 V_{RHE}, E_H = 1.6 V_{RHE} under stagnant conditions, and E_H = 1.6 V_{RHE} at a rotation speed of 1600 rpm. We see that the Pt catalyst mass loss increases with increasing rotating speed when the upper potential limit is set above 1.2 V_{RHE}, while we see less separation as a function of rotation speed when the upper potential limit is set below 1.2 V_{RHE}. Moreover, the influence of Zn additives on Pt dissolution is smaller at less positive upper potential limits, as can be seen by the data points plotted at E_H = 1.2 V_{RHE}. Furthermore, in cases with high rotation speeds, the addition of Zn to the acid solution does not enhance the dissolution rate for E_L = 0.05 V_{RHE} nearly as much as it does under stagnant conditions, or with the comparatively low flow rates of the EQCN flow cell as shown in Figure 3.9.

While hardly conclusive, these data are consistent with a scenario in which the hydrogen underpotential region prepares the platinum surface to be more conducive

to redeposition or recapture of the mobile species when mobile species are generated during cycling. The fact that rotation speed increases the overall rate of dissolution at higher potentials suggests that convection can carry mobile species away from the surface before they can redeposit. If the effect of Zn was invariant with rotation speed, we might infer that the Zn interference with hydrogen underpotential deposition changed the magnitude or nature of dissolution; the fact that the system is more sensitive to Zn additives under stagnant conditions than under conditions of higher rotation speeds suggests changes in solution-phase saturation or redeposition rates relative to convection. We note that the relatively small changes to the rate of mass loss with Zn additives at potentials where PtO_2 has yet to be formed makes it more likely that the UPD region has a greater effect on the reaction in Equation 3.6 than passivation or protection from Equation 3.1, though both mechanisms do appear to be at play in the system. So, these results shown above represent that Zn UPD changed the properties of the Pt surface where the potential is less than 0.34 V_{RHE} or hinder soluble Pt species from re-depositing on Pt surface. While the exact mechanism of what occurs on the surface at lower potential and its effect on oxide formation and stripping is not yet clearly understood, the competition of Zn UPD (adsorption) with Pt^{2+} redeposition might develop Pt-Zn-Pt structure if we assume Pt^{2+} is generated during PtO_2 reduction process (Equation 3.6) and accelerate Pt dissolution by losing Pt on top of Zn when the adsorbed Zn desorbs during anodic scan in the potential cycling process.

From the discussion above it is clear that the influence of Zn UPD and the hydrogen underpotential deposition processes are not sufficiently explored in the literature, especially the relationship between UPD and Pt dissolution. Moreover, there is little data about the surface structure of the monolayer with regard to the number of active sites occupied by each ad-atom, as well as to the maximum coverage of the surface. To the best of the authors' knowledge, this study of the incorporation of Zn UPD in explaining the Pt dissolution rate is novel and has not been reported before. While we do not anticipate that cations will be used to tailor stability in actual fuel cell operation, we believe that the results suggest future work to clarify how modifications to the surface in the H UPD region are sustained even as the metal is cycled to higher potentials.

3.4 CONCLUSION

The dissolution behavior of Pt catalyst was investigated by EQCN flow cell, RRDE and ICP-MS. We found that when the upper potential limit was maintained at 1.6 V_{RHE}, the dissolution rate from both triangular-wave and square-wave potential cycling revealed a broad maximum as a function of the lower potential cycling limit; cyclic tests in which the lower potential limit remained either entirely within a region of oxide stability or in a region where H UPD occurs resulted in significantly lower dissolution rate. The results from the EQCN experiment are quite compatible with the results obtained by ICP-MS. We also found a significant effect of metal UPD on dissolution from cycling under conditions in which the lower potential limit was less

than 0.2 V_{RHE}. By adding 5mM of Zn^{2+} ion, the Pt dissolution rate under conditions when E_L was less than 0.2 V_{RHE} increased up to the same relatively largely rates when E_L was set to 0.5 - 0.6 V_{RHE}. These results suggest that Zn UPD changed the properties of the Pt surface that influence dissolution by hindering soluble Pt species from re-depositing on Pt surface, but the nature of what occurs on the surface at lower potential and its effect on oxide formation and stripping is not yet understood. From the RRDE test, the rotation speed plays a key role in accelerating Pt dissolution over E_H = 1.2 V_{RHE}. The soluble Pt species can be detected at the ring electrode (E_{ring} = 1.4 V_{RHE}) during cathodic scans of disk electrode at potentials more positive than E_H = 1.3 V_{RHE}.

The amount of Pt^{2+} detected at ring electrode during cathodic scan is estimated to be about 4.99 % of total dissolved Pt amount during cycling, suggesting formation of other electrochemical active mobile species or detached species not detectable electrochemically.

CHAPTER 4

Influence of ORR on Pt oxide formation and Pt dissolution

4.1 INTRODUCTION

A major contributor to the deterioration of the fuel cell's performance over time is the decrease of oxygen reduction reaction (ORR) activity, both from oxide poisoning (so-called daily decay), and by electrochemical surface area loss, which has can be accelerated by potential cycling (4).

The oxygen reduction reaction (ORR) occurs in a potential range where the platinum surface is at least partially covered by oxides. These Pt oxides can be formed from both H_2O (30, 45, 47) and gas-phase O_2 (66). While it has been reported that the Pt oxide formed from H_2O decreases the oxygen reduction activity by acting as poison (67-69), it is as yet unclear how Pt oxide formed from gas phase O_2 influences either the composition of the surface or the oxide's role in partially protecting the surface from dissolution.

Recently, Paik *et al*. (70) reported on the influence of gas phase O_2 on Pt oxide formation. They found that O_2 reduction generates more Pt oxide formation by direct dissociative adsorption of O_2 on Pt at 0.85 V_{RHE}, but does not do so at 0.95 V_{RHE}. However, this work did not examine potential holds above 0.95 V_{RHE}. By contrast, Liu *et al*. (71) reported that the amount of Pt oxide does not depend on previous exposure to gas-phase O_2, indicating the reversibility of any oxidized species generated in the presence of gas phase O_2. Most recently, Sugawara *et al*. (72)

showed that oxygen concentration affects electrochemical oxidation of Pt surface by using RRDE, and Matsumoto *et al*. (73) also showed the electrochemical dissolution of Pt is enhanced under potential cycling in an oxygen atmosphere.

In the proton-exchange membrane fuel cell stack test, Bi *et al*. (74) showed that oxygen environment, compared to nitrogen, appeared to be have a negligible effect on Pt/C degradation in PEMFC under potential cycling up to 1.2 V_{RHE}.

In this study, we showed the effect that oxygen has very close relation with Pt oxide formation/reduction for wide range of potentials by using various electrochemical techniques and also investigated the degree to which Pt dissolution by the nature of Pt oxide formation/reduction is related to the oxygen reduction reaction (ORR) by using ICP-MS analysis.

4.2 EXPERIMENTAL

A catalyst layer was fabricated on a glassy carbon working electrode by dispersing 30 mg of Pt-black catalyst (E-Tek) and 180 mg of 5 wt% Nafion solution (Aldrich) in the mixture of 2 mL of isopropyl alcohol and 4.5 mL of distilled pure water. The solution was ultrasonicated until a dark homogeneous dispersion was formed during about 1hr; 8 μl of the dispersed ink solution was dropped onto the glassy carbon (GC) disk electrode of rotating disk electrode (RDE, Pine Inc.) or rotating ring disk electrode (RRDE, Pine Inc.) to give an catalyst loading of 35,800

ng. The loading was 188.5 ugcm^{-2} for RDE, 144.6 ugcm^{-2} for RRDE and the electrodes were subsequently dried in the atmosphere of ultra pure N_2 gas (99.999%).

100 ml of 0.5 M H_2SO_4 electrolyte solution was de-aerated or aerated with vigorous bubbling with very high purity N_2, air or O_2 gas for 1hr before each electrochemical test; continuous purging was maintained during the experiment. Prior to the measurements, the working electrode was pretreated by a potential cycle (CHI760C, CH Instruments Inc.) between 0.05 ~ 1.0 V_{RHE} at a rate of 100 mVs^{-1} for 20 cycles. The hydrogen electrode (HydroFlex, Gaskatel GmbH Inc.) and Pt wire electrode separated by glass frit were also used as reference and counter electrode.

Linear sweep voltammograms (LSVs) were carried out to examine the effect of oxygen exposure on oxide stripping. For N_2 experiments, the working electrode was held at a defined potential for 50 min under N_2 condition; to determine the effect of oxygen exposure without requiring the subtraction of an ORR background current, the electrode was held at a defined potential for 40min while being exposed to O_2, followed by a 10-minute hold at the same potential with vigorous nitrogen bubbling through the solution. After holding each electrode at fixed potential under either N_2 or O_2/N_2 conditions, LSVs were obtained by cathodically sweeping from the holding potential to 0.05 V_{RHE} at 50mVs^{-1}.

Simultaneous Pt oxide formation/reduction measurements in the presence of oxygen or air were carried out by square wave voltammetry (SWV) method by RDE and oxygen reduction reaction (ORR) shielding effect method at high convection condition by RRDE (GC disk – Pt ring, E7R9, PINE Inc.). The SWV was carried out

with the parameters of 25 mV amplitude, 5mV step height, 5Hz frequency and the shielding effect method was carried out by 50mV/s scan rate of cyclic voltammetry from 0.05 V_{RHE} to 1.2 V_{RHE} under each N_2, air, O_2 convection condition (1600rpm).

Accelerated degradation tests (ADT) via potential cycling (0.5 V_{RHE} to various upper potential limits E_H) were carried out on a rotating disk electrode at 1600 rpm condition. At the end of testing, the solutions were analyzed by using ICP-MS (Optimass 8000, GBC Scientific Inc.) to determine the amount of dissolved Pt ion; the ICP-MS system had a detection limit of 0.1 ngL^{-1} for Pt ions.

The generation of mobile platinum species during Pt oxide reduction was investigated at N_2, O_2 condition using a rotating ring disk electrode. A Pt catalyst loaded on GC disk – Au ring electrode (E7R9, PINE Inc.) was CV scanned with 50mVs^{-1} scan rate between 0.05 V_{RHE} ~ 1.6 V_{RHE} at 1.4 V_{RHE} of ring potential.

4.3 RESULTS AND DISCUSSION

4.3.1 Influence of ORR on Pt oxide formation at potential holding condition

Figure 4.1 (a) shows the LSVs collected after holding at various potentials after exposure to either N_2 alone or exposure to O_2 followed by N_2 purging. As shown in earlier studies(70) and mentioned in the introduction, the amount of Pt oxide present on the surface after a fixed potential hold increases with previous exposure to O_2 below 0.95 $V_{RHE.}$ Above 0.95 $V_{RHE,}$ we find that total oxide present after a hold at a fixed potential is lower after previous exposure to O_2 than after exposure to N_2 alone.

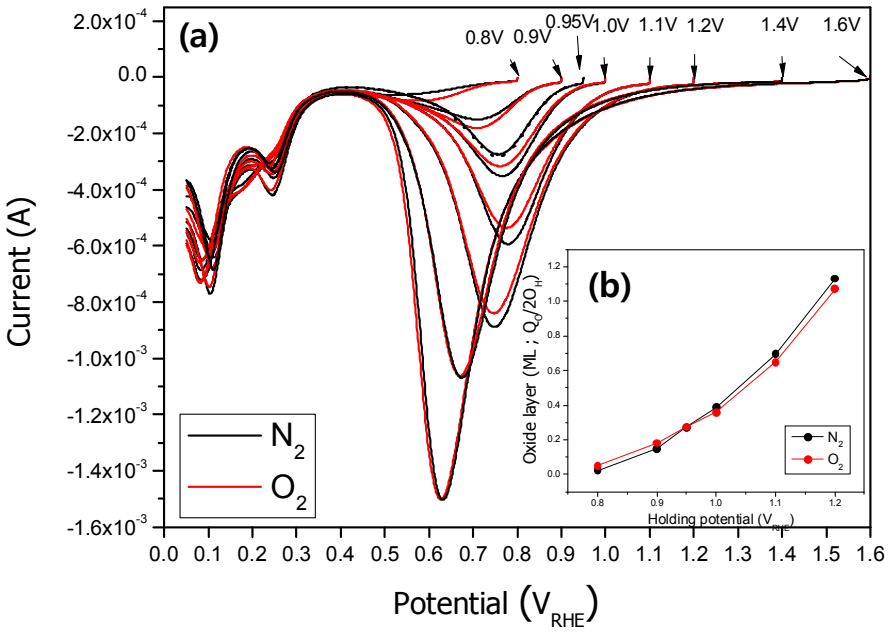

Figure 4.1 (a) LSVs (linear sweep voltammograms) following initial potential hold after exposure to N_2 (50min) and O_2 (40min) / N_2 (10min) at each potential.

(b) Oxide layer (ML) normalized by ECSA at each holding potential under N_2, O_2 condition.

It is interesting to note that O_2-exposed and N_2-exposed curves lie almost directly on top of one another at 0.95 V_{RHE} and above 1.4 V_{RHE}; at lower potentials of 0.95 V_{RHE}, the oxygen-rich solution appears to promote more oxide formation, while at higher potentials up to 1.2 V_{RHE}, Platinum oxide formation appears to be hindered in the presence of oxygen by ORR and above 1.4 V_{RHE}, the presence of oxygen plays no role on platinum oxide formation because this region is beyond oxygen reduction

reaction (ORR). Figure 4.1 (b) represents the oxide layer (ML) normalized by electrochemical surface area (ECSA) at each holding potential under N_2, O_2 condition.

The result that Pt oxide coverage depends on the ORR can be explained by that Pt oxides (PtO or PtOH) are intermediate states during ORR that seems like to act as Pt oxide formation contributor at below 0.95 V_{RHE} and as competitor or consumer at above 0.95 V_{RHE}. Note that this trend was reproduced regardless of various kind of Pt electrodes such as Pt UME (ultramicroelectrode, 100um diameter) or Pt smooth planar electrode (2mm diameter) and even experimental order of O_2 or N_2 exposure condition.

In regards to this discrepancy of ORR influence on Pt oxide formation at below and above 0.95 V_{RHE}, we can take a consideration in terms of several points of view.

The first one is from the view of intermediate states (i.e. PtO, PtOH) during oxygen reduction reaction (ORR), the ORR mechanism was investigated by theoretical calculation based periodic density function theory calculation in terms of free energy of intermediates for both the 'dissociative' and 'associative' reaction pathway (66, 75). The dissociative mechanism is

$$\frac{1}{2}O_2 \rightarrow O_{ad} \tag{4.1}$$

$$O_{ad} + H^+ + e^- \rightarrow HO_{ad} \tag{4.2}$$

$$HO_{ad} + H^+ + e^- \rightarrow H_2O \tag{4.3}$$

And the associative mechanism is

$$O_2 \rightarrow O_{2ad} \tag{4.4}$$

$$O_{2ad} + H^+ + e^- \rightarrow HO_{2ad} \tag{4.5}$$

$$HO_{2ad} + H^+ + e^- \rightarrow H_2O + O_{ad} \tag{4.6}$$

$$O_{ad} + H^+ + e^- \rightarrow HO_{ad} \tag{4.7}$$

$$HO_{ad} + H^+ + e^- \rightarrow H_2O \tag{4.8}$$

Where *ad* denotes the adsorption on the Pt surface (i.e. O_{ad}, OH_{ad}). Although these two mechanisms differ each other in terms of their pathway, there are generation and extinction steps of PtO, PtOH as intermediate states during reaction.

The last one is from the view of intermediate states (i.e. PtO, PtOH) during electrochemical oxidation of H_2O on Pt surface that was reported by Conway *et al.* (42), and Harrington (47).

$$Pt + H_2O \rightarrow PtOH + H^+ + e^- \tag{4.9}$$

$$PtOH \rightarrow PtO + H^+ + e^- \tag{4.10}$$

$$Pt + H_2O \rightarrow PtO + 2H^+ + 2e^- \tag{4.11}$$

However, in regards of kinetics of Pt oxidation from water, Harrington showed that PtO forms slowly and then rapidly diffuses across the Pt surface, whereas Conway et al. proposed a rapid formation of PtOH followed by a slow place exchange between Pt and OH. The place exchange between Pt and OH was modified

as place exchange between Pt and O, not OH by Jerkiewicz *et al*. (30) by using electro quartz microbalance (EQCM).

The products of Equation 4.1~4.7 are intermediates for oxygen reduction mechanism which means that the formation of PtO, PtOH is necessary for oxygen reduction. However, if Pt oxide cannot be quickly reduced to Pt, it will block oxygen access to the Pt surface. With regards to the comparison of kinetics of generation and extinction of Pt oxide from ORR and electrochemical oxidation from H_2O, there is no literature result. However, from the results of this study, we can conclude that there is an interaction between ORR and electrochemical Pt oxidation and shows different effects at above and below 0.95 V_{RHE}.

The third one is place exchange phenomenon between Pt and O above place exchange onset potential.

Jerkiewicz *et al*. (30) proposed the mechanism of place exchange between Pt and O by showing Pt surface oxidation. They proposed the first step involves interaction of H_2O molecules with Pt below 0.85 V_{RHE} by partial positive charge of Pt surface that attracts the negatively charged oxygen end of the water molecules (Equation 4.12).

$$Pt + H_2O \xrightarrow{strong\ physisorption} Pt^{\delta+} - O^{\delta-}H_2 \qquad (4.12)$$

Above 0.85 V_{RHE}, the discharge of about half a monolayer of H_2O molecules takes place and results in formation of about 0.5 ML of chemisorbed oxygen (O_{chem}) (Equation 4.13).

$$(Pt+Pt)-H_2O \rightarrow (Pt+Pt)^{\delta+}-O^{\delta-}H_{chem}+H^+ + e^- \quad (4.13)$$

$$(Pt+Pt)^{\delta+}-O^{\delta-}H_{chem} \rightarrow (Pt+Pt)^{\delta+}-O^{\delta-}+H^+ + e^- \quad (4.14)$$

And then, the second 0.5 ML of H_2O molecules is formed by discharging process (Equation 4.14)

$$Pt-O_{chem}+H_2O \rightarrow Pt^{2+}-O^{2-}+2H^+ + 2e^- \quad (4.15)$$

During the process of Equation 4.15, the second half monolayer of O_{chem} begins to build up and strong dipole-dipole lateral repulsive interactions set in themselves, driven by the dipole moment of the $(Pt-Pt)^{\delta+}-O_{chem}{}^{\delta-}$. And then, the initial 0.5 ML of O_{chem} adatoms undergo an interfacial place exchange process with the Pt surface atoms leading to a 3-dimensional PtO lattice in order to minimize repulsions between O_{chem}.

$$PtO \rightarrow OPt \quad (4.15)$$

However, the onset potential of this place exchange is still a matter of debate. Angerstein-Kozlowska *et al*. (76) proposed that place exchange begins above 0.95 V_{RHE} by revealing little displacement of the reductive peak to lower potentials relative to the oxidative peak until the upper limit exceeded 0.95 V_{RHE}.

Wagner and Ross (77) suggested that place exchange begins at around 1.0 V_{RHE}. Assuming the onset potential of place exchange is around 0.95 V_{RHE}, the change in relative oxide prevalence with and without oxygen exposure in acid solutions suggests a close relationship to the place-exchange mechanism and overall oxide thickness.

Alsabet *et al*. (78) proposed the growth of PtO follows two distinct kinetic laws i) the logarithmic growth of PtO at below 1.0 V_{RHE}, ii) inverse-logarithmic growth law at above 1.0 V_{RHE}. He also proposed that logarithmic growth law originates from the interfacial exchange between O_{chem} and the top-most Pt which means at the surface of Pt, whereas the inverse-logarithmic growth law comes from the inner Pt/oxide interface which means place exchange.

Most recently, Friebel *et al*. (79) showed that in 0.01M $HClO_4$, a place exchange begins to take place from 1.0 V_{RHE} by using *in situ* X-ray absorption spectroscopy (XAS) and proposed that the potential for oxide formation be expected to be kinetically influenced by the stability of its precursor state, *i.e.* chemisorbed oxygen on the Pt surface. Moreover, Imai *et al*. (80) proposed that by using *in situ* time-resolved energy dispersive X-ray Absorption Spectroscopy (DXAFS), the successive process for oxygen chemisorptions seems to be formation of the PtO_2, the nature of the PtO_2 is very different from that of bulk oxides consisting of Pt^{4+} (or Pt^{2+}) and O^{2-}. From these previous works, the place exchange can be thought to start around 0.95 V_{RHE} ~ 1.0 V_{RHE} and the results of this study that the oxygen reduction reaction (ORR) plays a significant role on Pt oxide formation by either contributing or competing to it around 0.95 V_{RHE} ~ 1.0 V_{RHE} can be thought reasonable.

From the point of views such as ORR mechanism, Pt oxidation mechanism via electrochemical reaction of H_2O and place exchange between Pt and O, we can conclude that ORR and electrochemical Pt oxidation from water has strong relation with respect to the kinetics of generation and extinction of Pt oxide.

4.3.2 Simultaneous measurement of Pt oxide formation under ORR condition.

4.3.2.1 Measurement by square wave voltammetry method

The Pt oxide coverage is typically measured by integration of oxide formation or reduction charge passed during cyclic voltammetry (CV) or linear sweep voltammetry (LSV) such as Figure 4.1 (b). Because these measurements are conducted under N_2 saturated (i.e., deaerated) conditions, it is impossible to measure both the Pt oxide formation/reduction and the oxygen reduction reaction (ORR) activity at the same time; moreover, the relationship between the two is obscured. So-called gas switching ($O_2 \rightarrow N_2$) experiment such as Figure 4.1 may be unable to estimate actual Pt formation/reduction while the ORR proceeds because oxygen is absent during the Pt oxide formation or reduction measurement. Therefore, in this study, we propose a set of experiments to study the formation and stripping of Pt oxide in the presence of ORR.

We studied the methods of simultaneous electrochemical measurement of the Pt oxide formation/reduction in the presence of ORR and clarified their relationship by i) square wave voltammetry (SWV) and ii) shielding effect method using RRDE. Figure 4.2 (a) and (b) shows schematic waveform of potential and its current response throughout an SWV experiment for reversible oxidation/reduction materials with R absent from the bulk. SWV is a further improvement of staircase voltammetry which is a derivative of linear sweep voltammetry. In SWV, a square wave is superimposed on the potential staircase sweep. Current samples are taken twice per cycle at the end of each pulse. The forward current sample (i_{for}) arises from the first pulse per cycle,

which is in the direction of the staircase scan. The reverse current sample (i_{rev}) is taken at the end of the second pulse, which is in the opposite direction. Net current (i_{net}) is represented as the difference between i_{for} and i_{rev}.

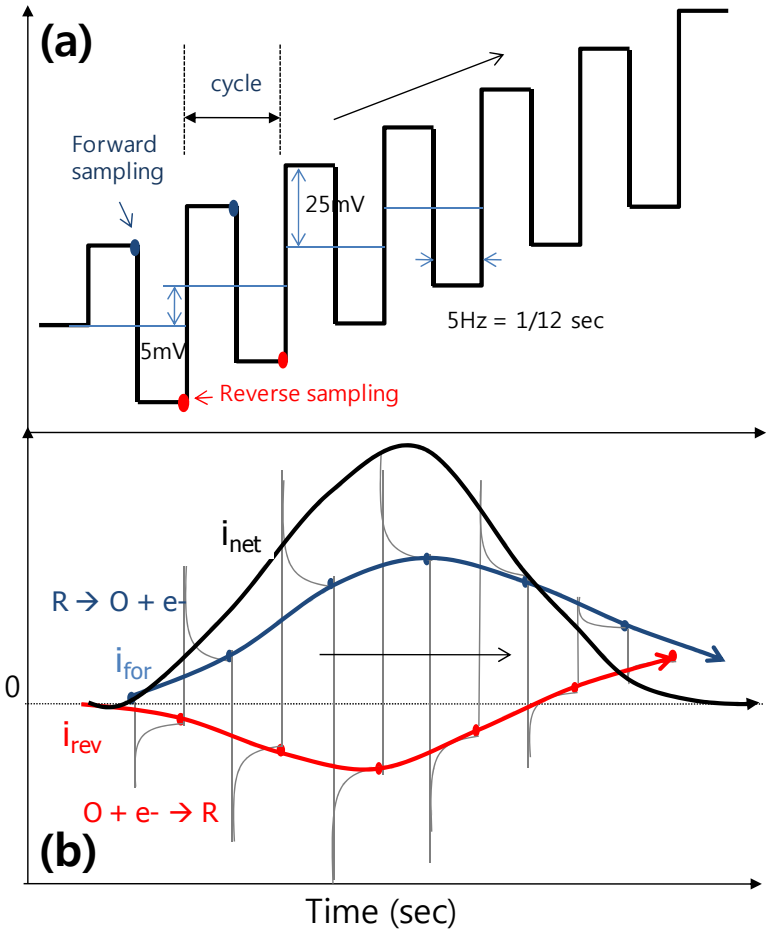

Figure 4.2 (a) Schematic of potential pulse of square wave voltammetry (SWV)
(b) Schematic of current responses of potential pulse

On the whole, SWV is much better than CV for evaluating quantitative output current signal for systems and especially is the best choice for cancelling out the background currents, such as contributions from H_2O double-layer capacitance or the oxygen reduction reaction (ORR). by obtaining the difference between the forward current and reverse current. Therefore, SWV experiment is appropriate method for evaluating the degree of Pt oxidation formation reaction under ORR active condition. Moreover, due to the lesser contribution of capacitance charge and other background charge (i.e., ORR), the detection limit for SWV is on the order of nanomolar concentrations. In this study, the square wave experiment is characterized by frequency (5 Hz), potential amplitude (25 mV) and potential step (5 mV).

Figure 4.3 (a : anodic scan, b : cathodic scan) shows the forward current (i_{for}) and the reverse current (i_{rev}) at N_2, air, O_2 saturated 0.5M H_2SO_4 acid solution under 1600 rpm rotation rate condition. From the Figure 4.3 (a) N_2 condition, the hydrogen adsorption/desorption current peaks are shown at the same anodic scan. Moreover Pt oxide formation current (i_{for}) start to increase anodically from around 0.7 V_{RHE} and Pt oxide reduction current (i_{rev}) also start to increase cathodically because Pt oxide was formed at each previous forward pulse scan. In Figure 4.3 (a, b) air and O_2 condition, the current at H_2O double layer capacitance potential region (0.4 V_{RHE} ~ 0.7 V_{RHE}) is located at less positive potential than N_2 condition due to the oxygen reduction reaction (ORR) under condition with high rates of mass transport.

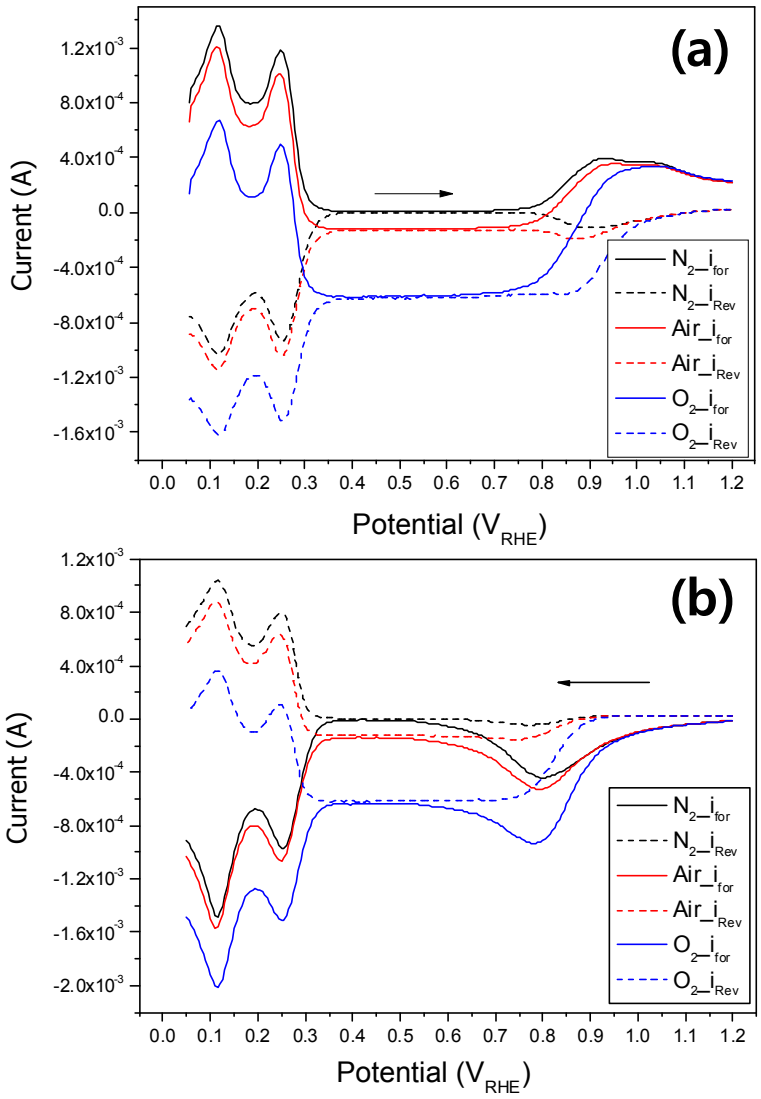

Figure 4.3 (a) Comparison of forward current (solid line) and reverse current (dashed line) of anodic direction scan SWV at N_2 (black), air (red), O_2 (blue) saturated 0.5 M H_2SO_4 solution.

(b) Comparison of forward current (solid line) and reverse current (dashed line) of cathodic direction scan SWV at N_2 (black), air (red), O_2 (blue) saturated 0.5 M H_2SO_4 solution

Figure 4.4 (a, b) reveals the net current of Figure 4.3 (a, b). Neither graph reveal a background current due to double-layer capacitance or ORR, due to cancellation of each on forward and reverse current. By eliminating the ORR current, there remain only Pt oxide formation/reduction reaction peaks around 0.6 V_{RHE} ~ 1.2 V_{RHE}. In this way, we can compare Pt oxide formation/reduction in the presence of air or O_2. From inset of Figure 4.4 (a), we can see that the onset potential of Pt oxide formation of O_2 condition is more negatively located than air and N_2 condition and Pt oxide formation is also accelerated at below 1.0 V_{RHE}. These results look compatible with previous results in the literature proposing that Pt oxide formation changes via place exchange starting around 0.95 V_{RHE} ~ 1.0 V_{RHE} as well as the result of Figure 4.1 that shows oxygen reduction reaction (ORR) plays a role on Pt oxide formation.

4.3.2.2 Measurement by shielding effect method of RRDE

The second method for simultaneous electrochemical measurement of the Pt oxide formation/reduction in the presence of ORR is the shielding effect technique of RRDE. If there is only oxygen reduction reaction ($O_2 + 4H^+ + 4e^- \rightarrow 2H_2O$) at Pt ring electrode in the acid solution, the ORR current at the ring electrode is strongly influenced by oxygen flux from disk electrode (oxygen shielding effect) which is given by (42).

$$i_{Ring} = nFD_{O_2} 2\pi \int_{r_2}^{r_3} \left(\frac{\partial C_{O_2}}{\partial y}\right)_{surface(y=0)} r dr \qquad (4.16)$$

Where r_2 and r_3 are the inner radius and outer radius of ring electrode, respectively (r_2 = 3.13mm, r_3 = 3.96mm in this study).

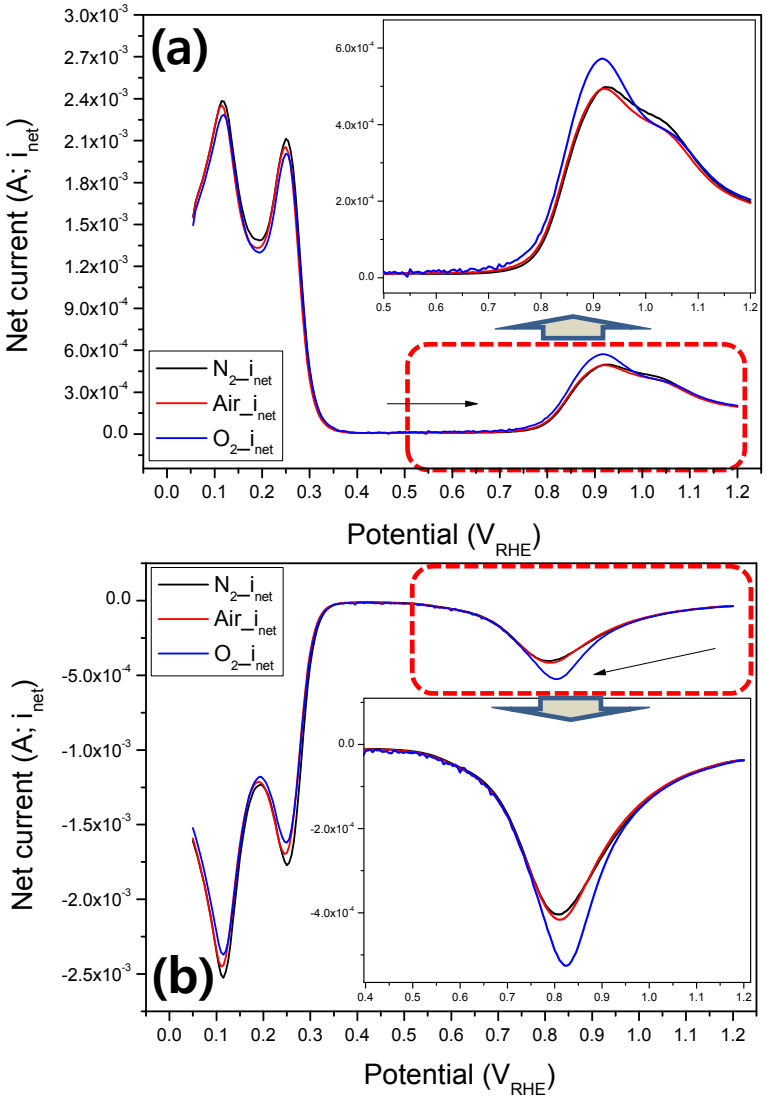

Figure 4.4 (a) Net current (i_{net}) of anodic direction scan SWV at N_2 (black), air (red), O_2 (blue) saturated 0.5 M H_2SO_4 solution.

(b) Net current (i_{net}) of anodic direction scan SWV at N_2 (black), air (red), O_2 (blue) saturated 0.5 M H_2SO_4 solution.

Figure 4.5 shows a rapid current variation of disk and ring electrode when the vigorous N_2 bubbling was stopped during RRDE measurement under convection condition in the 0.5 M H_2SO_4. We can see the disk and ring current shifts more negatively as the measurement time goes on right after vigorous N_2 bubbling was stopped because oxygen concentration increase. And the oxide covered potential region (> 0.8 V_{RHE}) on the disk electrode is less effective at reducing oxygen in solution than the bare Pt region (< 0.8 V_{RHE}); at cathodic potential, the ring electrode reveals a little other than two distinct limiting current plateaus, based upon how much oxygen is consumed at the disk electrode.

The limiting ring current and collection efficiency (N) can be written as shown in Equation 4.17 and 4.18.

$$i_{Ring,\lim} = 0.62nF\pi(r_3^3 - r_2^3)^{2/3} D_{O_2}{}^{2/3} \omega^{1/2} \upsilon^{-1/6} C_{O_2}^* \tag{4.17}$$

$$N = \frac{-i_{Ring}}{i_{Disk}} \tag{4.18}$$

Where ω is rotating rate (s^{-1}), υ is kinematic viscosity (cm^2s^{-1}) and i_{Disk} is current at disk electrode. The collection efficiency (N) depends only geometrical dimension of disk and ring electrode and is independent of ω, oxygen concentration, oxygen diffusion coefficient.

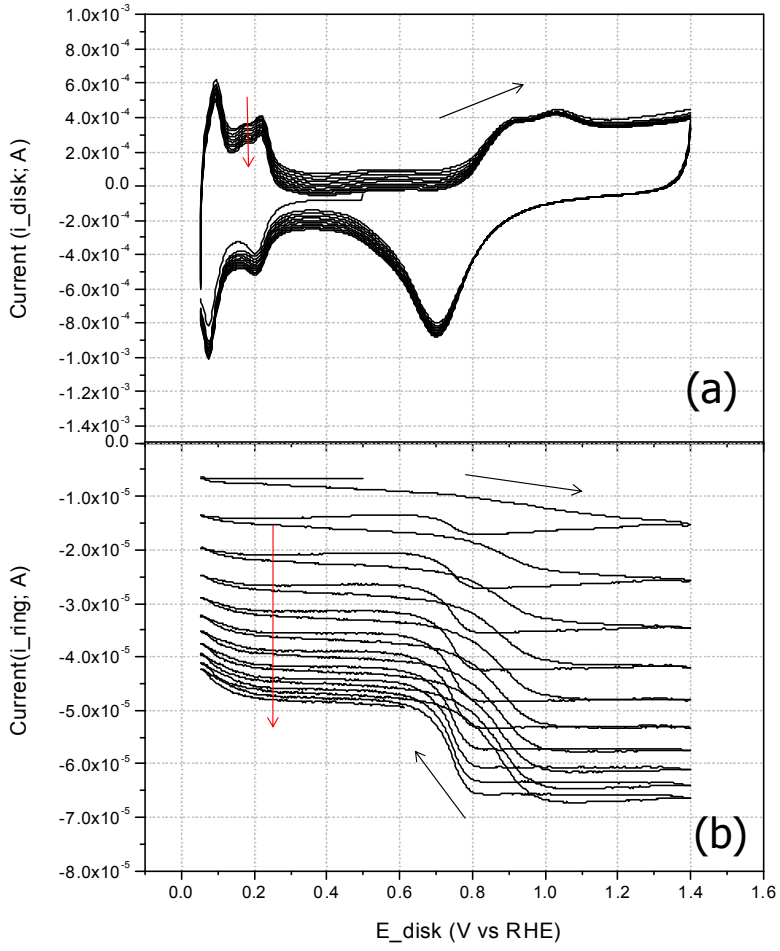

Figure 4.5 Oxygen shielding effect of RRDE experiment. (vigorous N_2 bubbling was stopped right after measurement, rotating speed :1600 rpm)

(a) Measured current at disk electrode (Pt black coated film on GC electrode, scan rate 50 mVs^{-1})

(b) Measured Pt ring current (E_{ring} = 0.5 V_{RHE})

The limiting current at the ring will achieve its maximum current ($i_{Ring,\lim}^{i_{Disk,ORR}=0}$) when the current of disk electrode by ORR is zero ($i_{Disk,ORR}=0$). If the potential of disk electrode shift more negatively (i.e., more active ORR at disk electrode), the flux of oxygen to the ring electrode decreases resulting in the decrease of ORR current at the ring electrode (Equation 4.19).

$$i_{Ring} = i_{Ring}^{i_{Disk,ORR}=0} - N \times i_{Disk,ORR} \tag{4.19}$$

From Equation 4.19, the collection efficiency (*N*) can be experimentally measured

$$N = \frac{i_{Ring}^{i_{Disk,ORR}=0} - i_{Ring}^{i_{Disk,ORR},\lim}}{i_{Disk,ORR,\lim}} \tag{4.20}$$

Moreover, the ORR current at disk electrode can be calculated by plugging Equation 4.20 to Equation 4.19

$$i_{Ring} = i_{Ring}^{i_{Disk,ORR}=0} - \left(\frac{i_{Ring}^{i_{Disk,ORR}=0} - i_{Ring}^{i_{Disk,ORR},\lim}}{i_{Disk,ORR,\lim}} \right) \times i_{Disk,ORR} \tag{4.21}$$

By rearranging Equation 4.21, the calculated ORR current at disk electrode is

$$i_{Disk,ORR} = \frac{i_{Ring}^{i_{Disk,ORR}=0} - i_{Ring}}{\left(\frac{i_{Ring}^{i_{Disk,ORR}=0} - i_{Ring}^{i_{Disk,ORR},\lim}}{i_{Disk,ORR,\lim}} \right)} \tag{4.22}$$

When we use a Pt black catalyst on a GC disk electrode, the current generated at the disk electrode comes from a variety of electrochemical reactions such as Pt

oxide formation/reduction, hydrogen adsorption/desorption, and double-layer capacitance in addition of oxygen reduction (ORR). Therefore, we can get a modified current profile ($i_{Disk,\mathrm{mod}}$) that only ORR current was eliminated from disk electrode which means only current by Pt oxide formation/reduction, H_2O double layer capacitance, hydrogen ad/desorption remain. We can get the Equation 4.24 by plugging the Equation 4.22 into Equation 4.23.

$$i_{Disk,\mathrm{mod}} = i_{Disk} - i_{Disk,ORR} \tag{4.23}$$

$$i_{Disk,\mathrm{mod}} = i_{Disk} - \frac{i_{Ring}^{i_{Disk,ORR}=0} - i_{Ring}}{\left(\frac{i_{Ring}^{i_{Disk,ORR}=0} - i_{Ring}^{i_{Disk,ORR},\mathrm{lim}}}{i_{Ding,ORR,\mathrm{lim}}} \right)} \tag{4.24}$$

Therefore, by using this Equation 4.23, Pt oxide formation/reduction property can be measured under the ORR condition simultaneously as well as its relationship.

Figure 4.6 (a), (b), (c) shows the measured disk current, the measured ring current, the calculated ORR current at disk ($i_{Disk,ORR}$) and the calculated modified current at disk ($i_{Disk,\mathrm{mod}}$) under each N_2, air, O_2 saturated 0.5 M H_2SO_4 acid solution condition. Here the potential of ring electrode was held at 0.4 V_{RHE} during experiment and the ring current ($i_{Ring}^{i_{Disk,ORR}=0}$) is measured when the disk potential is around 1.2 V_{RHE} where the ORR current at disk electrode is zero. As like as $i_{Ring}^{i_{Disk,ORR}=0}$, the $i_{Ring}^{i_{Disk,ORR},\mathrm{lim}}$ was measured when the disk potential is around 0.4 V_{RHE} where the ORR current at disk electrode is maximum ($i_{Disk,ORR,\mathrm{lim}}$).

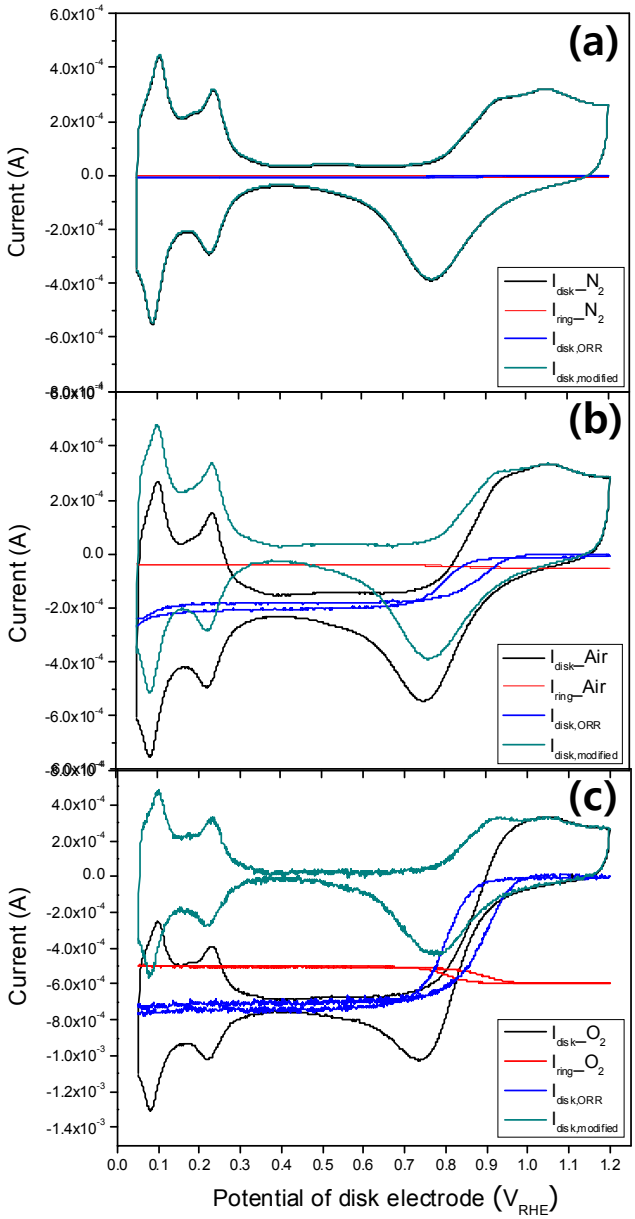

Figure 4.6 Measured current at disk electrode (i_{Disk}, black), Measured ring current (i_{Ring}, red), calculated ORR current at disk electrode ($i_{Disk,ORR}$, blue) and modified current at disk electrode ($i_{Disk,mod}$, green) of (a) N_2, (b) air, (c) O_2 saturated 0.5 M H_2SO_4 solution.
Pt black coated film on GC electrode (disk; 50 mVs^{-1} scan) – Pt (ring, 0.4 V_{RHE} hold) with 1600rpm

Figure 4.7 (a) shows the merge of the modified disk current ($i_{Disk,\mathrm{mod}}$) at each N_2, air, O_2 condition. The modified current response of air and O_2 condition are very similar to the current response of N_2 condition because the ORR induced current at disk electrode was eliminated. As seen in Figure 4.4 (a) and 4.4 (b), Pt oxide formation was accelerated in the presence of ORR at below 1.0 V_{RHE}; the Pt oxide reduction charge also increased in the presence of oxygen in the acid solution. Figure 4.7 (b) shows the Pt oxide coverage normalized by each electrochemical surface area (ECSA).

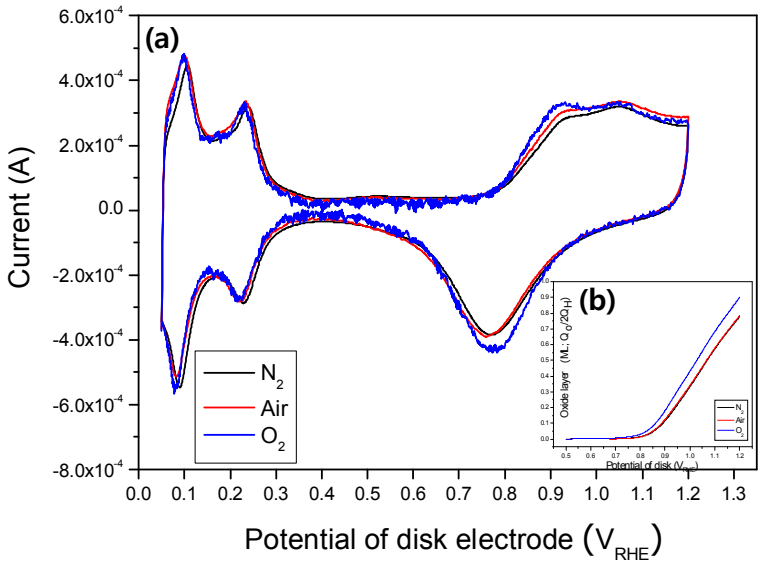

Figure 4.7 (a) Modified disk electrode current ($i_{Disk,mod}$) of N_2, air, O_2 condition. (b) Pt oxide coverage (ML) normalized by each ECSA.

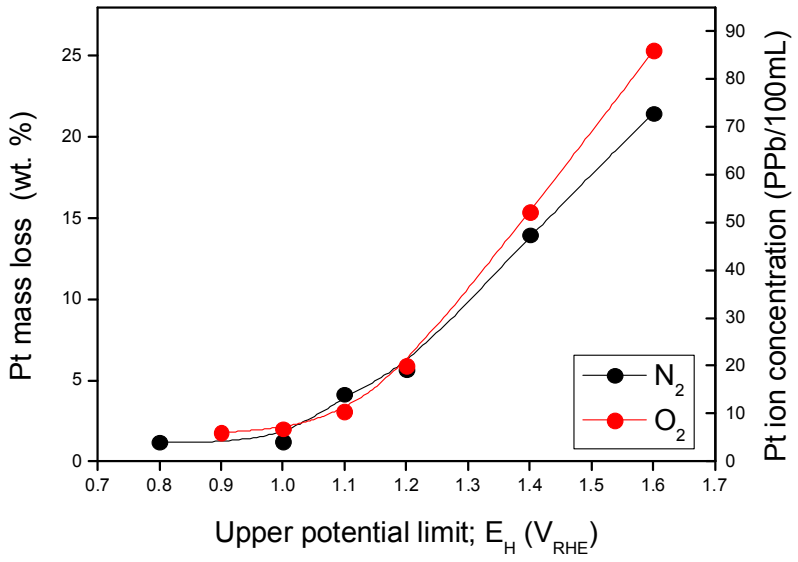

Figure 4.8 Pt mass loss (wt. %) and Pt ion concentration after accelerated degradation test (ADT) (0.5 V – E_H, 500 mV/s, 500 cycles) in N_2 and O_2 saturated in the 0.5 M H_2SO_4 solution (100 ml), ω = 1600 rpm.

4.3.3 Pt dissolution under ORR condition.

Figure 4.8 shows the Pt catalyst mass loss (%) and Pt ion concentration in the acid solution by ICP-MS analysis after accelerated degradation test (ADT) to reveal the relationship between protective the Pt oxide layer and Pt dissolution under N_2, O_2 saturated condition. The accelerating effects of voltage cycling on Pt dissolution and ECSA loss are generally ascribed to restructuring of Pt surface by repeated formation and reduction of place-exchanged oxide film. Moreover, the higher upper potential limits (E_H) extend the degree to which the surface experiences place exchange between Pt and O atoms. For accelerated degradation testing with an upper cycling

potential limit (E_H) of 1.6 V_{RHE}, the Pt dissolution is shown to be significantly greater in O_2-saturated acid solutions relative to N_2-saturated solutions only above 1.4 V_{RHE} of E_H.

Although the degradation analysis that take into consideration the influence of oxygen have been very limited to date, we can consider several possibilities. The first one is chemical dissolution of PtO_2 that is formed above E_H=1.4 V_{RHE}. Matsumoto *et al*. (73) showed that Pt dissolution was enhanced by the presence of oxygen, even in the lower potential regions (PtO or PtOH formation potential region), and proposed that the oxygen in an electrolytes (0.5M H_2SO_4) reacts with the Pt surfaces accompanied with place-exchanged surface reconstruction even at lower potentials by cathodic dissolution of surface oxide formed in an O_2 atmosphere during the oxygen reduction reactions. The Pt oxide layer accelerates Pt dissolution by chemical reaction such as the mechanisms described by Equation 4.25 and 4.26.

$$PtO_2 + 4H+ \rightarrow Pt^{4+} + 2H_2O \tag{4.25}$$

$$PtO + 2H+ \rightarrow Pt^{2+} + H_2O \tag{4.26}$$

Moreover, Mitsushima *et al.* (48) showed the Pt concentration increased in the air and oxygen atmospheres, and steady value after 50 hr in 1 M H_2SO_4 solution, and the detected mobile species was Pt^{4+} by measurement with $SnCl_2$ which is a reducing agent for Pt^{4+} , hence $Pt(OH)_3^+$. The proposed dissolution mechanism is shown as Equation 4.27

$$PtO_2 + H_2O + H^+ \rightarrow Pt(OH)_3^+ \tag{4.27}$$

The Pt dissolution concentration measurement in these two studies, however, was fulfilled after very long time dipping (about 50 hr) of Pt electrode into 0.5 M or 1 M H_2SO_4 solution when compared to this study (less than 30min).

The second mechanism is by place-exchange induced Pt dissolution acceleration. Just as the ORR reaction changes the quantity and nature of Pt oxide, the acceleration below 0.95 V_{RHE} (or 1.0 V_{RHE}) and inhibition of Pt oxide formation at above (or 1.0 V_{RHE}) in the presence of oxygen might accelerate Pt dissolution by increasing extent of place exchange and changing the location of Pt species in the oxide layer, thereby modify the fraction of mobile Pt species that can be recaptured by the Pt surface upon stripping of the oxide, and the fraction of those species that move away from the surface.

The third reason can be ascribed to the Pt dissolution during PtO_2 reduction process that will be shown at Figure 4.9 (a) and (b). Figure 4.9 (a) shows a comparison of the cyclic voltammograms for electrodes exposed to an N_2-saturated solution (solid line) and an O_2-saturated solution (dash line). There is an obvious offset in the O_2-saturated case due to mass-transport limited ORR. Figure 4.9 (b) shows the oxidation peaks at ring electrode held at 1.4 V_{RHE} during CV cathodic scan at disk electrode (Figure 4.9 (a)) under 3000 rpm convection and N_2, O_2 saturated condition. The increasing size and height and a shift toward negatively potential of oxidation peaks are in accordance with the upper potential limit (E_H) and the reduction peak at the disk electrode at both gas condition. So, we can propose that this oxidation peak at ring electrode is strongly due to the increase in the amount of

PtO_2. Moreover, we can see that the oxidation charge in the case of O_2 condition is bigger than those of N_2 condition at all upper potential limit tests.

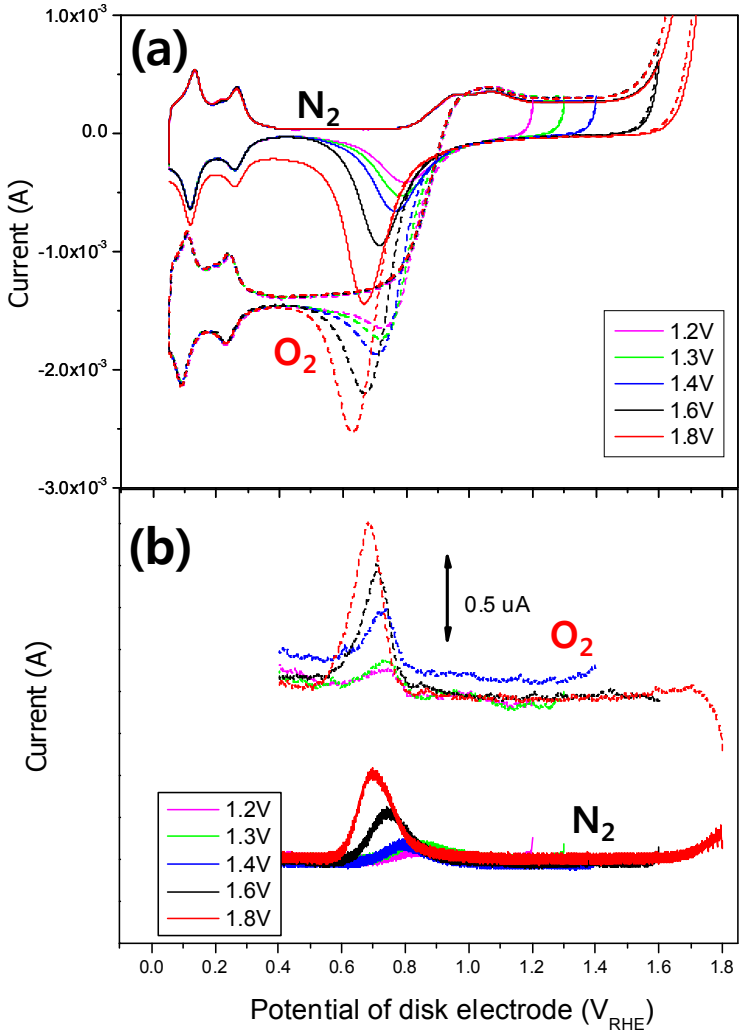

Figure 4.9 RRDE measurement (with various E_H) in N_2 and O_2 saturated 0.5M H_2SO_4 at a scan rate of 50 mVs^{-1} of disk electrode, ω=3000 rpm

(a) Disk current of N_2 (solid line), O_2 (dashed line)

(b) Ring current of N_2 (solid line), O_2 (dashed line) (E_{ring} = 1.4 V_{RHE})

If this oxidation peak at ring electrode is regarded as Pt^{2+} as like as Johnson *et al*. (52) proposed that Pt^{2+} form during reduction of Pt oxide ($PtO_2 + 4H^+ + 2e^- \rightarrow Pt^{2+} + 2H_2O$) with rotating ring disk electrode (RRDE) and Inzelt *et al.*(81) proposed the detachment of the Pt atoms or clusters during the reduction of Pt oxides, we can proposed that oxygen reduction reaction (ORR) accelerate Pt dissolution during PtO_2 reduction process as well as overall Pt dissolution acceleration as shown at Figure 4.8. The result of Bi *et al*.(74) that the effect of oxygen partial pressure on cathode degradation was insignificant up to 1.2 V_{RHE} condition at PEMFC can be explained by the Figure 4.8 and Figure 4.9 (b).

From the results of this study, we can assume that the O_2 condition at cathode side may show significant Pt dissolution difference compared to N_2 or air condition at the PEMFC abuse test condition where the electrode potential goes up to 1.5 V_{RHE} such as PEMFC start/stop or fuel starvation condition, not at just normal operating condition of PEMFC such as at below 1.2 V_{RHE}.

4.4 CONCLUSION

It was observed that the Pt oxide formation and reduction strongly depends on oxygen reduction reaction (ORR) by gas changing LSV experiment, SWV by RDE and shielding effect method by RRDE.

At below 0.95 V_{RHE} ~ 1.0 V_{RHE}, ORR increases Pt oxide formation either by facilitating oxygen dissociative or associative adsorption. On the contrary, at above

0.95 V_{RHE} ~ 1.0 V_{RHE}, electrochemical oxidation of Pt from H_2O appears to be hindered by competition with the oxygen reduction reaction.

Potential cycling (E_H > 1.4 V_{RHE}) in an O_2-saturated solution revealed a greater Pt loss than in N_2-saturated solution. Dissolved oxygen in 0.5M H_2SO_4 solution appears to play a role in changing the Pt oxide property from the onset potential of Pt oxide formation as well as the PtO_2 layer property that protect Pt dissolution at higher potential region.

With ORR condition, we found that Pt dissolution by PtO_2 reduction process also is more accelerated than N_2 or air condition by comparing Pt^{2+} oxidation peak at ring electrode of RRDE experiment.

CHAPTER 5

The use of Scanning Electrochemical Microscopy (SECM) for the detection of mobile species during Pt oxide reduction

5.1 INTRODUCTION

Although advantages of proton exchange membrane fuel cell (PEMFC) such as high efficiency and low waste emission attract increasing attention as automobile vehicles (8), the implementation of the PEMFC technology in commercial market is still hindered by the long time performance stability, such as the dissolution or sintering of platinum electrocatalysts, carbon support corrosion, and membrane degradations, the electrochemical active area (ECSA) loss (4). The electrocatalyst degradation in the PEMFC cathode has been studied extensively, and is generally agreed to be related to three major mechanisms; Ostwald ripening (Pt dissolution and redeposition onto lower surface energy sites) (28-29), coalescence of Pt nanoparticles via migration and surface diffusion on the carbon supports (23, 28, 35), and carbon corrosion-induced Pt detachment or agglomeration (44).

Especially, Birss *et al*. (82) indicated that platinum dissolution accompanied with repeated oxide growth and reduction cycles and other research groups (17, 48, 83) have studied and showed how much platinum dissolve under potential cycling of platinum electrodes to a range in which oxides are formed and subsequently stripped and loss of electrochemically active surface area (ECSA) that is more rapid than holding the potential at either the upper or lower potential limit. When it comes to the

relationship between platinum dissolution and platinum oxide, some literature suggests that the presence of platinum oxide can help to protect the platinum surface from anodic platinum dissolution at higher potentials holding (29), on the contrary, the dynamic platinum surface reconstructions due to place exchange by platinum oxide formation/reduction cycles also enhance the platinum dissolution (17).

For PEMFC used in an automobile, the start/stop procedure is an additional, moreover much severe electrocatalyst dissolution mechanism. Reiser *et al*. (15) showed that during start-up procedure the anode is locally starved from proton and it cause the difference in potential in the oxygen exposed region of the anode, which results in an increase cathode potential up to 1.5 V_{RHE} and decrease to normal operation potential 0.5 ~ 1.0 V_{RHE} as hydrogen gas replace the room oxygen or air reside. This start-up procedure is very similar with potential cycling or potential step experiment between 0.5 ~ 1.5 V_{RHE} of accelerated degradation test (ADT). It is estimated that about 30,000 detrimental start-up events occur during PEMFC lifetime for automobile (14). This means during PEMFC of automobile suffers at least 30,000 times platinum oxidation/reduction cycling or potential step.

As described above, the platinum catalyst of PEMFC for automobile suffers two types of platinum loss from the surface of the electrode. The first one is direct dissolution (Equation 5.1) in the course of increasing potential up to 1.5 V_{RHE}, which occurs simultaneously with platinum oxide formation such as Equation 5.2 and 5.3.

$$Pt \leftrightarrow Pt^{2+} + 2e^- \qquad E(V_{RHE}) = 1.188V + 0.0295\log[Pt^{2+}] \qquad (5.1)$$

$$Pt+H_2O \leftrightarrow PtO+2H^+ +2e^- \qquad E^o=0.98\ V_{RHE} \tag{5.2}$$

$$Pt+2H_2O \leftrightarrow PtO_2+4H^+ +4e^- \qquad E^o=1.045\ V_{RHE} \tag{5.3}$$

The second one is the platinum dissolution during the platinum oxide reduction which is either by a mechanical detachment of Pt atoms (or clusters) or the reduction of PtO_2 (Pt^{4+}) that formed at higher positive potential. You *et al*. (84) proposed the physical Pt atoms detachment process is related to the surface restructuring during the formation of platinum oxide which resulting in an interfacial place exchange of the oxygen and platinum atom, and some of platinum atoms do not reduce during the reduction of PtO_2 due to the separation from bulk platinum by oxygen atoms. Johnson *et al*. (52) proposed by using rotating ring disk electrode (RRDE) that the platinum dissolution occurs during the reduction of platinum oxide (PtO_2), suggesting the thermodynamic Equation 5.4.

$$PtO_2+4H^+ +2e^- \rightarrow Pt^{2+} +2H_2O \tag{5.4}$$

Moreover, recently Umeda *et al*. (85) and Yadav *et al*. (83) observed platinum ion detection at ring or the second working electrode during PtO_2 reduction process respectively and suggested Equation 5.5.

$$PtO_2+4H^+ +2(2-x)e^- \leftrightarrow xPt^{2+} +(1-x)Pt+2H_2O \qquad E^o=0.837V + 0.0295\log[Pt^{2+}] \tag{5.5}$$

In the present study, in order to understand the platinum dissolution mechanism we investigated what the mobile species is generated during PtO_2 reduction by using rotating ring disk electrode (RRDE) and scanning electorochemical microscopy (SECM).

5.2 EXPERIMENTAL

5.2.1 RRDE experiment

A catalyst layer was fabricated on a glassy carbon working electrode by dispersing 30 mg of Pt-black catalyst (E-Tek) and 180mg of 5wt% Nafion solution (Aldrich) in the mixture of 2 mL of isopropyl alcohol and 4.5mL of distilled pure water. The solution was ultrasonicated until a dark homogeneous dispersion was formed during about 1hr; 8μL of the dispersed ink solution was dropped onto the glassy carbon (GC) disk electrode of rotating ring disk electrode (RRDE, Pine Inc.) to give a catalyst loading of 35,800 ng. The loading was 144.6 $ugcm^{-2}$ for RRDE and the electrodes were subsequently dried in the atmosphere of ultra pure N_2 gas (99.999%).

100ml of 0.5 M H_2SO_4 electrolyte solution (97% metal grade, Alfa Aesar, diluted with deionized Milli-Q H_2O) was de-aerated with vigorous bubbling with very high purity N_2 for 1hr before each electrochemical test; continuous purging was maintained during the experiment. Prior to the measurements, the working electrode was pretreated by a potential cycle (CHI760C, CH Instruments Inc.) between 0.05 ~ 1.0 V_{RHE} at a rate of 100 mVs^{-1} for 20 cycles. The hydrogen electrode (HydroFlex, Gaskatel GmbH Inc.) and Pt wire electrode separated by glass frit were also used as reference and counter electrode.

The detection of mobile platinum species during Pt oxide reduction was investigated at N_2 condition using a rotating ring disk electrode. A Pt catalyst loaded

on GC disk – Au ring electrode (E7R9, PINE Inc.) was CV scanned with $50mVs^{-1}$ scan rate between 0.05 ~ 1.6 V_{RHE} at 1.4 V_{RHE} of ring potential hold.

5.2.2 SECM experiment

The 100 μm diameter platinum wire (99.99%, Devon) and 100 μm diameter gold wire (99.99%, Devon) were used to fabricate the SECM tip or substrate (RG (r_g/a) < 2) by heat sealing the corresponding Pt wire under vacuum in a borosilicate glass capillary. Commercially made 25 μm diameter platinum ultramicroelectrode UME (99.99%, CHI instrument) was also used for tip electrode. The 200 μm diameter of glassy carbon (GC) UME was prepared by etching method. For details, a glassy carbon rod is immersed in concentrated base (KOH, NaOH) along with a graphite counter electrode and a DC voltage is applied between them in order to etch the GC rod. The magnitude of the DC voltage and the time required to dissolve the rod depends on the final size required for the experiments to be performed (i.e. 200 μm). Once the rod has been etched to the desired size, the newly formed rod is rinsed with water, acetone and dried at room temperature. Then, the GC tip is placed at one of the ends of a borosilicate capillary and a connection is made between the GC tip and copper wire with silver epoxy paste. Finally, the GC exposed UME is covered with several layers of cathodic paint and one final layer of epoxy resin to ensure perfect insulation. The excess of cathodic paint and epoxy resin were polished to expose a disk shaped electrode to perform the experiments.

Both electrodes were polished with 50 nm diameter sized alumina paste (Buehler, Lake Bluff) on microcloth pad and then sonicated in deionized Milli-Q H_2O. Prior to the measurements, both electrodes were cycled (CHI920C, CH Instruments Inc.) between 0.05 ~ 1.0 V_{RHE} at a rate of 100 mVs^{-1} for 20 cycles in 0.5 M H_2SO_4 electrolyte solution for cleaning and then washed by deionized Milli-Q H_2O. The hydrogen electrode (HydroFlex, Gaskatel GmbH Inc.) and tungsten wire electrode (0.5 mm, Danvers, MA) was used as reference and counter electrode.

0.1 M Phosphate buffer solution pH 4.5 (monobasic, Alfa Aesar, Teknova) was used as was received. Amplexultrared (Modified N-acetyl-3,7-dihydroxyphenoxanzine, Invitrogen. Inc) was dissolved to 2 mM in dimethyl sulfoxide (DMSO) immediately on arrival, divided into 250 μl and stored at -20 ^{o}C until immediately before use. Horseradish peroxidase (HRP, 200U/mg, fisher Scientific, Thermo Scientific,) also was dissolved to 300 U/mL HRP in 0.1 M potassium phosphate pH 4.5 (monobasic) as stock solution and was stored at 4 ^{o}C, and then diluted to 5 U/mL (excess compared to Amplexultrared concentration) with 0.1 M potassium phosphate pH 4.5 for experiments. All solutions used in the electrochemical experiments were purged with argon before and during the electrochemical tests.

The general reaction mechanism of peroxidase with substrate (here, Amplexultrared) proceeds in three distinct steps(86). H_2O_2 reacts rapidly with the ferric enzyme in a two-electron process to generate the intermediate known as

compound I. compound I stores the two oxidizing equivalents from peroxide as oxyferryl iron [Fe(IV)=O] and a π-cation radical delocalized over the haem ring (87), thus giving a formal oxidation state of +5. And the compound I is discharged in two sequential single-electron reactions with reducing substrate, producing radical products and water (88).

Here, U (unit) represents a specific activity of peroxidase enzyme catalyst to form 1.0 mg purpurogallin from one pyrogallol unit in 20 sec at pH 6.0 and 20 ^{o}C. The reaction is shown at Figure 5.1.

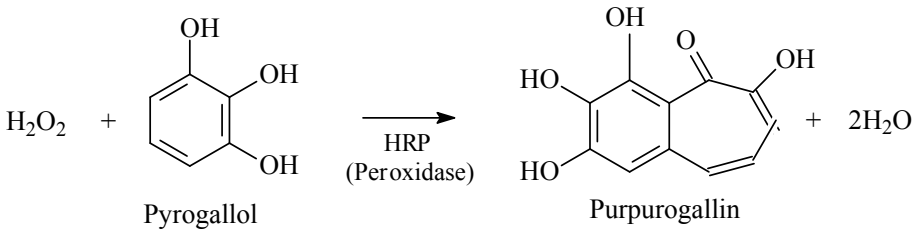

Figure 5.1 Oxidation reaction of Pyrogallol to purpurogallin when catalysed by horse radish peroxidase enzyme catalyst.

Figure 5.2 shows the positioning and alignment of the Pt tip and GC substrate that was fulfilled by using positive feedback (tip generation/substrate collection) mode with the mediator of 1 mM of ferrocenemethanol (97 % FcMeOH, Sigma Aldrich) in 0.1 M sodium nitrate ($NaNO_3$, Sigma Aldrich) solution. The Pt tip was scanned x, y directions and approached to the GC substrate for optimizing the

positive feedback current (Figure 5.2 (b)). The tip was positioned in the z direction by means of a positive feedback approach curve at a rate of 0.5 $\mu m\, s^{-1}$. A successful approach was considered and estimated collection efficiency higher than 98 % was achieved upon a CV scan under positive feedback conditions (Figure 5.2 (c)). A good indicator for a successful alignment of the electrodes is the collapse of the substrate and tip currents to the same curve, which indicates nearly 100 % collection efficiency.

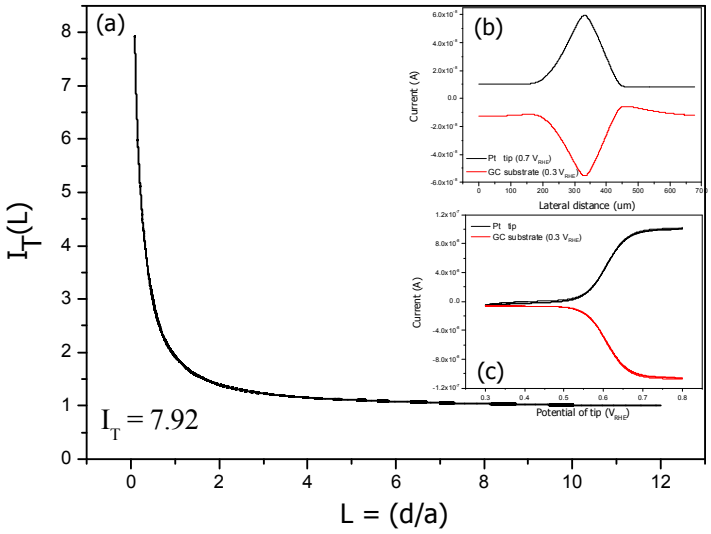

Figure 5.2 (a) Approach curve at the centered position between tip (100 μm diameter Pt UME) and substrate (200 μm diameter GC UME).

(b) Line scan of the tip over the substrate, showing a desirable symmetry in the electrochemical response (E_{tip} = 0.7 V_{RHE}, E_{sub} = 0.3 V_{RHE})

(c) Cycle voltammetry at optimal centered position in which the tip is being scanned from 0.3 ~ 0.8 V_{RHE} with 50mV/s scan rate and the substrate is held at 0.3 V_{RHE}.

Distance between tip and substrate was estimated by normalizing dimensionless form of $I_T(L)$ $(= i_T(L)/i_{T\infty})$ through L (d/a) to using the numerical Equation 5.6 (42), where $i_{T\infty}$ is current of the UME tip at 'infinite' distance from the substrate and $i_T(L)$ is the current read at a given distance from the substrate. The estimated distance between tip and substrate in this SECM experiment was about 5 ~ 5.5 μm by the Equation 5.6.

$$I_T(L) = 0.68 + \frac{0.78377}{L} + 0.3315\exp(\frac{-1.0672}{L}) \quad (5.6)$$

5.3 RESULTS AND DISCUSSION

5.3.1 Mobile species detection generated during reduction of Pt oxide

There are a lot of observations supporting that Pt surface area loss is induced by Pt dissolution and redeposition; (i) ECSA loss proportional to the potential limit(89), (ii) detection of Pt nanocrystals in the ion-conducting phase(90), (iii) ECSA loss accelerated by potential cycling(91), (iv) changes in the size and distributions of Pt nanoparticles in PEMFC with operation time(92). In particular, Aragane *et al*. (93-94) reported the presence of Pt nanocrystals in the matrix of fuel cell and Pt loss from the cathode, which provided direct evidence for Pt dissolution from Pt nanoparticles in the cathode and reduction of soluble Pt species with permeated hydrogen gas molecules in the membrane phase (i.e. $Pt^{z+} + (z/2)H_2 \rightarrow Pt + 2H^+$). In addition, Yasuda *et al*. (95-96) detected the appearance of numerous Pt single crystals of 10~100 nm in

the membrane after long time operation in air or N_2 in PEMFC and the amount of Pt found in the membrane was shown to increase with increasing cathode potentials.

Previously, in the introduction part of this chapter we proposed that the main electrochemical reaction processes of Pt dissolution follow direct dissolution (Equation 5.1) and platinum dissolution during the platinum oxide reduction (Equation 5.4). Therefore, we wanted to investigate whether we might determine the nature of species that are generated during PtO_2 reduction process. As such, we conducted RRDE and SECM experiments to detect mobile species under potential cycling.

Figure 5.3 shows the result from RRDE (scan rate 50 mVs^{-1}, 3000 rpm) and SECM (scan rate 300 mVs^{-1}) experiments respectively in 0.5M H_2SO_4. Figure 5.3 (a_1) and 5.3 (b_1) show the current generated on the disk (Pt black on GC) or tip (25 μm diameter Pt UME) electrode and Figure 5.3 (a_2) and 5.3 (b_2) reveal the current at the ring (Au, E_{ring} = 1.4 V_{RHE}) or substrate (100 μm diameter of Au, E_{sub} = 1.4 V_{RHE}) electrode as a function of ring of substrate potential during cathodic scan of disk or tip electrode. Based on both results, we can see that increasing the upper potential limit of the disk or tip electrode are an increase in the oxidation charge at ring or substrate electrode during the cathodic scan of disk or tip electrode and a shift of the oxidation peak potential of the ring or substrate electrode toward more negative potential values, in proportional to the reduction peak potential shift for disk or tip electrode.

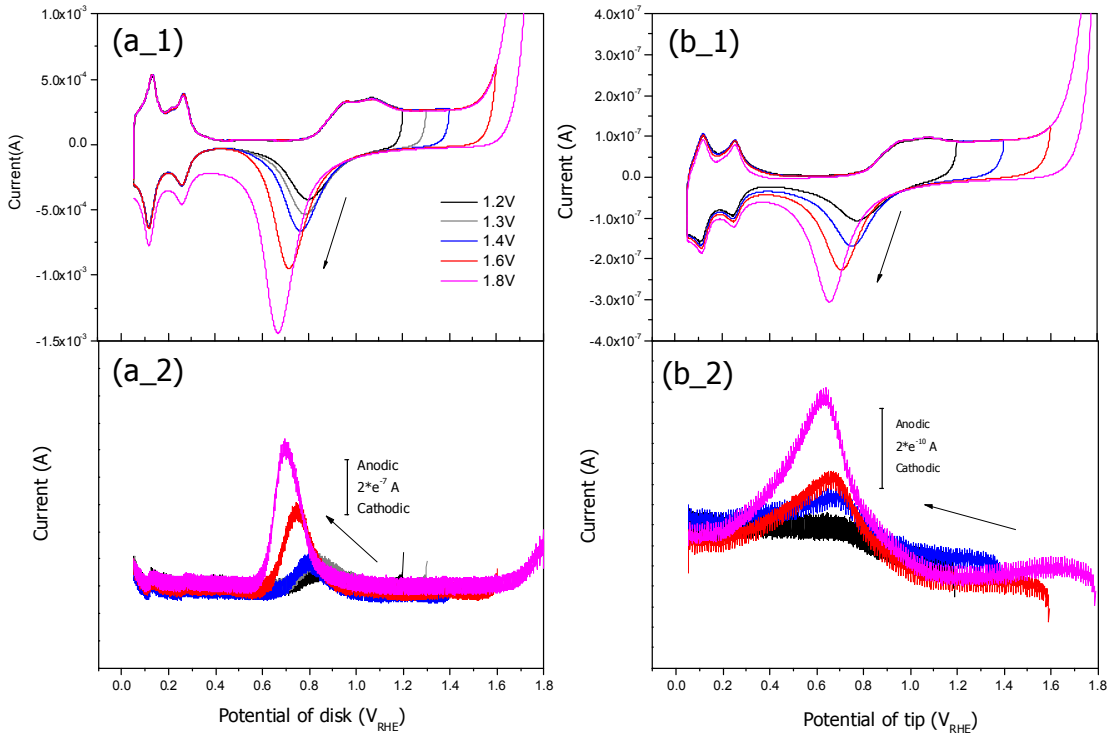

Figure 5.3 (a_1) Current vs potential of disk electrode (Pt black on GC) at RRDE experiment in N_2 saturated 0.5M H_2SO_4 at a scan rate of 50 mV/s with various upper limit potentials (E_H), ω =3000 rpm

(a_2) Current response at ring electrode (Au) with various upper limit potentials of disk electrode, E_{ring} = 1.4 V_{RHE}.

(b_1) Current vs potential of tip electrode (25 μm diameter Pt UME) at SECM experiment in argon saturate 0.5M H_2SO_4 at a scan rate of 300 mV/s of tip electrode with various upper limit potentials (E_H).

(b_2) Current response at substrate electrode (100 μm diameter Au UME) with various upper limit potentials of tip electrode, $E_{substrate}$= 1.4 V_{RHE}.

Based on these results, oxidizable mobile species in solution appear to be generated at the disk or tip electrode only during the reduction of the oxide peak which is strongly related to the increasing the amount of PtO_2 that is enhanced by increasing the upper potential limit of the disk or tip electrode (50).

We see experiment results look similar to the interpretation of experiments by Johnson *et al*. (52) who suggested that the oxidation peak at ring electrode results from the electrochemical oxidation of Pt^{2+} ($Pt^{2+} \rightarrow Pt^{4+} + 2e^-$) at the ring electrode as this species is generated at the disk electrode by the electrochemical reduction reaction shown by the reaction described in Equation 5.4. However, we also note that when the ring potential was held at very low potentials we saw no reducible peak ($Pt^{2+} + 2e^- \rightarrow Pt$) in the ring or substrate electrode under same condition of Figure 5.3. As shown at Figure 5.4 (a_2 & b_2), the oxidation peak at ring or substrate electrode appears even around 0.9 V_{RHE} ~ 1.0 V_{RHE} of ring or substrate electrode in which potential Pt^{2+} is hard to oxidize to Pt^{4+}. Moreover, the potential around 0.6 ~ 0.7 V_{RHE} of disk or tip that Pt^{2+} was generated during PtO_2 reduction was too negative for Pt^{2+} to be transferred to the ring or substrate by diffusion, the distance of tip and substrate is very close around 5 μm though. It might be more kinetically favorable for Pt^{2+} to reduce to Pt metal than to diffuse out to the solution at that potential of 0.6 ~ 0.7 V_{RHE}. So, we tentatively concluded that the oxidation peak might be not from Pt^{2+} oxidation or at least from a mixture of mobile species of Pt and other species like H_2O_2 or oxygen containing species.

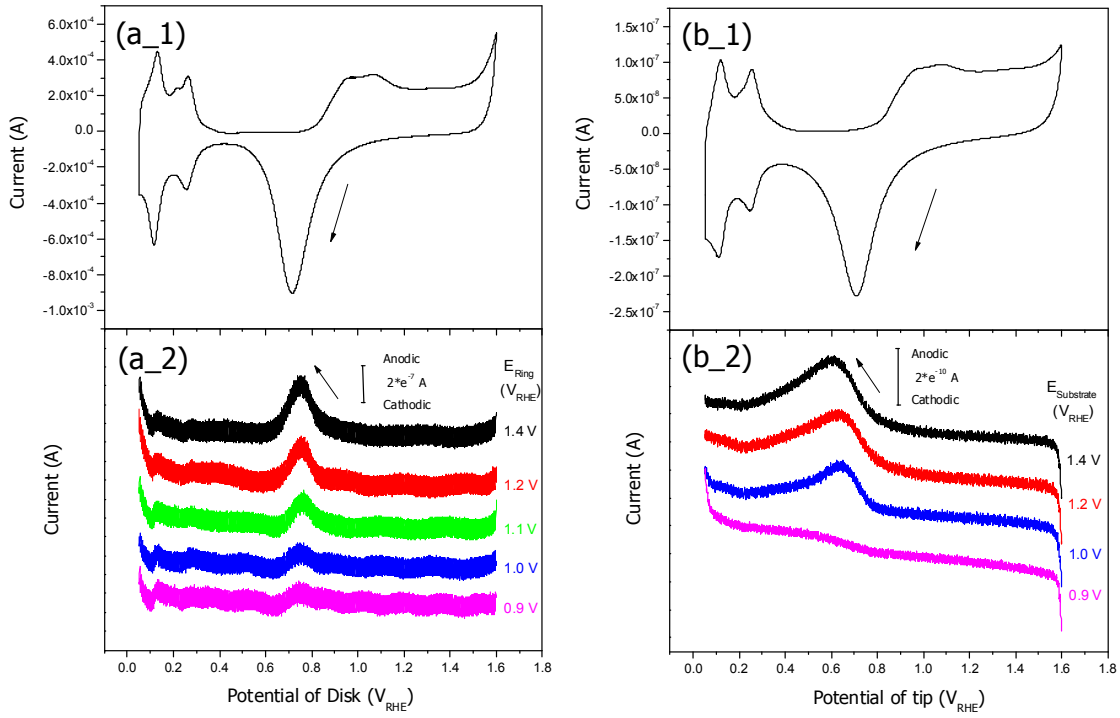

Figure 5.4 (a_1) Current vs disk electrode (Pt black on GC) potential of RRDE experiment in N_2 saturated 0.5M H_2SO_4 at a scan rate of 50 mV/s of disk electrode, ω =3000 rpm

(a_2) Current response at ring electrode (Au) with various holding potential during cathodic scan of disk electrode

(b_1) Current vs tip electrode (25 μm diameter Pt UME) potential of SECM experiment in Argon saturate 0.5M H_2SO_4 at a scan rate of 300 mV/s of tip electrode

(b_2) Current response at substrate electrode (100 μm diameter Au UME) with various holding potential during cathodic scan of tip electrode

5.3.2 Determining the nature of mobile species generated during reduction of Pt oxide

Because it is very hard to figure out the nature of mobile species generated during PtO_2 reduction process with conventional TG/SC (tip generation/substrate collection), we came up with the method to use the peroxidase material as mediator shown in Figure 5.5 to evaluate the mobile species generated at tip electrode with an assumption that a portion of the oxidation peak might come from hydrogen peroxide oxidation.

A method for low level detection of hydrogen peroxide by using a chemically activated redox mediator was studied by Lyon *et al*. (97) and showed that when electrochemically inert material (10-acetyl-3,7-dihydroxyphenoxanzine, AmplexRed) was chemically, irreversibly oxidized by as low as 8 pM of H_2O_2 in the presence of the enzyme horseradish peroxidase (HRP) as catalysts, the chemically oxidized material (resorufin) was detected by electrochemical reduction to dihydroresorufin at electrode surface which was held at reducible potential.

In this study, we used a modified N-acetyl-3,7-dihydroxyphenoxanzine (AmplexUltrared , Invitrogen, Inc) that has more sensitive property at low pH (~ pH 3) and enhanced sensibility instead of AmplexRed (10-acetyl-3,7-dihydroxyphenoxanzine, Invitrogen, Inc).

We also used 0.1 M potassium phosphate pH 4.5 buffer solution instead of 0.5 M H_2SO_4 because AmplexUltrared and HRP enzyme are unstable and lose its property very quickly at highly acid condition like 0.5 M H_2SO_4 solution.

Figure 5.5 shows the schematic of modified SECM TG/SC (tip generation / substrate generation) feedback mode fulfilled in 0.1M potassium phosphate pH 4.5 buffer solution containing 25 μM of AmplexUltrared (P). The inset is a CV (50mV/s on GC electrode) of 8 μM resorufin that has 0.34 V_{RHE} of E^o.

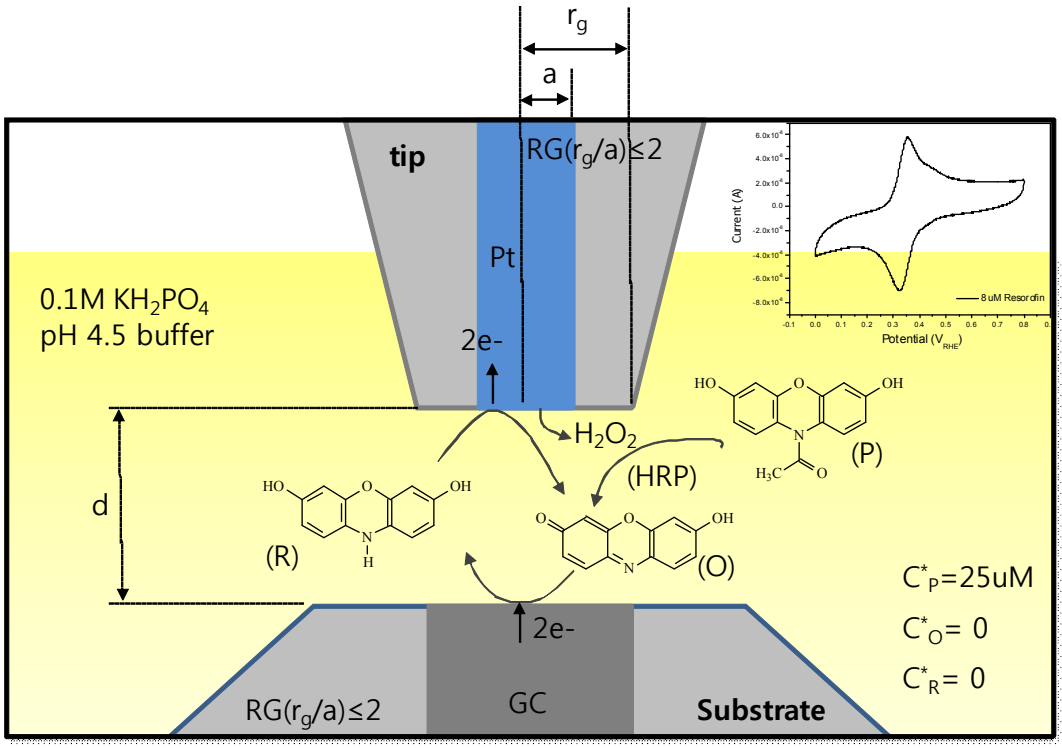

Figure 5.5 Schematic diagram of the SECM experiment used to detect H_2O_2 generated during PtO_2 reduction process. For this study, a (radius of Pt tip) = 50 μm, d = 5 μm, r_g = 100 μm, radius of GC substrate = 100 μm. Inset is CV (50 mV/s on 200 μm diameter of GC) of 8 μM resorufin (O) that have E^o of 0.34 V_{RHE}.

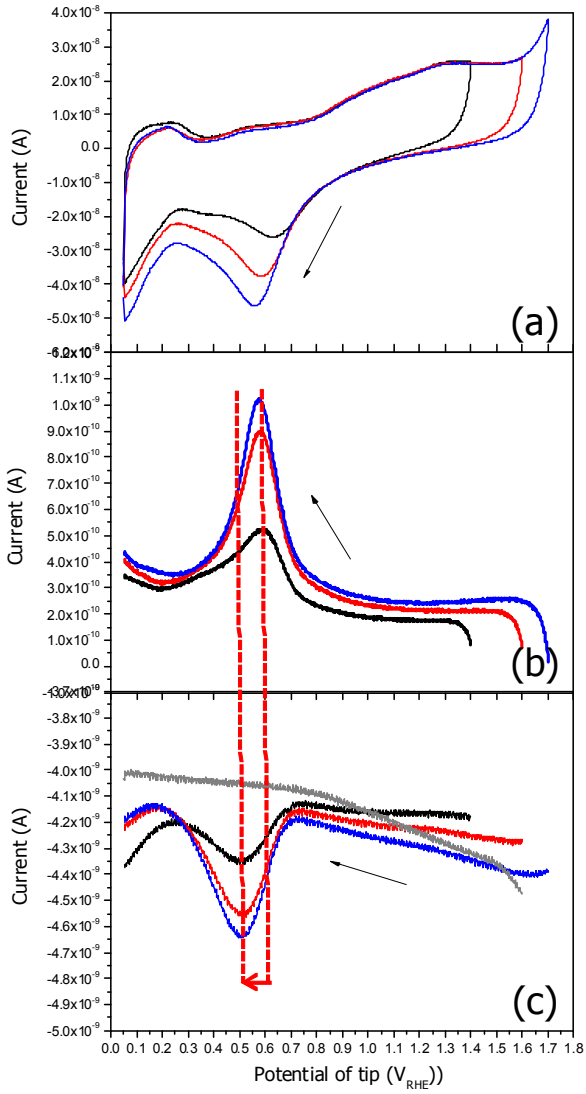

Figure 5.6 (a) Typical CV of tip (100 μm diameter Pt UME) with various E_H in 0.1M potassium phosphate buffer pH 4.5; scan rate of 100 mVs^{-1}
(b) Current response at substrate (200 μm diameter GC UME, $E_{substrate}$ = 1.4 V_{RHE}) during cathodic scan of tip
(c) Current response at substrate (200 μm diameter GC UME, $E_{substrate}$ = 0.1 V_{RHE}) during cathodic scan of tip electrode in 25 μM of Amplexultrared (Modified N-acetyl-3,7-dihydroxyphenoxanzine), 5 U/ml of horseradish peroxidase (HRP) and 0.1M potassium phosphate buffer pH 4.5; grey line is a current response where there is no HRP.

Figure 5.6 (a) shows the tip current with respect to potential scan of 100 mVs^{-1} in the 0.1M potassium phosphate pH 4.5 buffer solution with changing upper limit potential. Similarly to the Figure 5.3 of 0.5 M H_2SO_4 solution condition, we can also see from Figure 5.6 (b) that as the upper potential limit of the disk or tip electrode increases the oxidation charge at ring or substrate electrode during the cathodic scan of disk or tip electrode increases proportionally and shifts toward more negative potential values. And this oxidizable mobile species also appears to be generated at the disk or tip electrode only during the reduction of the oxide peak, which is strongly related to the increasing the amount of PtO_2 in 0.1 M potassium phosphate pH 4.5 buffer solution. Figure 5.6 (c) shows the reduction peaks in the presence of both AmplexUltrared and HRP at GC substrate electrode when the potential of substrate is held at 0.1 V_{RHE} during cathodic scan of Pt tip electrode.

To avoid an unwanted additive effect on the response reduction current from oxidized resorufin or reduced dihydroresorufin and residue of hydrogen peroxide, the SECM cell was washed with deionized H_2O_2 and 0.1 M potassium phosphate pH 4.5 buffer solution at least ten times during each measurement very cautiously without changing any geometrical setting such as tip-substrate alignment or gab distance. As similar as Figure 5.6 (b), the reduction charge in Figure 5.6 (c) shows increased value in proportional to the increase of the upper limit potential at Pt tip electrode which is related to the increased amount of PtO_2. However, unlike oxidation peaks in Figure 5.6 (b) that showed negatively shift with respect to the upper limit potential, the reduction peaks in Figure 5.6 (c) shows same peak potentials position as well as about

100mV negatively shift of peak potential regardless of upper limit potential. By comparison of oxidation and reduction charge calculated by numerical integration of the baseline subtracted voltammograms in Figure 5.6 (b) & 5.6 (c), we found that the reduction charge of each upper limit potential in Pt tip electrode is 64 %, 74 %, 80 % of each oxidation charge in Figure 5.6 (b) respectively. Regardless of the comparison of charge amount, shifted peak position between oxidation and reduction peak in Figure 5.6 (b) and 5.6 (c), we can conclude that hydrogen peroxide evolve from tip during PtO_2 reduction process and the amount of hydrogen peroxide evolution is strongly proportional to the amount of PtO_2 from the Figure 5.6 (c).

In order to explain the reason of reduction peak's negative shift that has the same peak position and to figure out how much hydrogen peroxide contribute to the oxidation and reduction charge, we set up simulation model of this SECM experiment at next chapter.

5.3.3 Simulation of SECM experiment

As described in Figure 5.5, for the development of the model in this study, the model assumes that the mediators undergo a simple diffusion controlled two electrode transfer at the tip and substrate electrode. In this study, digital simulation was fulfilled by COMSOL Multiphysics which uses finite element methods (FEM) for describing a variety of SECM problems in a versatile way. For instance, diffusion simulation coupling voltammetry to the SECM geometry described in Figure 5.5 in 2-D axial symmetry under transient condition was carried out using COMSOL Multiphysics

v.3.5a software (COMSOL, Inc). The simulation space (subdomain) was the usual SECM setup for two UME electrodes (Tip: a=25 μm, Substrate: a=50 μm, both $R_g \leq 2$) that were concentrically aligned. The gap between two UME electrodes is set to 5 μm which implies L=0.1.

The diffusion problem was solved under transient conditions (governing Equations) using concentration initial conditions in subdomain setting and boundary conditions in boundary setting on the tip and substrate electrodes. In the subdomain we consider both diffusive and kinetic compontents in which the species O (resorufin) are being generated and species P (modified N-acetyl-3,7-dihydroxyphenoxanzine), hydrogen peroxide are consumed by Equation 5.7 while species R is only diffusive functional. The kinetic component is assumed to be a second order process associate with a kinetic constant k.

$$\text{P (AmplexUltrared)} + H_2O_2 \xrightarrow[\substack{\text{HRP} \\ \text{(enzyme catalysts)}}]{k} \text{O (Resorufin)} \tag{5.7}$$

First, governing Equations can be described below by using Fick's second law

$$\frac{\partial C_p}{\partial t} = D_p \nabla^2 C_p - k C_p C_{H_2O_2} \tag{5.8}$$

$$\frac{\partial C_{H_2O_2}}{\partial t} = D_{H_2O_2} \nabla^2 C_{H_2O_2} - k C_p C_{H_2O_2} \tag{5.9}$$

$$\frac{\partial C_O}{\partial t} = D_O \nabla^2 C_O + k C_p C_{H_2O_2} \tag{5.10}$$

$$\frac{\partial C_R}{\partial t} = D_R \nabla^2 C_R \tag{5.11}$$

(where, P : modified N-acetyl-3,7-dihydroxyphenoxanzine, O : resorufin, R : dihydroresorufin)

The initial concentration condition of each species in bulk solution are set C_P = 25 μm (25e^{-3} mol/m^3), C_{H2O2}=0 mol/m^3, C_O=0 mol/m^3, C_R = 0 mol/m^3 (1 mol/m^3 = 1 mM).

At the tip boundary, z = 0, 0 < r < a, the condition is inward flux following Butler-Volmer kinetics and potentials sweep, following Equation 5.12.

$$\text{O (resorufin)} + 2e^- \underset{k_R}{\overset{k_f}{\rightleftharpoons}} \text{R (dihydroresorufin)} \tag{5.12}$$

$$-D_{H_2O_2} \nabla C_{H_2O_2} = N_{H_2O_2} \tag{5.13}$$

$$-D_O \nabla C_O = -k^o \, e^{(-\alpha f (E-E^o))} \, C_o(0,r) + k^o e^{((1-\alpha) f (E-E^o))} C_R(0,r) \tag{5.14}$$

$$-D_R \nabla C_R = k^o \, e^{(-\alpha f (E-E^o))} \, C_o(0,r) - k^o e^{((1-\alpha) f (E-E^o))} C_R(0,r) \tag{5.15}$$

$$E = E_{ini} - \upsilon t \tag{5.16}$$

Here the N_{H2O2} is flux of hydrogen peroxide generated from the tip electrode during PtO_2 reduction process and k^o is the heterogeneous rate constant chosen to be 0.1 ms^{-1} avoiding thus any kinetic complication at L = 0.1, α the symmetry factor equal to 0.5 and f which is equal to 38.94 V^{-1} at 298 K and E^o the formal standard potential of the reaction. E is the potential of the tip and relates the scan to time by

means of scan rate υ (100 mVs^{-1}) and E_{ini} represents the initial potential. In this simulation study, if we assume the oxidation charge at Figure 5.6_b is all from hydrogen peroxide oxidation, the mole flux of hydrogen peroxide generated from tip, N_{H2O2}, can be converted to like Figure 5.7.

Moreover, the equation of N_{H2O2} can be acquired by Lorentzian fitting the experimental data with time as shown at Equation 5.17, Table 5.1 and Figure 5.7 (a), (b), (c).

$$N_{H_2O_2}\left[\frac{mol}{m^2 s}\right] = \frac{A}{\left(1+\left(\frac{t-t_{pc}}{w}\right)^2\right)} \tag{5.17}$$

Table 5.1 Lorentzian fitting parameters of Equation 5.17

E_H	A	t_{pc}	w
1.4 V_{RHE}	$5.1101e^{-8}$	8.3305	1.1016
1.6 V_{RHE}	$1.1087e^{-7}$	10.2417	0.8956
1.7 V_{RHE}	$1.2410e^{-7}$	11.2516	0.7635

At the substrate boundary, $z = d$, $0 < r <$ a, the condition is also inward flux as same as Equation 5.14 & 5.15 and potentials was fixed at 0.1 V_{RHE}. Where C_P, C_{H2O2}, C_O and C_R are the concentrations of each species and are functions of r, z and time.

D_O and D_R are the diffusion coefficients of resorufin and dihydroresorufin in aqueous solution and are given the value of 6.6×10^{-10} m^2s^{-1} (98), the diffusion coefficient of AmplexUltrared, D_P, is assumed as same value and D_{H2O2} in aqueous solution is 1.6×10^{-9} m^2s^{-1} (99).

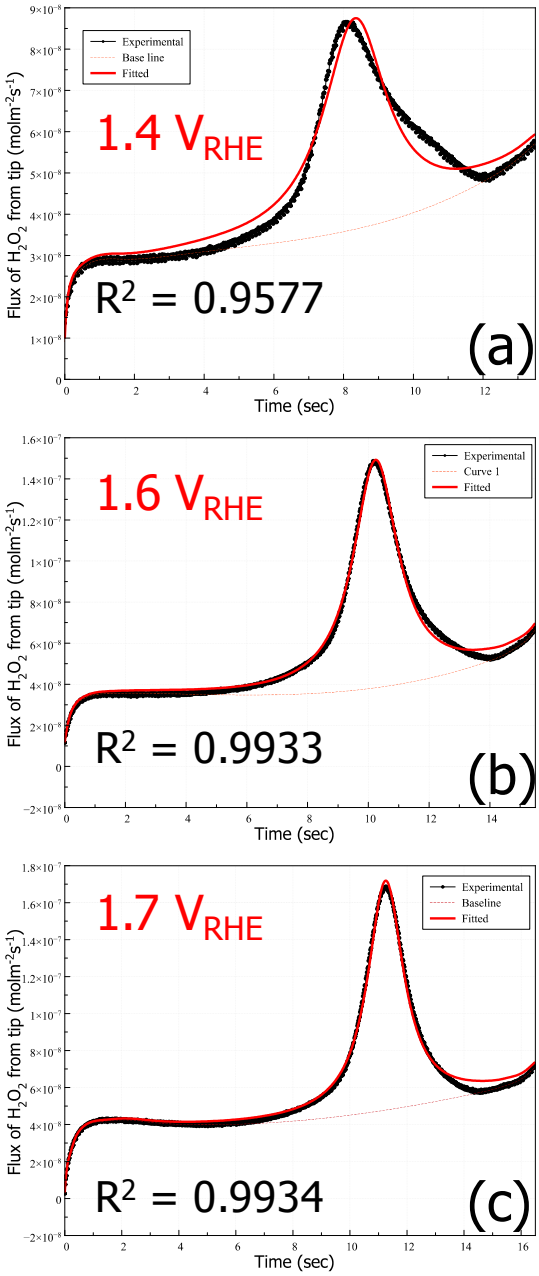

Figure 5.7 Flux of hydrogen peroxide [$molm^{-2}s^{-1}$] converted from Figure 5.6 (b) and fitting by Lorentz Equation (red line) and baseline (red dash)

(a) E_H = 1.4 V_{RHE} (0 ~ 13.5sec with 100mVs^{-1})

(b) E_H = 1.6 V_{RHE} (0 ~ 15.5sec with 100mVs^{-1})

(c) E_H = 1.7 V_{RHE} (0 ~ 16.5sec with 100mVs^{-1})

The current read at the tip and substrate are obtained by integrating the normal diffusive flux of the oxidized species at its surface and multiplying times a geometric argument to solve for the geometry as shown in Equation 5.18 and 5.19.

$$i_{tip} = \int_{r=0}^{r=a} 2\pi nFD_O r \frac{\partial C_o(r,0)}{\partial z} dr \tag{5.18}$$

$$i_{sub} = \int_{r=0}^{r=b} 2\pi nFD_R r \frac{\partial C_R(r,d)}{\partial z} dr \tag{5.19}$$

Where n is the number of electrons transferred (n=2 in this simulation), F is Faraday's constant (96485 C/mol).

Figure 5.8 shows representative results for the simulations at different values of the kinetic constant k (for the reaction of Amplexultrared and hydrogen peroxide in the presence of horseradishperoxidase) and comparison with the experimental current response data. The kinetic constant k was varied over 6 order of magnitude and limiting behavior under these conditions was found when $k \geq 10^4$ $m^3mol^{-2}s^{-1}(mM^{-1}s^{-1})$. When k value increases from 0.1 to 10^5, there is a positive shift in the peak potential position and increase in the peak size and reduction charge. When compared with the experimental current response that has peak potential at around 0.55 V_{RHE}, low k value of 5 ~ 10 shows similar reduction charge with that of experimental data but also shows huge peak potential shift (100 mV) negatively. In contrast, the large k value, i.e. over 10000, represents similar peak potential at around 0.5 V_{RHE} but shows much larger reduction charge compared to experimental data. With respect to this kinetic constant of decomposition of H_2O_2 chemical reaction catalyzed by enzyme

catalyst such as horseradishperoxidase (HRP), Baronas *et al*. (100) and Ohlsson *et al*. (101) proposed that the kinetic constant of reaction H_2O_2 with substrate such as Amplexultrared in presence of HRP enzyme catalyst, is around $7.1\times10^3 \sim 2\times10^4$ [$m^3mol^{-1}s^{-1}$]. If we regard this large kinetic constant (i.e. over $k > 10^4$) as adjustable in our study, the larger reduction charge in the simulated results compared to the experimental data can be thought due to the wrong assumption that all oxidation charge in Figure 5.6 (b) is the hydrogen peroxide oxidation reaction.

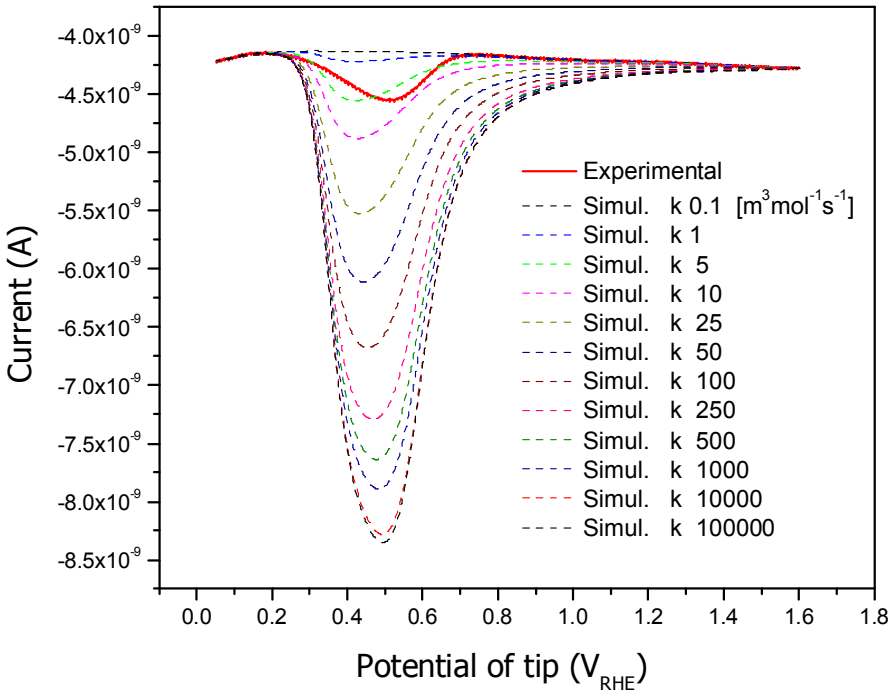

Figure 5.8 Experimental current response (red line) at substrate (200 μm diameter GC UME, scan rate of 100 mVs^{-1}, $E_{substrate}$ = 0.1 V_{RHE}) and simulated results with changing kinetic constant *k*.

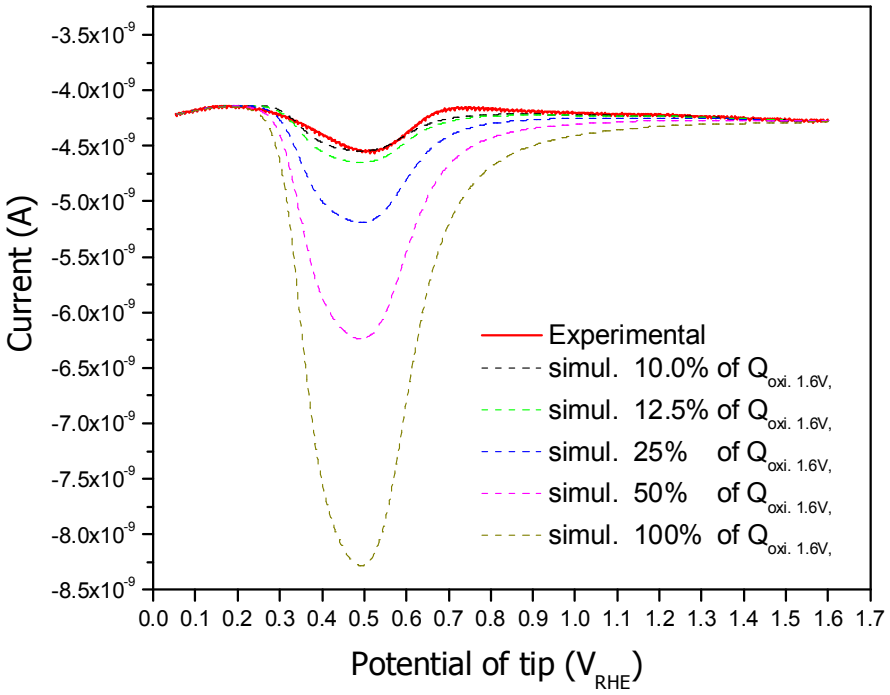

Figure 5.9 Experimental current response (red line) at substrate (200 μm diameter GC UME, scan rate of 100 mVs^{-1}, $E_{substrate}$ = 0.1 V_{RHE}) and simulated results with various oxidation charge of Figure 5. 8 only except for kinetic constant $k = 10^4$ [$m^3mol^{-1}s^{-1}$] fixed.

Figure 5.9 shows the variation of the reduction charge and peak size of the substrate response of the simulation with the various flux of H_2O_2 (N_{H2O2}), i.e. various H_2O_2 oxidation charge in Figure 5. 6 (b) when the kinetic constant, k, is fixed as 10^4 [$m^3mol^{-1}s^{-1}$]. Because this irreversible chemical reaction (Equation 5.7) is catalyzed by horseradishperoxidase (HRP), it is thought reasonable that the large

value of kinetic constant works for in this study. When compared to the experimental data, Figure 5.9 represents that only about 10 % of oxidation charge of the Figure 5. 6 (b) plays a role in the irreversible chemical reaction of Equation 5.7.

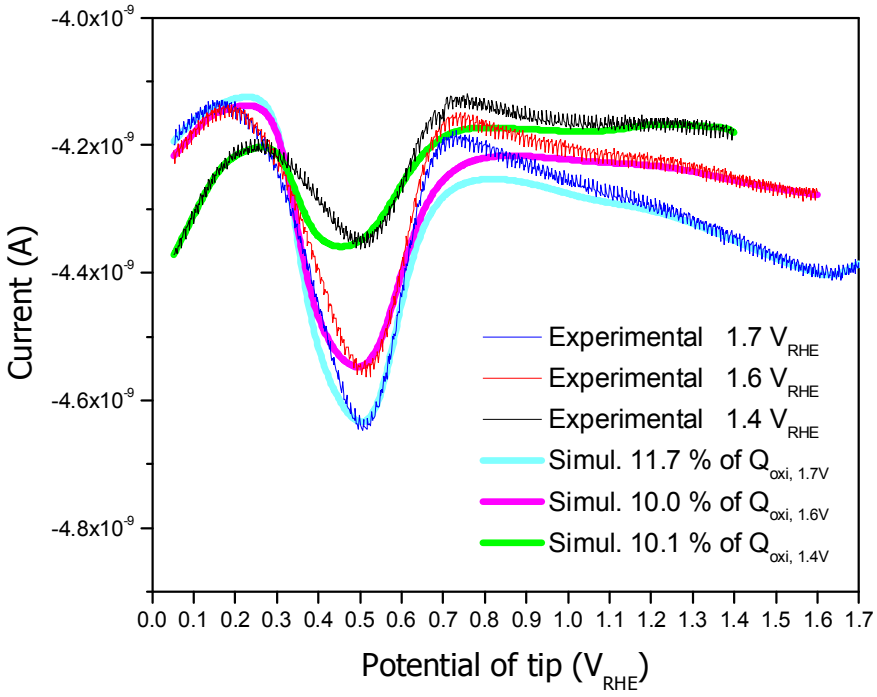

Figure 5.10 Comparison of experimental reduction current response at substrate (200 μm diameter GC UME, 100 mVs^{-1}, $E_{substrate}$ = 0.1 V_{RHE}) and simulated results with reduced oxidation charge and upper limit potentials. ($k = 10^4$ $[m^3mol^{-1}s^{-1}]$ fixed)

Figure 5.10 presents the comparison of the experimental with simulated data at reduced oxidation charge input and upper limit potentials. The results of simulated

data fit quite well with the experiment at all upper limit potentials and about 10~12 % of oxidation charge of Figure 5.6 (b) involves in HRP catalyzed chemical reaction.

Previously noted, we have at least 98 % collection efficiency in this SECM tip generation/substrate collection (TG/SC) positive feedback mode because we used larger size of substrate (200 μm diameter) compared to tip size (100 μm diameter) under very well aligned tip and substrate positioning. Therefore, we can consider that the result of simulation imply the previous assumption that the oxidation charge of Figure 5.6 (b) comes from all H_2O_2 oxidation is not correct assumption or imply there might be some factors that affect the irreversible chemical (Equation 5.7) and reversible electrochemical reaction (Equation 5.12) (C_iE_r) respectively.

The first factor we can suppose is the assumption of diffusion coefficient of Amplexultrared (D_p). We assumed that the diffusion coefficient of Amplexultrared (D_p) is 6.6×10^{-10} m^2s^{-1}, the same value as that of resorufin (D_O) and dihydroresorufin (D_R). However, with changing this value 4 order i.e. 6.6×10^{-8} ~ 6.6×10^{-12} m^2s^{-1} at simulation, we found there is no significant discrepancy in reduction current response of original value, 6.6×10^{-10} m^2s^{-1}. So we can conclude the C_iE_r reaction is not limited by diffusion of Amplexultrared around this range.

The second supposed factor is pH induced denaturation of HRP and Amplexultrared. The concept of using Amplexultrared and HRP in order to detect H_2O_2 in this study is very well known and still very widely being used in biochemistry to detect biological samples that release H_2O_2 and is known with the

name of enzyme linked immunosorbent assays (ELISA). The general reaction mechanism of HRP with substrate material is known as pH dependant (87-88, 101). For example, a substrate material such as Amplexultrared (modified N-acetyl-3,7-dihydroxyphenoxanzine) used in this study is a fluorogenic substrate material in a 1:1 stoichiometric ratio to produce resorufin (excitation/emission maxima ~ 568/581 nm) and has a efficiency of 60 % at pH 4.5 compared to that of pH 7.0 (Figure 5.11).

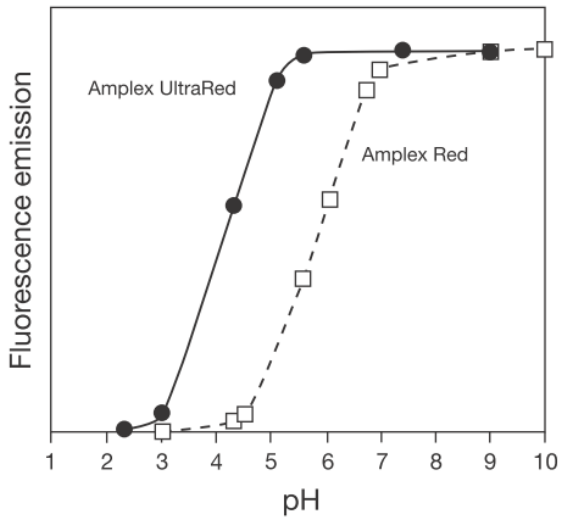

Figure 5.11 pH dependency of resorufin in fluorescence signal (measured at 568 (ex)/581(em) nm) as a production of Amplexultrared and H_2O_2 chemical reaction in the presence of HRP. (excerpt from www.invitrogen.com)

The third one is the collection efficiency in this SECM tip collection/substrate generation (TC/SG) feedback mode. Previously noted, we already got collection

efficiency of SECM tip generation/substrate collection (TG/SC) feedback mode is above 98 % in case of pure diffusion controlled redox reaction of FcMeOH as mediator. Because the initial concentration of resorufin (O) and dihydroresorufin (R) is zero in this study and the standard reduction potential of resorufin (O) is 0.34 V_{RHE}, when mole flux of H_2O_2 from tip electrode works as trigger for generation of resorufin (O) via irreversible enzyme catalyzed chemical reaction not by electrochemical reaction at above 0.34 V_{RHE}, the SECM mode is not only TC/SG feedback mode but also TG/SC feedback mode at the same time. In other words, because there is no O and R in the solution before H_2O_2 is generated during PtO_2 reduction at tip electrode, with generation of O via chemical reaction the SECM mode becomes generation (R at substrate, O at tip) mode and collection (R at tip, O at substrate) mode at the same time at above 0.34 V_{RHE}. However, at below 0.34 V_{RHE}, the feedback mode turns into negative feedback mode until all O deplete in the gap. In case of TC/SG mode where the tip diameter (100 μm Pt) is half of substrate diameter (200 μm GC) such as in this study, the collection efficiency drops to approximately value of 80 % at L = 0.1 and then this factor has to be taken into account as factor.

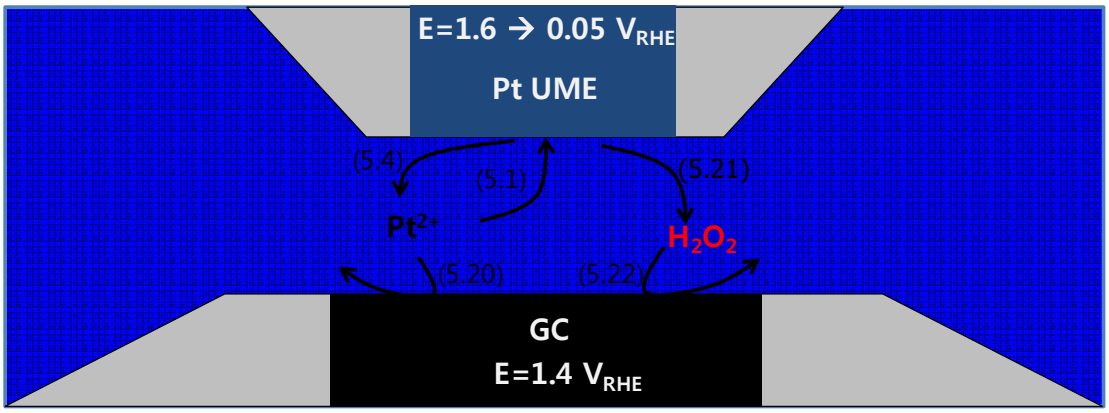

Figure 5.12 Suggested detection mechanism of mobile species generated during PtO_2 reduction process.

Figure 5.12 shows suggested detection mechanism of mobile species generated during PtO_2 reduction process. As introduced at the introduction part of this chapter, the reduction of PtO_2 has been regarded as the most probable source of mobile Pt species (i.e. Pt^{2+} via Equation 5.5 and 5.20) that could be detected electrochemically at the ring or substrate until quite recently (81, 83, 85). However, the potential around 0.6 ~ 0.7 V_{RHE} at disk or tip that Pt^{2+} was generated via PtO_2 reduction process was too negative for Pt^{2+} to be transferred to the ring or substrate by diffusion or convection. Therefore we expected that the x value of Equation 5.5 might be very small value because the electrochemical reduction of Pt^{2+} to Pt metal is more kinetically favorable than diffusion to substrate.

$$PtO_2 + 4H^+ + 2e^- \rightarrow Pt^{2+} + 2H_2O \quad (5.4)$$

$$PtO_2 + 4H^+ + 2(2-x)e^- \rightarrow xPt^{2+} + (1-x)Pt + 2H_2O \quad (5.5)$$

$$Pt^{2+} \rightarrow Pt^{4+} + 2e^- \quad (5.20)$$

Therefore, we questioned that the prevailing proposition that the detected mobile species is Pt^{2+} might not be correct. We there proposed a method of using enzyme catalyst and substrate with an assumption that the mobile species might be H_2O_2 or oxygen containing species and finally got results that prove this assumption was correct. Because of the difficulty in SECM experiment of C_iE_r reaction in pH 4.5 acid solution, we could not get an exact value of x and y of Equation 5.23. However, to the author's knowledge, the detection of H_2O_2 generation during PtO_2 reduction process was first accomplished by this dissertation.

$$PtO_2 + 2H^+ + 2e^- \rightarrow Pt + H_2O_2 \quad (5.21)$$

$$H_2O_2 \rightarrow O_2 + 2H^+ + 2e^- \qquad E^o = 0.695\ V_{RHE} \quad (5.22)$$

$$(1+y)PtO_2 + 2(2+y)H^+ + 2(2-x+y)e^- \rightarrow xPt^{2+} + (1-x+y)Pt + 2H_2O + yH_2O_2 \quad (5.23)$$

5.4 CONCLUSION

In conclusion, the RRDE and SECM experiments were used to detect and evaluate the nature of mobile species generated during PtO_2 reduction process. Especially, the SECM experiment showed the mobile species detected at GC substrate at 1.4 V_{RHE} is at least partially the oxidation of H_2O_2 by fulfilling irreversible chemical and reversible electrochemical reaction (C_iE_r) by using Amplexultrared and HRP in 0.1 M potassium phosphate pH 4.5 buffer solution.

Moreover, we performed diffusion controlled simulation under transient condition using COMSOL Multiphysics in order to support the experimental result and find out quantify the amount of H_2O_2 generation. By setting up SECM model, we successively account for the reduction peak size and position with input of H_2O_2 flux converted from the oxidation current measured at E_{sub} = 1.4 V_{RHE} during PtO_2 reduction process.

Although we have not quantified the precise amount of H_2O_2 generated, these results suggest that H_2O_2 is generated during the PtO_2 reduction process, even in the absence of oxygen.

CHAPTER 6

SUMMARY

The purpose of this dissertation is to extend the fundamental understanding of the degradation of Pt catalysts in PEMFC cathodes. The ultimate goal would be the reduction of the electrocatalyst degradation through a better understanding of the degradation (dissolution) mechanisms. The extended discovery about Pt dissolution mechanism in this study would be very useful for new catalyst synthesis, system operation design.

Due to high catalytic activity for hydrogen oxidation reaction (HOR) for anode and oxygen reduction reaction (ORR) for cathode, Pt has been a standard catalyst for the electrode material of PEMFCs. However, its weak durability of Pt catalyst by degradation (dissolution) under the PEMFC operating conditions (i.e. < pH 1 and potential cycling) induces a lot of challenges for its application toward commercialization. The degradation (dissolution) of Pt catalyst as cathode material of PEMFC is known to be caused by several competing process; electrochemical anodic dissolution, electrochemical cathodic dissolution with combination of chemical dissolution (24).

Electrochemical anodic Pt dissolution

Within the scope of this dissertation in terms of potential cycling region, the dissolution of Pt catalyst can be explained by a direct electrochemical anodic dissolution path

$Pt \rightarrow Pt^{2+} + 2e^-$ $E\ (V_{RHE}) = 1.188 + 0.0295\log[Pt^{2+}]$ (6.1)

and the indirect chemical dissolution path via the electrochemical Pt oxide formation, the first one is from PtO.

$Pt+H_2O \rightarrow PtO + 2H^+ + 2e^-$ $E\ (V_{RHE}) = 0.98 - 0.0591pH$ (6.2)

$PtO + 2H^+ \rightarrow Pt^{2+} + H_2O$ (6.3)

The second path is from PtO_2 that is formed at higher potential region (48).

$PtO + H_2O \rightarrow PtO_2 + 2H^+ + 2e^-$ $E\ (V_{RHE}) = 1.045 + 0.0591pH$ (6.4)

$PtO_2 + 4H^+ \rightarrow Pt^{4+} + 2H_2O$ (6.5)

or

$PtO_2 + H_2O + H^+ \rightarrow Pt(OH)_3^+$ (6.6)

without taking the influence of oxygen into account (102). In this dissertation (chapter 3), however, we found out that oxygen dissolved in the acid solution significantly affects the Pt dissolution above E_H = 1.4 V_{RHE} where is the region of PtO_2 formation.

Electrochemical cathodic Pt dissolution

The cathodic path of Pt dissolution likely occurs in the low potential region. Thermodynamically, higher order oxides such as PtO_2 dissolve cathodically below 0.837 V_{RHE} (Equation 6.7) (24, 52).

$PtO_2 + 4H^+ + 2e- \rightarrow Pt^{2+} + 2H_2O$ $E\ (V_{RHE}) = 0.837 + 0.0295\ \log[Pt^{2+}]$ (6.7)

During the accelerated Pt dissolution test (ADT) of potential cycling, these series of electrochemical and chemical reaction (Equation 6.1 ~ 6.7) may happen repeatedly according to the upper potential (E_H) and lower potential (E_L).

With regards to clarifying which electrochemical reactions are likely dominant for Pt catalyst dissolution at specific potential region and electrochemical, chemical path, the experiment of this dissertation was focused on understanding the oxide-mediated dissolution of Pt catalysts by using electrochemical experiment methods such as RRDE, EQCN, SECM with a combination of ICP-MS and computational simulation with COMSOL Multiphysics.

For details, in chapter 3, oxide-mediated Pt dissolution rate and the influence of cation underpotential depositon (UPD) on Pt dissolution was measured by using EQCN flow cell, RRDE and ICP-MS. We found that the Pt dissolution rate was proportional to the upper potential limits (E_H) and revealed a broad maximum as a function of the lower potential limit (E_L) when the upper potential limit (E_H) was maintained at 1.6 V_{RHE}. From the RRDE test, the convection condition plays a key role in accelerating Pt dissolution over E_H = 1.2 V_{RHE}. The electrochemical active mobile species can be detected at the ring electrode (E_{ring} = 1.4 V_{RHE}) during cathodic scans of disk electrode at potentials more positive than E_H = 1.3 V_{RHE}. If we assume this mobile species is Pt^{2+}, the amount of Pt^{2+} detected at ring electrode is about 4.99 % of total dissolved Pt amount during cycling and suggest formation of other dissolved such as H_2O_2 or a great part of Pt^{2+} redeposit as soon as it generate during PtO_2 reduction process. We also found a significant Pt dissolution rate increase by adding 5 mM of Zn^{2+} ion in which the lower potential limit (E_L) was less than 0.2 V_{RHE}. These results represent that Zn UPD changed the properties of the Pt surface where the potential is less than 0.34 V_{RHE} or hinder soluble Pt species from re-

depositing on Pt surface. Although the exact mechanism of what occurs on the surface at lower potential and its effect on oxide formation and stripping is not yet clearly understood, the competition of Zn UPD (adsorption) with Pt^{2+} redeposition might work as the place exchange effect between Zn and Pt atoms if we assume Pt^{2+} is generated during PtO_2 reduction process as like as place exchange between Pt and oxygen above 0.95 V_{RHE} accelerate Pt dissolution in the potential cycling test by making Pt surface unstable.

In chapter 4, we found out how much oxygen reduction reaction (ORR) plays a role in Pt oxide formation/reduction and Pt catalyst dissolution by using gas changing LSV experiment, SWV by RDE and shielding effect method of RRDE. From the gas changing LSV experiment, we found that ORR plays a role on Pt oxide formation either by contributing at below 0.95 V_{RHE} ~ 1.0 V_{RHE} with facilitating oxygen dissociative or associative adsorption, and by impeding at above 0.95 V_{RHE} ~ 1.0 V_{RHE} by consuming oxygen on Pt surface. It is interesting that the potential of 0.95 V_{RHE} ~ 1.0 V_{RHE} is regarded as an onset potential of place exchange by a lot of previous works (77-80). Therefore we might think that Pt oxide as intermediator of ORR works differently according to the Pt surface property. Moreover, from the simultaneous electrochemical measurement of Pt oxidation/reduction in the presence of oxygen (SWV, shielding effect of RRDE), we found that ORR promotes Pt oxide formation and onset potential of Pt oxidation is also less positively shifted. We also found that ORR accelerates the Pt dissolution only at above E_H > 1.4 V_{RHE} in potential cycling test. This result imply that less positive onset potential shift of Pt

oxidation and larger Pt oxide coverage in the presence of oxygen act as a precursor state of place exchanged Pt oxide that accelerate Pt dissolution rather than oxide on Pt surface that protect Pt from dissolution(79). With the RRDE test, in the presence of oxygen in the 0.5M H_2SO_4 we found that the mobile species detected at ring electrode (E_{ring} = 1.4 V_{RHE}) during PtO_2 reduction process is also accelerated than N_2 or air condition. From the series of results, we can conclude that ORR plays a significant role in place exchanged Pt oxide formation and mobile species production generated during PtO_2 reduction reaction which is strongly related to Pt dissolution process.

In the chapter 5, we found out the nature of mobile species generated during PtO_2 reduction process which have been disputed as Pt ion or other mobile species and fulfilled computational simulation for evaluation of SECM experiment. With a suspicion that the reduction potential of PtO_2 is too negative for Pt^{2+} to be detected at ring or substrate electrode, we came up with the method of using enzyme catalyst and substrate with an assumption that the mobile species might be H_2O_2. The reduction peak at substrate (E_{sub}=0.1 V_{RHE}) is unimpeachable evidence of H_2O_2 generation during PtO_2 reduction process at Pt tip electrode. In addition to SECM experiment, with computational simulation by using COMSOL Multiphysics, we were able to theoretically support the SECM experiment result. Because of the difficulty in SECM experiment of C_iE_r reaction in pH 4.5 acid solution, however, we have not quantified the precise amount of H_2O_2 generated during PtO_2 reduction process even in the absence of oxygen condition. Even though the amount of H_2O_2 could not be

determined precisely, we are sure that the generation of H_2O_2 on the surface of Pt in the cathode electrode of PEMFC is critical to PEMFC performance degradation.

In summary, in an effort to elucidate the detailed Pt dissolution processes, we found out

1. The anodic Pt dissolution is proportional to the upper potential limit (E_H) which is significantly related to the amount of PtO_2 and the degree of place exchange between Pt and O. (chaper 3)
2. The cathodic Pt dissolution by PtO_2 reduction process was proved by changing the lower potential limit (E_L) and by incorporating Zn UPD experiment. (chapter 3)
3. The oxygen reduction reaction (ORR) plays a role on Pt dissolution by increasing the amount of PtO_2 formation only above E_H = 1.4 V_{RHE} at Pt dissolution acceleration test. (chapter 4)
4. The evidence of H_2O_2 generation during PtO_2 reduction process was proved by using SECM experiment with combination of COMSOL simulation. (chapter 5).

In terms of the purpose of this dissertation; finding out the nature of oxide-mediated Pt dissolution, how much ORR influences to Pt oxide formation/reduction and Pt dissolution and what is the nature of mobile species generated during PtO_2 reduction process, are sure to be very helpful in developing new catalysts and enhancing system design and suggested operating conditions.

BIBLIOGRAPHY

1. U. Stimming, L. Carrette and K. A. Friedrich, *Chemphyschem*, **1**, 162 (2000).
2. A. Kirubakaran, S. Jain and R. K. Nema, *Renew Sust Energ Rev*, **13**, 2430 (2009).
3. M. Mathias, H. Gasteiger, R. Makharia, S. Kocha, T. Fuller and J. Pisco, *Abstr Pap Am Chem S*, **228**, U653 (2004).
4. R. Borup, J. Meyers, B. Pivovar, Y. S. Kim, R. Mukundan, N. Garland, D. Myers, M. Wilson, F. Garzon, D. Wood, P. Zelenay, K. More, K. Stroh, T. Zawodzinski, J. Boncella, J. E. McGrath, M. Inaba, K. Miyatake, M. Hori, K. Ota, Z. Ogumi, S. Miyata, A. Nishikata, Z. Siroma, Y. Uchimoto, K. Yasuda, K. I. Kimijima and N. Iwashita, *Chem Rev*, **107**, 3904 (2007).
5. M. L. Perry and T. F. Fuller, *J Electrochem Soc*, **149**, S59 (2002).
6. M. S. Wilson and S. Gottesfeld, *J Appl Electrochem*, **22**, 1 (1992).
7. M. S. Wilson and S. Gottesfeld, *J Electrochem Soc*, **139**, L28 (1992).
8. C. K. Dyer, *J Power Sources*, **106**, 31 (2002).
9. H. A. Gasteiger, S. S. Kocha, B. Sompalli and F. T. Wagner, *Appl Catal B-Environ*, **56**, 9 (2005).
10. A. Sarkar and A. Manthiram, *J Phys Chem C*, **114**, 4725 (2010).
11. A. Sarkar, A. V. Murugan and A. Manthiram, *J Phys Chem C*, **112**, 12037 (2008).
12. B. Seger and P. V. Kamat, *J Phys Chem C*, **113**, 7990 (2009).
13. E. Antolini and E. R. Gonzalez, *Solid State Ionics*, **180**, 746 (2009).
14. S. C. Ball, S. L. Hudson, D. Thompsett and B. Theobald, *J Power Sources*, **171**, 18 (2007).

15. C. A. Reiser, L. Bregoli, T. W. Patterson, J. S. Yi, J. D. L. Yang, M. L. Perry and T. D. Jarvi, *Electrochem Solid St*, **8**, A273 (2005).

16. V. A. Sethuraman, J. W. Weidner, A. T. Haug and L. V. Protsailo, *J Electrochem Soc*, **155**, B119 (2008).

17. S. Mitsushima, S. Kawahara, K. I. Ota and N. Kamiya, *J Electrochem Soc*, **154**, B153 (2007).

18. H. J. Wang, S. S. Zhang, X. Z. Yuan, J. N. C. Hin, K. A. Friedrich and M. Schulze, *J Power Sources*, **194**, 588 (2009).

19. A. A. Franco and M. Gerard, *J Electrochem Soc*, **155**, B367 (2008).

20. L. M. Roen, C. H. Paik and T. D. Jarvic, *Electrochem Solid St*, **7**, A19 (2004).

21. M. V. Williams, H. R. Kunz and J. M. Fenton, *J Electrochem Soc*, **151**, A1617 (2004).

22. T. Madden, M.Perry, L.Protsailo, M.Gullalla, S.Burlastsky, N.Cipollini, S.Motupally and T.Jarvi, *Handbook of Fuel cells*, chapter 58, Wiley (2009)..

23. Y. Shao-Horn, W. C. Sheng, S. Chen, P. J. Ferreira, E. F. Holby and D. Morgan, *Top Catal*, **46**, 285 (2007).

24. M. Pourbaix, *Atlas of Electrochemical Equilibria in Aqueous Solutions*, 380 (1966).

25. X. P. Yan, H. F. Liu and K. Y. Liew, *J Mater Chem*, **11**, 3387 (2001).

26. G. E. van Dorssen, D. C. Koningsberger and D. E. Ramaker, *J Phys-Condens Mat*, **14**, 13529 (2002).

27. D. E. Ramaker and D. C. Koningsberger, *Phys Rev Lett*, **89** (2002).

28. P. Bindra, S. J. Clouser and E. Yeager, *J Electrochem Soc*, **126**, 1631 (1979).

29. X. P. Wang, R. Kumar and D. J. Myers, *Electrochem Solid St*, **9**, A225 (2006).

30. G. Jerkiewicz, G. Vatankhah, J. Lessard, M. P. Soriaga and Y. S. Park, *Electrochim Acta*, **49**, 1451 (2004).

31. B. E. Conway, B. Barnett, H. Angersteinkozlowska and B. V. Tilak, *J Chem Phys*, **93**, 8361 (1990).

32. Kinoshit.K, Lundquis.Jt and Stonehar.P, *J Electroanal Chem*, **48**, 157 (1973).

33. M. Uchimura, S. Sugawara, Y. Suzuki, J. B. Zhang and S. S. Kocha, in *Proton Exchange Membrane Fuel Cells 8, Pts 1 and 2*, T. Fuller, K. Shinohara, V. Ramani, P. Shirvanian, H. Uchida, S. Cleghorn, M. Inaba, S. Mitsushima, P. Strasser, H. Nakagawa, H. A. Gasteiger, T. Zawodzinski and C. Lamy Editors, p. 225 (2008).

34. J. A. S. Bett, K. Kinoshita and P. Stonehart, *J Catal*, **41**, 124 (1976).

35. M. S. Wilson, F. H. Garzon, K. E. Sickafus and S. Gottesfeld, *J Electrochem Soc*, **140**, 2872 (1993).

36. E. Endoh, S. Terazono, H. Widjaja and Y. Takimoto, *Electrochem Solid St*, **7**, A209 (2004).

37. A. Pozio, R. F. Silva, M. De Francesco and L. Giorgi, *Electrochim Acta*, **48**, 1543 (2003).

38. W. Liu and D. Zuckerbrod, *J Electrochem Soc*, **152**, A1165 (2005).

39. D. E. Curtin, R. D. Lousenberg, T. J. Henry, P. C. Tangeman and M. E. Tisack, *J Power Sources*, **131**, 41 (2004).

40. V. O. Mittal, H. R. Kunz and J. M. Fenton, *J Electrochem Soc*, **154**, B652 (2007).

41. T. Frelink, W. Visscher and J. A. R. vanVeen, *Langmuir*, **12**, 3702 (1996).

42. A. J. Bard and L. R. Faulkner, *Electrochemical Methods: Fundamentals and Applications*, John Wiley & sons, NJ (2001).

43. A. J. Bard, F. R. F. Fan, J. Kwak and O. Lev, *Anal Chem*, **61**, 132 (1989).

44. D. A. Stevens, M. T. Hicks, G. M. Haugen and J. R. Dahn, *J Electrochem Soc*, **152**, A2309 (2005).

45. B. E. Conway, *Prog Surf Sci*, **49**, 331 (1995).

46. B. E. Conway and G. Jerkiewicz, *J Electroanal Chem*, **339**, 123 (1992).

47. D. A. Harrington, *J Electroanal Chem*, **420**, 101 (1997).

48. S. Mitsushima, Y. Koizumi, S. Uzuka and K. I. Ota, *Electrochim Acta*, **54**, 455 (2008).

49. E. Guilminot, A. Corcella, M. Chatenet, F. Maillard, F. Charlot, G. Berthome, C. Iojoiu, J. Y. Sanchez, E. Rossinot and E. Claude, *J Electrochem Soc*, **154**, B1106 (2007).

50. A. Sun, J. Franc and D. D. Macdonald, *J Electrochem Soc*, **153**, B260 (2006).

51. G. Benke and W. Gnot, *Hydrometallurgy*, **64**, 205 (2002).

52. D. C. Johnson, D. T. Napp and Buckenst.S, *Electrochim Acta*, **15**, 1493 (1970).

53. D. A. J. Rand and R. Woods, *J Electroanal Chem*, **35**, 209 (1972).

54. R. M. Darling and J. P. Meyers, *J Electrochem Soc*, **150**, A1523 (2003).

55. A. A. El-Shafei, *J Electroanal Chem*, **447**, 81 (1998).

56. S. Taguchi and A. Aramata, *J Electroanal Chem*, **396**, 131 (1995).

57. G. Vatankhah, J. Lessard, G. Jerkiewicz, A. Zolfaghari and B. E. Conway, *Electrochim Acta*, **48**, 1613 (2003).

58. A. P. Yadav, A. Nishikata and T. Tsuru, *Electrochim Acta*, **52**, 7444 (2007).

59. T. Hachiya, H. Honbo and K. Itaya, *J Electroanal Chem*, **315**, 275 (1991).

60. K. Sashikata, N. Furuya and K. Itaya, *J Electroanal Chem*, **316**, 361 (1991).

61. A. Aramata, M. A. Quaiyyum, W. A. Balais, T. Atoguchi and M. Enyo, *J Electroanal Chem*, **338**, 367 (1992).

62. F. Mikuni and T. Takamura, *Denki Kagaku*, **38**, 113 (1970).

63. S. Trasatti, *Z Phys Chem Neue Fol*, **98**, 75 (1975).

64. S. Taguchi, A. Aramata, M. A. Quaiyyum and M. Enyo, *J Electroanal Chem*, **374**, 275 (1994).

65. K. Varga, P. Zelenay, G. Horanyi and A. Wieckowski, *J Electroanal Chem*, **327**, 291 (1992).

66. N. M. Markovic and P. N. Ross, *Surf Sci Rep*, **45**, 121 (2002).

67. A. Damjanovic, *J Electrochem Soc*, **138**, 2315 (1991).

68. J. L. Zhang, M. B. Vukmirovic, Y. Xu, M. Mavrikakis and R. R. Adzic, *Angew Chem Int Edit*, **44**, 2132 (2005).

69. N. M. Markovic, H. A. Gasteiger, B. N. Grgur and P. N. Ross, *J Electroanal Chem*, **467**, 157 (1999).

70. C. H. Paik, T. D. Jarvi and W. E. O'Grady, *Electrochem Solid St*, **7**, A82 (2004).

71. Y. X. Liu, M. Mathias and J. L. Zhang, *Electrochem Solid St*, **13**, B1 (2010).

72. S. Sugawara, K. Tsujita, S. Mitsushima, K. Shinohara and K.-i. Ota, *Electrocatalysis*, **2**, 60 (2011).

73. M. Matsumoto, T. Miyazaki and H. Imai, *J Phys Chem C*, **115**, 11163 (2011).

74. W. Bi, Q. Sun, W. Deng and T. F. Fuller, *Electrochim Acta*, **54**, 1826 (2009).

75. J. K. Norskov, J. Rossmeisl, A. Logadottir, L. Lindqvist, J. R. Kitchin, T. Bligaard and H. Jonsson, *J Phys Chem B*, **108**, 17886 (2004).

76. Angerste.H, B. E. Conway and W. B. A. Sharp, *J Electroanal Chem*, **43**, 9 (1973).

77. F. T. Wagner and P. N. Ross, *Surf Sci*, **160**, 305 (1985).

78. M. Alsabet, M. Grden and G. Jerkiewicz, *J Electroanal Chem*, **589**, 120 (2006).

79. D. Friebel, D. J. Miller, C. P. O'Grady, T. Anniyev, J. Bargar, U. Bergmann, H. Ogasawara, K. T. Wikfeldt, L. G. M. Pettersson and A. Nilsson, *Phys Chem Chem Phys*, **13**, 262 (2011).

80. H. Imai, K. Izumi, M. Matsumoto, Y. Kubo, K. Kato and Y. Imai, *J Am Chem Soc*, **131**, 6293 (2009).

81. G. Inzelt, B. Berkes and A. Kriston, *Electrochim Acta*, **55**, 4742 (2010).

82. V. I. Birss, M. Chang and J. Segal, *J Electroanal Chem*, **355**, 181 (1993).

83. A. P. Yadav, A. Nishikata and T. Tsuru, *J Electrochem Soc*, **156**, C253 (2009).

84. H. You and Z. Nagy, *Electrochim Acta*, **47**, 3037 (2002).

85. M. Umeda, Y. Kuwahara, A. Nakazawa and M. Inoue, *J Phys Chem C*, **113**, 15707 (2009).

86. H. B. Dunford, *Horseradish peroxidase: structure and kinetic properties*, CRC Press, Boca Raton (1990).

87. D. Dolphin, A. Forman, D. C. Borg, J. Fajer and R. H. Felton, *P Natl Acad Sci USA*, **68**, 614 (1971).

88. H. B. Dunford and J. S. Stillman, *Coordination Chemistry Reviews*, **19**, 187 (1976).

89. A. Honji, T. Mori, K. Tamura and Y. Hishinuma, *J Electrochem Soc*, **135**, 355 (1988).

90. J. Xie, D. L. Wood, K. L. More, P. Atanassov and R. L. Borup, *J Electrochem Soc*, **152**, A1011 (2005).

91. K. Yasuda, A. Taniguchi, T. Akita, T. Ioroi and Z. Siroma, *Phys Chem Chem Phys*, **8**, 746 (2006).

92. P. J. Ferreira, G. J. la O', Y. Shao-Horn, D. Morgan, R. Makharia, S. Kocha and H. A. Gasteiger, *J Electrochem Soc*, **152**, A2256 (2005).

93. J. Aragane, T. Murahashi and T. Odaka, *J Electrochem Soc*, **135**, 844 (1988).

94. J. Aragane, H. Urushibata and T. Murahashi, *J Appl Electrochem*, **26**, 147 (1996).

95. T. Akita, A. Taniguchi, J. Maekawa, Z. Sirorna, K. Tanaka, M. Kohyama and K. Yasuda, *J Power Sources*, **159**, 461 (2006).

96. K. Yasuda, A. Taniguchi, T. Akita, T. Ioroi and Z. Siroma, *J Electrochem Soc*, **153**, A1599 (2006).

97. J. L. Lyon and K. J. Stevenson, *Anal Chem*, **78**, 8518 (2006).

98. E. A. Schilling, A. E. Kamholz and P. Yager, *Anal Chem*, **74**, 1798 (2002).

99. M. V. Vazquez, S. R. Desanchez, E. J. Calvo and D. J. Schiffrin, *J Electroanal Chem*, **374**, 179 (1994).

100. R. Baronas, E. Gaidamauskaite and J. Kulys, *Sensors-Basel*, **7**, 2723 (2007).

101. P. I. Ohlsson, K. G. Paul and S. Wold, *Acta Chemica Scandinavica Series B-Organic Chemistry and Biochemistry*, **38**, 853 (1984).

102. L. Kim, C. G. Chung, Y. W. Sung and J. S. Chung, *J Power Sources*, **183**, 524 (2008).

VITA

Seok koo Kim was born in Republic of Korea. He earned his B.S and M.S. degrees in Chemical Engineering from Sogang University in Seoul, Republic of Korea, respectively, in February, 1999 and July, 2001. He worked at the LG chem Ltd. Research Park as a research scientist from Jun, 2001 to August, 2007. He entered the University of Texas at Austin in August, 2007.

Email address : ibankim@gmail.com

This dissertation was typed by the author.